Characterization of Hierarchical Morphologies in Co-Sputter Deposited Immiscible Alloy Thin Films

by

Max Lyle Powers

A dissertation submitted in partial fulfillment
of the requirements for the degree of
Doctor of Philosophy
(Materials Science and Engineering)
in the University of Michigan
2021

Doctoral Committee:

Professor Amit Misra, Chair
Assistant Professor Yue Fan
Assistant Professor John Heron
Assistant Professor Liang Qi

Max L. Powers

maxpow@umich.edu

ORCID iD: 0000-0003-1195-3264

Dedication

Dedicated to all of those who believed in me: my parents, my sister, and Gina, my heart, my light

"Veda means originally knowing or knowledge, and this name is given"
-Ramayana of Valmiki

"Ah, merciless love, is there any length to which you cannot force the human heart to go?"
– Dido, The Aeneid

Acknowledgements

This PhD has been the culmination of many years of work and discipline, stretching back to before graduate school and undergraduate. My ambition in achieving a doctoral degree is driven by my love for science, my love for research, and principally by my love for my parents and my desire to use education as a tool to pull up those around me. I still remember the days where I would sit cross-legged on my bed for countless hours, leafing through my high school homework and studying for the standardized exams. And now here it is, this document representing the grand sum of my efforts, the long-awaited fruit picked in the orchard of delayed gratification.

I would like to first thank my advisor, Professor Amit Misra, for developing me as a researcher and providing guidance to navigate the rocky road of graduate school. Professor Misra has demonstrated his true character as someone with an unparallel work ethic who strives tirelessly to help others. His probing questions challenged my material science knowledge and pushed me to explore novel research paths, re-igniting my passion for investigating the unknown. Throughout these years, I have seen Professor Misra demonstrate his selflessness on multiple occasions and perform great acts of kindness for both those inside and outside the Michigan materials community. It is easy to see why he is so respected. I also thank him for indulging in my cultural references, I apologize for not commenting on the Beatles calendar in his office (my father loves the Beatles and I have seen a number of documentaries based on them). I really could not have picked a better advisor and friend, thank you Professor Misra.

I extend my gratitude to Dr. Benjamin Derby, an esteemed colleague and friend. I have scarcely met anyone with such a passion for research and an inherent love for characterizing the underlying physics. The first day we worked together on the PVD-75 marked an inflection point in my graduate school career and a dramatic upswing in my productivity. I really enjoyed our conversations spanning from surface wetting and thin film growth, to horseback riding, to sociological comparisons of rural versus urban societies, to German culture, to the perfect wrench capability. Dr. Derby made the laboratory fun and exciting. Every day there was a new challenge, a new error to troubleshoot, new solutions to brainstorm. I would be remiss if I did not mention the cosmic coincidence of our mutual geographic origin of Upstate New York. It was a sincere pleasure working with you Ben, thank you.

I would like to thank my collaborators Dr. Remi Dingreville and Dr. James Stewart for your patience in showing me the MEMPHIS framework. Thank you for the discussions, showing me Sandia National Laboratories, and for helping me put together a truly great publication. I also appreciated the references to French culture, from Charlemagne to Giscard d'Estaing, and to Upstate New York (Dr. Stewart is also a native). Thank you to Professor Michael Demkowicz. Thank you to Professor John Heron, Professor Liang Qi, and Professor Yue Fan for serving on my committee, for your comments, and for all the help in your respective classes. Thank you Professor Emmanuelle Marquis, my understanding of thermodynamics increased tenfold after your class. Thank you to Professor John Kieffer who entrusted me not once, but twice with grading for his course. Thank you Professor Brian Love, I purchased a copy of your book and I must bring it to you for a signature. Thank you Professor Lumin Wang, microscopy has become one of the pleasures of my graduate research. Thank you Professor Robert Hovden for indulging in my conversations about apple orchards and for always buying the nice coffee for the

breakroom, that does not go unnoticed. Thank you Professor Rachel Goldman for always saying C'hag S'meach during the holidays. Thank you Professor Richard Laine for your stories. Thank you Professor Pierre Poudeau for allowing me to practice my few phrases in French. Thank you Professor Manos Kioupakis and Professor Kathleen Sevener for helping me with the professional development work, all of those career panels would not have been possible without your help. To Professor Kioupakis, your group is the happiest of all the research groups in MSE, keep it up! Thank you, Professor Kioupakis, for showing me how to say Iphigenia and for catching my references on Orestes and the Furies, I hope Ari grows as strong as Hector.

Thank you to my labmates and the MSE community who have made graduate school a fun, enriching journey. Thank you to Mohsen Taheri Andani, Huai-Hsun/Burt, Lien, Arya Chaterjee, Li Jiang, Zhihua Huang, Yuchi Cui, Bibhu Sahu Prasad, Jacob Garves, Nicholas Etrick, Jeremy Yoo, Jason Luce, and David Montiel. Thank you for help on research ranging from microscopy to simulation. I would not have had half the fun I had during graduate school (and learned so much about so many different cultures) without my labmates and our conversations. Thank you to Evan Raeker for being an excellent undergraduate researcher, it is a pleasure to see you go onto your own PhD.

Thank you to my friends who brightened up my evenings and weekends, you are what I will miss most about Ann Arbor: Jonathan Schwartz, Brian Macdonald, Kathy Macdonald, Kevin Schneider, Lexi Schneider, Joseph Lowman, Paul Chao, Julia Lenef, Kathleen Chou, Nathan Louis, Aaron Gladstein, George Lindemann, Kyle Bushwick, Ju Won Lim, Brian Iezzi, Isabel Newton, Laura Andre, Brandon Carter, Carolyn Carter, Michael Chen, Ming Lee, Vishwas Goel, Youngwoo Woo, Duncan Greely, David Speer, Randy Cheng, Emmanuel Vega, , Kristen Soto, Joseph Valle, and Alexandra Halvey.

Special thanks to the Hovden research group: Jonathan Schwartz, Suk Hyun Sung, and Jiseok Gim. Whether it was talking about microscopy, tomography, image correlation, or English-to-Korean translation, I always enjoyed the shared lab between our groups. Thank you very much Jiseok for showing me to value in imaging on low-index zone axis (otherwise those diffraction patterns can be ridiculous!). I also thank you for your friendship and for discussing the fourth and fifth Korean Republics with me. Thank you to the Ann Arbor Rugby Football Club and the fun memories for the last four years.

I would like to recognize the administrators and MSE staff who have been so helpful to me during graduate school, Shelley Fellers, Renee Hilgendorf, Dr. Timothy Chambers, Ying Qi, Todd Richardson, and Debbie Johnson. Thank you to the staff at the Michigan Center for Materials Characterization (MC^2), Bobby Kerns, Deanna Wendel, Dr. Nancy Muyanja, Dr. Allen Hunter, Dr. Kai Sun, Dr. Tao Ma, and Dr. Haiping Sun, you have made microscopy fun and engaging.

Thank you to my sister, Bobbijo Leah Nagar-Powers for always being there for a phone call and for giving me Tiferet and Rivkah to hold and play with. Thank you for keeping the faith. Thank you to both my parents, Karen and Steven, who have supported me since I was young. They never had any such educational opportunities and I hope this PhD is the ultimate gift for all they have given up to help me over the years. My love for my parents has been the guiding fuel without which my life would have taken a very different path. I hope to make good on my promises and make you both proud.

Finally, I thank Dr. Gina Yu, MD for all her support these last five years. Gina, your passion and strength far exceed my own, you have been a perfect partner and I love you greatly. I am very much looking forward to the next chapter with you.

The research in this dissertation was performed under the Center for Research Excellence on Dynamically Deformed Solids (CREDDS) sponsored by the Department of Energy – National Nuclear Security Administration (DOE-NNSA), Stewardship Science Academic Program under the Award No. DE-NA0003857. Microscopy was performed at the Michigan Center for Materials Characterization at the University of Michigan. Mesoscale modeling concepts were developed in collaboration with the Center for Integrated Nanotechnologies (CINT) with the assistance of Drs. Remi Dingreville and James Stewart.

Table of Contents

List of Tables

List of Figures

Abstract

The processing-microstructure-properties relationships of unique hierarchical microstructure morphologies that resulted from the co-deposition of immiscible alloy thin films were studied. The hierarchical morphologies, which consist of distinct features at multiple length scales, present a unique self-assembled microstructure with plastic deformation capabilities exceeding traditional multilayer or monomodal concentration modulation structures. The present work examined a series of immiscible alloy systems: Cu-Ta, Cu-Ag, Cu-Fe, Cu-Mo, Mo-Ag, Cu-Mo-Ag, and varied the physical vapor deposition processing parameters of deposition temperature and rate to determine the kinetic conditions and thresholds favorable for hierarchical organization and the formation mechanism of such structures. A two-prong approach, experimental and computational, was employed to characterize the microstructural features, study the energetics of the metastable phases, and examine the influence of localized compositional differences on microstructural evolution. The studies include microscopic characterization of monomodal and multimodal Cu-Ta systems, a systematic survey of processing parameters to induce hierarchical formation in a number of immiscible systems, molecular dynamics computation to evaluate the energetics of the metastable nanoprecipitates present in microstructural agglomerates, phase-field simulation to replicate thin film deposition while varying localized concentration, and nanoindentation to affiliate microstructure features with mechanical performance.

Ultimately, it was determined that the hierarchical structures form with sufficient disparity in kinetic energy between the constituent atoms, one species being highly mobile and the other relatively immobile. The highly mobile species agglomerates quickly during film depositions to drive a localized compositional disparity in select regions to encapsulate the relatively immobile species as a minority nanoprecipitate. This condition arises typically at elevated deposition temperatures and reduced deposition rates but is also alloy dependent. Finally, we examine the mechanical performance of the hierarchical thin films using nanoindentation. The hardness and Young's moduli of the films are variant based on surface topology and underlying microstructure of protruding grains or flat film regions but exceed rule-of-mixtures performance of the constituent elements.

Chapter 1

Introduction

Thin films are an interesting material class with a diverse set of applications. Some examples are functional coatings to enhance the mechanical properties of a bulk [1], protective layering to prevent oxidation of a structure [2], conductive coatings to facilitate charge transfer in semi-conductors [3], or interfaces for magnetic memory transcription [4]. In any application, the thin film properties are directly affiliated with its material microstructure. Variations in grain size, orientation, texture, interfacial character, and microstructural heterogeneities, can result in significantly different film properties even within the same material system. To truly understand a thin film system, it is important to establish the relationship between processing conditions, the material microstructure, and the resultant thin film properties. The processing-microstructure-properties relationship is the cornerstone of thin film research (and material science as a whole) and is a useful framework for investigating new systems. This dissertation aims to establish the processing-microstructure-properties relationship for a new morphology of immiscible alloy thin films co-deposited with physical vapor deposition. The work presented here builds upon previous research of metallic nanocomposites by investigating immiscible metal alloy systems which self-assemble into a hierarchical morphology during fabrication. The goals of this dissertation are threefold: one, define the processing parameters and kinetic conditions that induce hierarchical microstructure organization, two, characterize the microstructure's

morphological features with electron microscopy and mesoscale computational methods, three, establish a baseline mechanical performance for functional coating applications.

Many structural biological materials like nacre, wood, and bone, are composites that contain finer sub-structure with distinct features across the multiple length scales making them hierarchical structures. Such hierarchical organization leads to their elevated mechanical performance in functional biological applications [5]. The exceptional properties of biological materials with hierarchical microstructures prompts the exploration of hierarchical morphologies in metallic nanocomposites. The question arises: can we replicate this natural morphology in the lab? If so, what is its functional application and how can we vary the processing to tune its properties as a metallic thin film?

Before directly analyzing hierarchical morphologies, we must first generally review metallic nanocomposites. Metallic nanocomposites are attractive as materials and coatings in tribological and mechanical applications as the combination of multiple phases in the nanocomposite can yield synergistic properties difficult to achieve in a single phase alloy, such as improved ductility, high yield strength, and increased fatigue and wear [6,7].

In typical use-cases, metallic thin films are processed with a monomodal microstructure geometry as monolithic, single-phase films or multi-layer laminate thin films. Monomodal indicates that the morphology can be described with a single characteristic length parameter. In the case of single-phase films, the parameter is often grain size, and for multilayer films the parameter is layer thickness. Figure 1-1 presents a cartoon of a thin film with monomodal microstructure morphology. Fig. 1-1(a) is a monolithic film and Fig. 1-1(b) is a multilayer film. Fig. 1-1(c) displays a hierarchical morphology which will be discussed in further detail in later paragraphs.

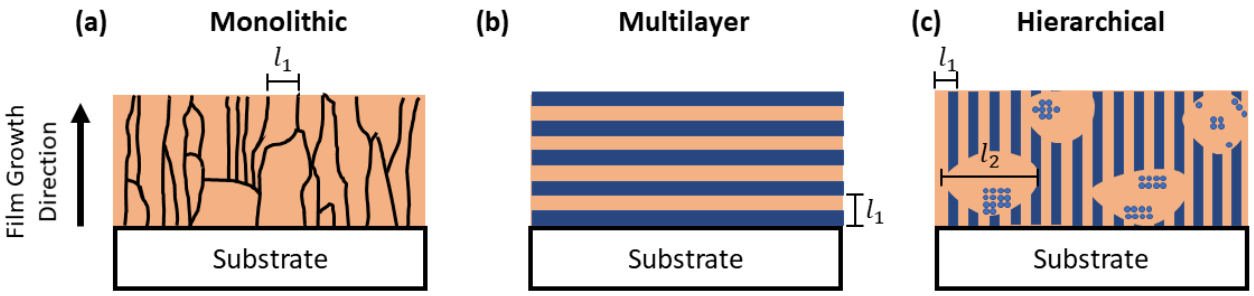

Figure 1-1: Cartoons of three possible thin film architectures. The characteristic length is the relevant length scale that describes the microstructure morphology (a) Monolithic, single phase films with a characteristic length, l_1, defined by the grain boundary spacing. (b) Multilayer films, that can be produced via sequential deposition or co-deposition and self-segregation, the characteristic length is the layer thickness. (c) Hierarchical microstructure morphology with distinct features on multiple length scales, shown here with alternating layers and agglomerates with nanoprecipitates. Uniquely, the sample hierarchical architecture has two characteristic length scales.

For metallic nanocomposites, previous research has emphasized the multilayer monomodal morphology. The films can be deposited sequentially to form well-defined multilayers with thickness controlled by deposition rates which in turn, enables targeted mechanical performance. Reducing composite layer thickness to the submicron range activates classic Hall-Petch strengthening in which the yield strength of a material increases with the decreasing square root of the layer thickness ($\sigma_{flow} \propto \frac{1}{\sqrt{d}}$ with σ_{flow} and d representing flow stress and layer thickness respectively) [8-9]. When the layer thickness is further reduced to under one approximately hundred nanometers, classic Hall-Petch strengthening no longer describes the mechanical performance as the dislocation pile-up at the interface becomes less relevant. Instead, the operative deformation mechanism is controlled by single dislocation interactions with the interphase boundary obstacles, resulting in either confined layer slip or interface crossing [10], [11].

The multilayer geometries provide a number of adjustable parameters in the materials selection, the length scale and geometry of layers, and the interfacial character to tune a metallic nanocomposite to a specific thin film application. Indeed, there are numerous examples of sequentially deposited multilayer systems, such as Cu/Cr [12], Cu/Fe [13], Cu/Nb [14], that have tailored hardness or modulus values based on layer thickness. These thin film systems benefit from the multilayer interfaces and the varying interfacial influence on deformation mechanisms as stated in the previous paragraph. The resulting multilayers exhibit enhanced mechanical properties, such as high hardness [12], exceeding values predicted by a simple rule of mixtures based on constituent composition.

The multilayer geometries in metallic nanocomposites may also form via self-assembly during co-deposition in immiscible alloy systems. High heat of mixing and dissimilar FCC and BCC equilibrium crystal structures encourage a phase-separating driving force in immiscible alloy systems such as Cu-W [15] and Cu-Mo [16]. The co-deposited elements will land on the substrate surface and segregate into phase-separated regions resembling sequentially deposited multilayers. Whereas sequentially deposited multilayers are grown with one geometry, the layers perpendicular to the film growth direction (see Fig. 1-1(b)), the co-deposited phase-separated regions will assemble into a variety of orientations. Depending on the processing parameters of deposition rate and deposition temperature, the phase-separated regions can form alternating phase layers in the film growth direction, perpendicular to the film growth direction, or in a random orientation [16].

The metallic multilayer thin films display elevated yield strength under uniaxial loading. Literature examples note 2.2 GPa yield stress for Cu/Nb with 5 nm thickness [17] and 2.8 GPa yield stress for Cu/Mo with 3 nm layer thickness [18]. However, the multilayer geometries have

a significant drawback in their plastic deformation regime. Under loading, the flow stress localizes into narrow bands, typically within the softer material layer, that promote local shearing and eventual shear band formation. The large shear band propagates through the microstructure eventually leading to fracture while the rest of the non-sheared material remains mildly deformed [17]. An example of the shear banding in multilayers is presented in Fig. 1-2. Interphase boundaries impede both dislocation glide and crack propagation [18].

The self-assembled 3D microstructures can mitigate the issue of stress localization. Derby *et al.* notes that the orientation of the Cu-Mo self-assembled multilayers can be controlled by deposition rate and temperature [16]. The multilayers forming vertical or horizontal phase separated regions, termed concentration modulations as they consist of alternating elemental layers, exhibit similar plastic flow localization as the sequentially deposited films. However, the films grown with randomly orientated phase-separated regions and semi-coherent interfaces

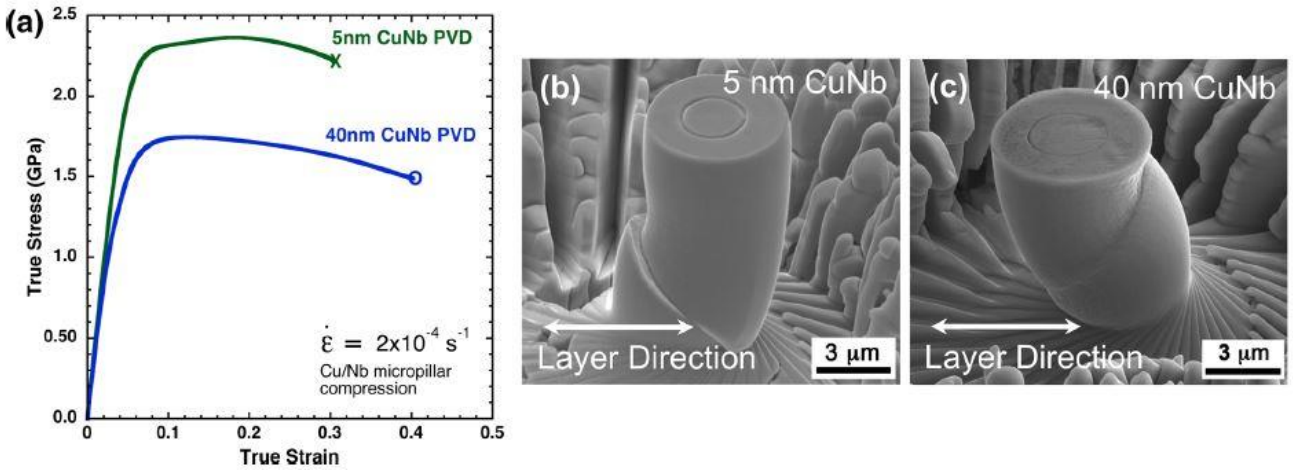

Figure 1-2: Micropillar compression results of Cu-Nb multilayer films (a) with corresponding SEM micrographs for samples at both (b) 5 nm and (c) 40 nm layer thickness. Note, the pronounced material strength is affected by significant shear banding forming across the layers leading to abrupt failure. Adapted from [17].

provide a more homogenous stress distribution as evidenced with nanopillar compression [19]. The random orientated concentration modulations have a tortuous topography which inhibits collective interfacial rotation and limits the distance of shear propagation. The nanopillar compression revealed a yield strength of the Cu-Mo semi-coherent random concentration modulation (RCM) nanocomposite to be 2.4 GPa with a layer thickness of 25 nm, only slightly lower than multilayer nanocomposites with fine 5 nm multilayer thickness [19].

The success of the RCM nanocomposites in stress homogenization prompted exploration into other self-assembled microstructure morphologies. Co-depositions of immiscible Cu-Mo at reduced deposition rates and elevated deposition temperatures produced unique multimodal microstructure morphologies previously unexplored in thin film systems [20,21]. Multimodal morphologies require multiple characteristic length scales to describe the microstructure. The multimodal morphologies observed in immiscible alloy metallic thin films can be categorized as hierarchical microstructures. The term “hierarchical” stems from the idea that the microstructure morphologies are composed of structure which themselves have structure and are the product of atomic species moving along multiple kinetic pathways during film deposition and synthesis. Fig. 1-1(c) displays a 2-D version of a hierarchical morphology. Fig. 1-3 shows both a monomodal morphology, Fig. 1-3(a), and a multimodal hierarchical morphology, Fig. 1-3(b). The Cu-Mo system presented the hierarchical morphology with features on two length scales. Microscopically, large Cu-rich agglomerates were surrounded by alternating Cu-Mo layers. On the nanoscale, a significant population of Mo nanoprecipitates were interspersed throughout the Cu-rich agglomerate. [20].

Akin to the RCM morphologies, the Cu-Mo hierarchical morphologies show stress homogenization under uniaxial compression. The multimodal structures suppressed shear band

formation the tortuous Cu-Mo alternating layers inhibit interfacial slip preserving the macroscopic strength despite the large Cu-rich agglomerates [22]. Such tortuous regions can be seen in Fig. 1-3(b) and have the ability to arrest interfacial shear analogous to that of RCM morphologies. Furthermore, the hierarchical Cu-Mo films exhibited significant crack growth resistance. Crack tip deflection occurred via localized shear at the Cu-Mo interfaces and the Cu-rich agglomerates were strengthened by the Mo nanoprecipitates to provide a ductile, yet strong, crack blunting to the oncoming tip [23]. It can be concluded that the Cu-Mo hierarchical morphologies receive a mechanical advantage from features on both characteristic length scales: shear band suppression and resistance to interfacial sliding from the macroscopic features, and ductile necking and crack blunting from the Cu-rich domains.

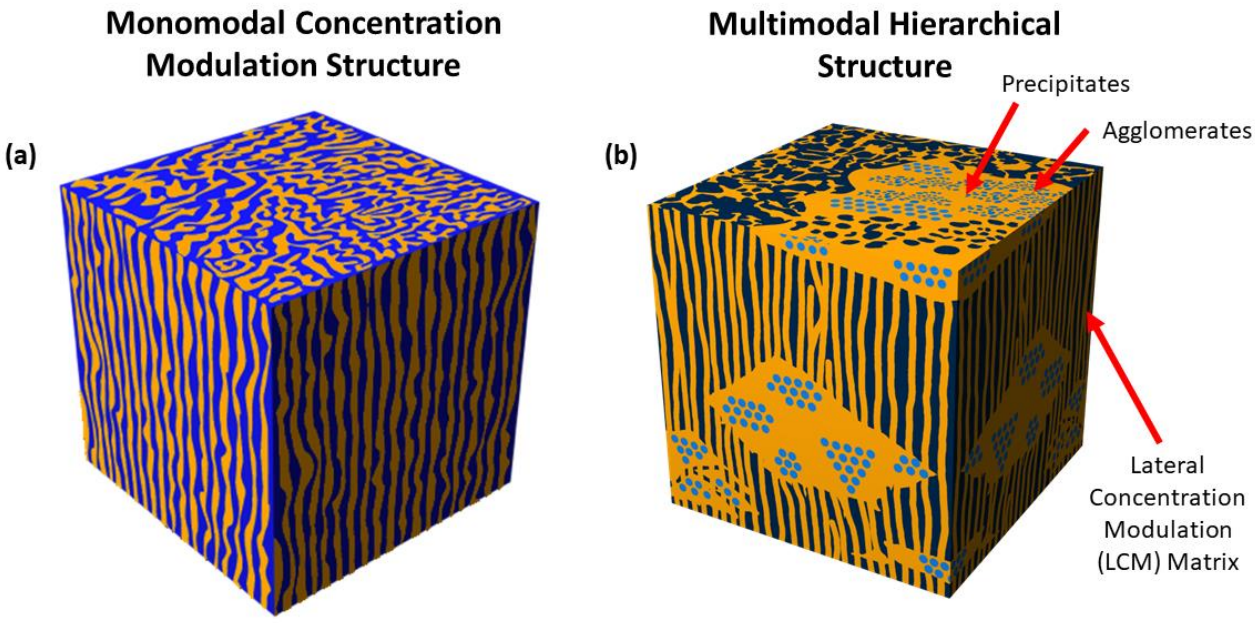

Figure 1-338: 3-D Cartoon visualizations of the (a) monomodal concentration modulation with a single characteristic length for the concentration modulation spacing. (b) A multimodal hierarchical morphology displaying two length scales one for the concentration modulations and agglomerates, a second for the nanoprecipitates embedded in the agglomerates

Having demonstrated the value in studying these hierarchical morphologies, the remainder of this introductory chapter will discuss the processing-microstructure relationship for thin films co-sputtered via physical vapor deposition, followed with a consideration of the phase separation mechanisms of bulk materials. Both topics will elaborate on the phenomena driving self-assembly in immiscible alloy thin films during deposition. The goal is to elucidate the complex phase separation driving force and kinetic pathways responsible for the bimodal nature of hierarchical morphologies seen in co-deposited immiscible alloy thin films. Finally, the introduction will cover the mechanical properties of the hierarchical microstructures including any strain rate dependencies that will influence potential performance. Further chapters will expand on material systems and processing parameters tested to determine the desired processing-microstructure-properties relationship for this unique microstructural architecture.

1.1 Microstructural Formation in Co-Sputtered Thin Films

Physical vapor deposition (PVD) sputtering is a reliable method of fabricating thin films with tunable microstructure features. The variety of processing parameters in PVD include substrate selection, substrate rotation speed, deposition temperature, deposition rate, deposition method (concurrent or sequential deposition), inert gas pressure, and use of a substrate bias [24]. Variations in any of these parameters can significantly influence film microstructure even within the same film material, e.g. changing the grain geometry from equiaxed to columnar or depositing a laminar film versus a film with significant porosity. The exact influence of deposition temperature, inert gas pressure, and deposition rate on ultimate film structure has been well studied for specific metal and oxide systems and is present in literature sources in the form of structural zone diagrams, useful for predicting film structures for thick, single phase films

[25]. Pairing the structural zone diagrams with concepts of island grain growth in film deposition [26] provides a basis from which to study multi-phase thin film microstructure evolution.

The PVD process works by employing an external power source to induce a plasma over a target placed inside a deposition gun. An inert gas is flowed into the chamber where it interacts with the plasma and becomes ionized in the local region surrounding the target. The deposition gun contains a cathode below the target that attracts the charged species and causes them to bombard the target, thereby sputtering the target material that deposits onto a substrate, that could be stationary or rotating. With plasma formation, the sputtering process of PVD is melting point indiscriminate allowing the co-deposition of species with sharp discrepancies in elemental melting temperatures such as Cu and Mo which have melting temperatures of 1084 ºC and 2620 ºC, respectively [24].

In co-sputtered thin films, multiple targets are concurrently activated to deposit various species on the substrate surface. The landing atoms, termed adatoms, land on the substrate surface and will diffuse a limited distance, controlled by their kinetic energy and the deposition rate, as they nucleate and form grains on the film surface. Similar to the single-phase island growth [26], the species of adatoms will move to either wet the surface to form wide, equiaxed grains or minimize surface area contact and form narrow, columnar grains depending on the surface energy of the substrate and the deposited material interface [27]. Specific assumptions about the flux of material on the film surface and the kinetics of the individual species will be covered in the following section of the introduction. The formation of these islands and subsequent grains would be the end result of co-deposited materials that form a solid solution. The co-deposition of immiscible alloys adds an additional layer of complexity with a thermodynamic driving force encouraging phase separation during film deposition. As the

depositing species will not mix, each element will have a distinct kinetic process, opening the potential for a multi-step kinetic pathway to form multimodal architectures.

1.2 Thermodynamic Driving Force for Phase Separation in Immiscible Systems

Co-deposited systems with limited solubility of the components will self-segregate during thin film deposition. For the alloys selected in this work, the immiscibility stems from a very high heat of mixing, ΔH, ranging from 24 kJ/mol in Cu-Ta [28] to 35 kJ/mol in Cu-W [29], a difference in crystal structure, and atomic size. The present studies focus on Cu, a ductile metal with FCC lattice structure, paired with various refractory metals in the Group V and VI of the periodic table. The Group V and VI metals include Ta, Mo, Nb, and W, all of which have a BCC lattice and accentuated hardness in bulk deformation. Other important factors influencing the selection are % misfit for {111} Cu and {100} BCC interplanar spacing, ranging from 7% misfit for Cu-Mo to 12% misfit for Cu-Ta, shear modulus mismatch, and density mismatch [30]. In the studied Cu-BCC systems there is nearly complete compositional immiscibility at the processing temperatures range for PVD, 23 ºC to 800 ºC.

As stated, the constituent elements of co-deposited immiscible alloys will self-segregate into phase regions with orientations dictated by the processing parameters. Defining these regions and orientations: concentration modulation structures are alternating phase layers with atomically sharp interfaces. The phase layers can separate into alternating layers perpendicular to the growth direction, termed vertical concentration modulation (VCM), parallel to the growth direction, termed lateral concentration modulation (LCM), or in random, intertwined orientation, termed random concentration modulations (RCM). The modulation orientations can be controlled by changing the kinetics of the landing adatoms as will be discussed in the following subsection. An example of the three orientations is provided in Fig. 1-4, adapted from a study of

Cu-Mo which displayed all three morphology orientations at differing deposition temperatures [16].

With the significant ΔH, a driving force of phase separation results in surface segregation and limited depth-dependent bulk diffusion during film growth. The phase separation is encouraged by the curvature in the Gibbs free energy describing a system with high ΔH. Figure 1-5 demonstrates a Gibbs free energy curve for a binary alloy containing a region of limited solubility. Thermodynamic stability in the system is possible when the curvature is positive, $\frac{\partial^2 G}{\partial x^2} > 0$. Each local minima in the curve represents a phase in thermodynamic equilibrium. The system becomes unstable at points where the curvature is negative and will phase-separate to form regions with compositions corresponding to the thermodynamic equilibria. *Ipso facto*, solubilities in the system are defined by the inflection points in the free energy, $\frac{\partial^2 G}{\partial x^2} = 0$, which are marked by small 'x's on Fig. 1-5. Small perturbations at these inflection points will induce spontaneous phase separation to the equilibrium compositions, which are the pure components in the case of Cu-BCC immiscible alloys [31 , 32]. The likely mechanism for phase separation in co-deposited films is spontaneous spinodal decomposition of the solid which is the relevant de-mixing process for compositions between inflection points on the Gibbs free energy curve. This is supported by experimental observation of "uphill diffusion" regimes noted in evolution of Cu-Mo microstructures in which local regions Cu or Mo will diffuse contrary to the chemical potential gradient to phase separate [16 , 20].

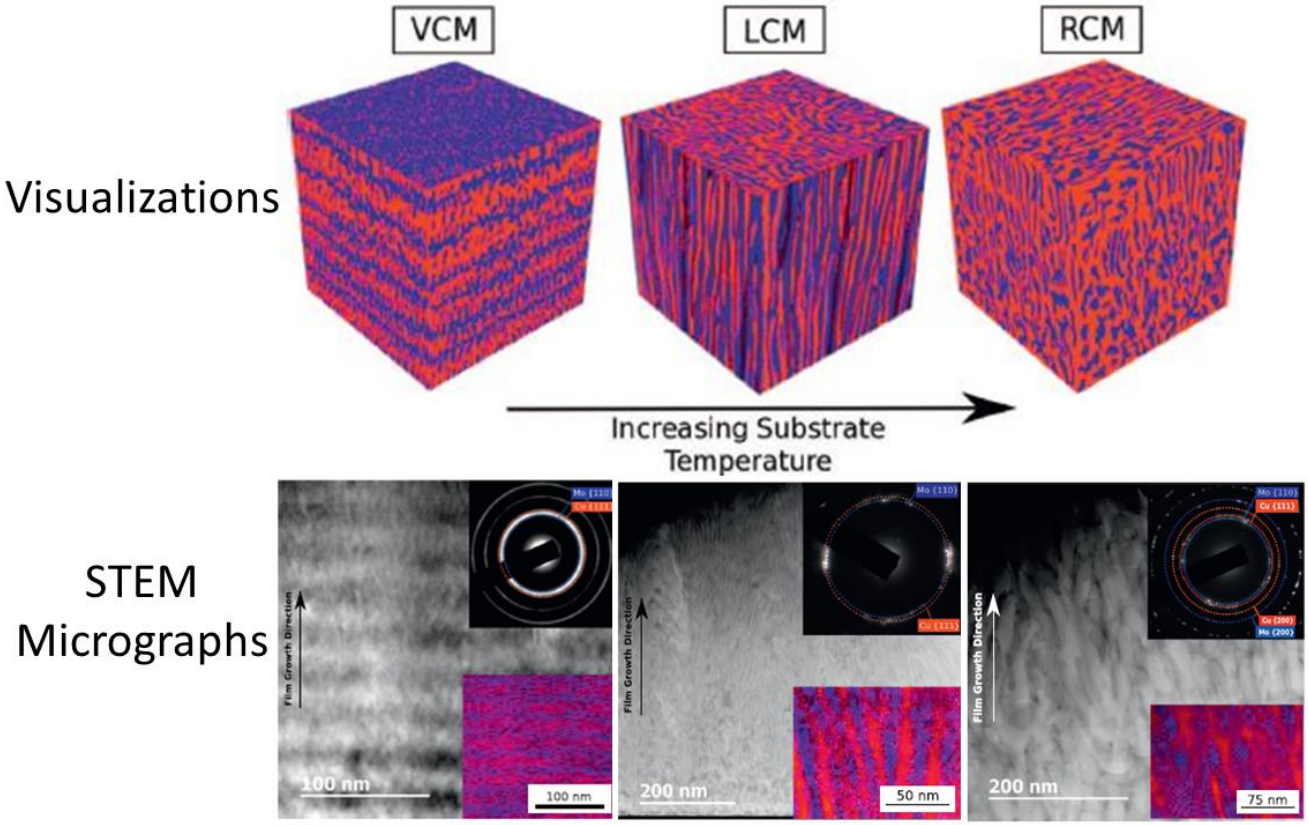

Figure 1-339: (top row) 3D schematics of co-deposited Cu-Mo sputtered at three distinct deposition temperatures 400, 600, and 800 ºC (from left to right) which self-assembled into distinct concentration modulation orientations. (bottom row) Scanning transmission electron microscopy (STEM) cross-sectional micrographs with elemental contrast of the three Cu-Mo corresponding experimental films. Figure adapted from [16].

As the landing adatoms contact the substrate surface, they will phase separate and diffuse a limited distance to reduce the free energy of the system. The surface self-segregation phenomena is well-understood and can be effectively modeled on the mesoscale with a modified version of the Cahn-Hilliard equation by assuming a conservation of mass in the computational domain. The Cahn-Hilliard expression used to simulate phase separation of Al-Si thin films is [33]:

$$F = \int_V [f(c) + \frac{\alpha^2}{2}(\nabla c)^2]dV \qquad (1\text{-}1)$$

In which, F is the total free energy of an inhomogeneous system, $f(c)$ is the chemical free energy density, α is the gradient energy coefficient, c is the concentration field, with the expression integrated with respect to volume, V. Multiple phase-field models have successfully applied the modified Cahn-Hilliard expression in forms similar to Eqn. 1-1 to replicate segregation in monomodal RCM, VCM, and LCM structures [21, 33, 34].

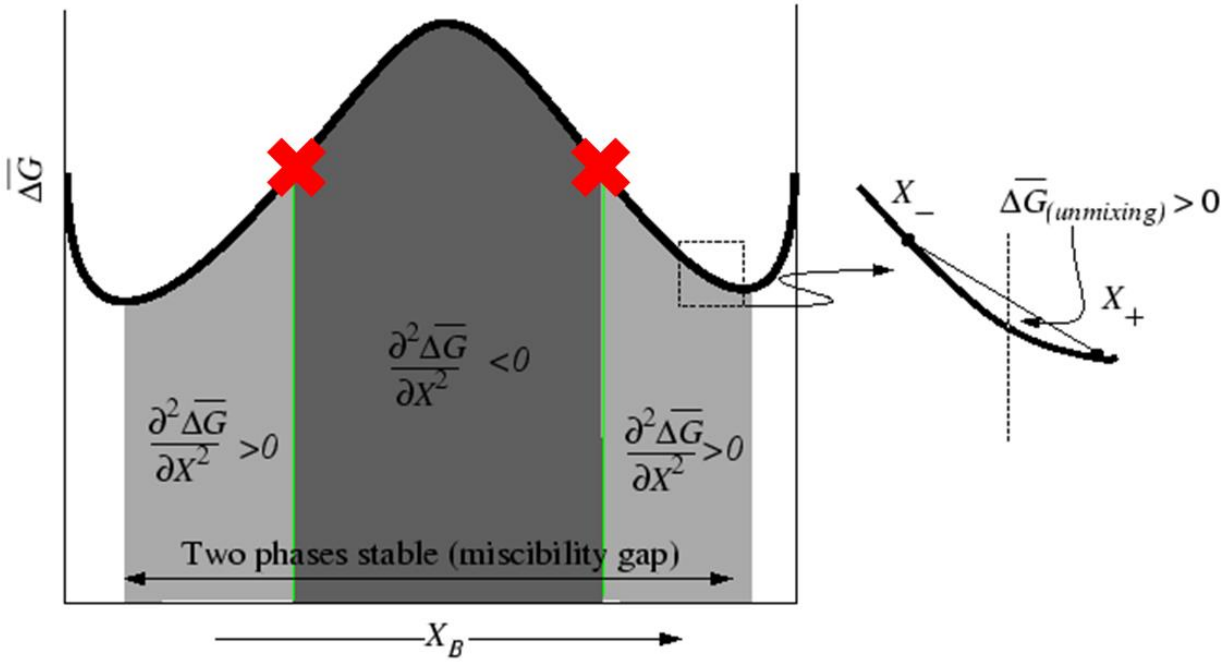

Figure 1-5: Gibbs free energy curve as a function of composition of a secondary element, B. The second derivative of the free energy with respect to composition denotes phase stability. The inflection points, noted with the red X's, are the stability transition points. The light gray regions promote downhill diffusion to the compositions at the energetic minima while the darker gray region (between the X's) encourages spinodal decomposition with short-range demixing with the potential for regions of "uphill" diffusion.

1.3 Kinetics of Phase Separation

As all the deposited immiscible systems have a similar phase-separating driving force, it is useful to frame the systems in terms of the kinetics of the adatoms arriving on the film surface.

While the physical mechanisms that lead to phase separation in bulk materials also occur in films, the process is complicated by two factors as outlined by Atzmon *et al.* [36]: 1) deposition occurs at a fixed, externally imposed rate, and 2) atomic transport occurs preferentially along the advancing surface. The implication is that surface diffusion is the dominant mechanism for film material flux and phase separation at the temperatures relevant to the current work. This makes it distinct from phase separation occurring during post-deposition annealing which is chiefly facilitated by bulk diffusion [37]. The prevalence of surface diffusion stems from the elemental surface diffusivity being orders of magnitude higher than that for bulk diffusivity. In literature, Al-Ge films deposited at 375°C for half an hour yielded bulk interdiffusion lengths of ~5 nm compared to surface interdiffusion lengths of ~400 nm [38]. In the present case, a "frozen bulk" approximation may be applied in which any elemental bulk diffusion is minimal and nearly negligible for films deposited at lower temperatures. As deposition temperatures increase, the contribution of bulk diffusion to microstructure development becomes more significant especially for films sputtered at T≥800°C. Additionally, the adatoms kinetics can be manipulated with variations in deposition rate and temperature. It is important to note that during magnetron sputtering the adatoms land on the substrate with a finite incident kinetic energy. The changes in processing deposition rate and temperature further add to the elevated kinetic energy.

In the PVD process, a landing adatoms will traverse a specific distance along the film surface before being buried under oncoming material deposition flux. The distance is termed the surface interdiffusion length, ρ, and is a consequential parameter for phase-separated morphologies. The Atzmon *et al.* model describes the surface interdiffusion length as [36] :

$$\rho = \sqrt{\frac{D_s \delta}{\nu}} \tag{1-2}$$

Where D_s is the surface diffusivity of the species, δ is the thickness of the most recently deposited layer (on the order of interatomic spacing), and ν is the deposition flux. In immiscible alloy systems, the adatoms will locally de-mix to minimize system energy which influences the subsequent layers and grow into the homogeneous phase-separated regions. The likely method for de-mixing is spinodal decomposition occurring on the surface layer, encouraging adatom movement before they are buried and "frozen" by the next oncoming layer. The deposition flux, ν, is in direct competition with the rate of phase separation as increases in ν equate to abbreviated surface interdiffusion lengths. The surface interdiffusion length and the mobility of an elemental adatom are related due to their mutual dependence on diffusivity [33].

The surface diffusivity,D_s, is reliant on the species deposited, A, B, for the binary alloy. The surface diffusivity is given by the well-known expression [24]:

$$D_s = D_0 \exp\left(\frac{-Q}{k_b T}\right) \tag{1-3}$$

Where D_0 is a diffusivity coefficient, Q is the activation energy required for the movement of an atom to an available adjacent site, k_b is Boltzmann's constant [24] and T is temperature. Coupling Eqns. 1-2 and 1-3 reveals the sensitivity of ρ to temperature and deposition rate which can both be varied as processing parameters.

The surface interdiffusion length provides a theoretical calculation for the size of phase-separated regions in the immiscible alloy microstructures. An example of this is the variance of Al and Ge phase-separated domain sizes observed in Al-Ge films co-deposited at various temperatures [38]. Additionally, the spacing between Cu-rich hillocks in co-deposited Cu-Ta thin films [39], approximately 300 nm in distance, aligned with calculated surface interdiffusion lengths for the Cu species.

In addition to surface interdiffusion length and species' diffusivity, a third kinetic parameter has a significant effect on film microstructure morphology. We must consider the direct influence of the deposition temperature on the movement of an individual species. The impact of increased deposition temperature on the relative mobility of an element can be quantified with the homologous temperature, T_H. The homologous temperature can be defined as:

$$T_H = \frac{T_{Processing}}{T_{Melting}} \tag{1-4}$$

With $T_{Processing}$ being the PVD processing temperature and $T_{Melting}$ being the melting temperature of a specific element, in Kelvin. The adatoms of a species is considered highly mobile at T_H > 0.35 [20]. Assessed T_H values provide a means of comparing the mobility of co-deposited species. For example, at a PVD deposition temperature of 400°C of a co-deposition of Cu-Mo, the T_H of Cu is 0.495 and T_H of Mo is 0.232 indicating high mobility for Cu adatoms and low mobility for Mo adatoms. It should be noted that diffusivity, D_s, is a function of temperature, and hence, T_H is a more explicit contrast of elemental adatom kinetics.

The arguments posed in the present subsection are based on well-studied self-segregation of monomodal morphologies. The focus of this thesis is to use the definitions of phase-separation thermodynamic and kinetics of PVD processes to characterize the formation mechanism responsible for multimodal microstructures. The presence of multiple characteristic lengths in hierarchical structures suggest a multi-step kinetic pathway with features evolving concurrently on multiple length scales. The multi-scale evolution is like that was observed in two-phase (α + β) Ti alloys [40]. In the two-phase Ti alloy system, the Gibbs free energy expression contains multiple energetic minima, driving segregation into distinct phases based on stability and processing conditions including intermediate phase decomposition. Of relevance is the bimodal

mechanism for microstructure formation in the Ti alloy which forms the same distinct microstructure on two separate length scales via a multi-step process. Treating the Ti system as an analog, the Cu-BCC hierarchical microstructures with multimodal morphologies are likely formed as a complex interplay between thermodynamic phase separation and surface diffusion kinetics relevant for PVD processing.

1.4 Mechanical Behavior of Metallic Thin Films

The work will focus on the final leg of the triangular processing-microstructure-properties relationship: determining the mechanical performance of the multimodal morphologies as thin film functional coatings via nanoindentation. The present work will focus on uniaxial loading of the hierarchical morphologies, comparing their performance to literature multilayer and monolithic films composed of the same elements. The nanoindentation properties are examined across multiple strain rates to determine any strain rate sensitivity which can be critical as key deformation mechanisms can vary significantly as the loading conditions change from quasi-static to shock loading. All nanoindentation in the present work are conducted with a Berkovich tip geometry which is a standard, triangular-faceted tip. Since it is a three-sided pyramid it is geometrically self-similar, and has a total included angle of 142.3° and a half-angle of 65.27°.

Seminal work by Oliver and Pharr extracted two key parameters characterizing thin film mechanical behavior with nanoindentation: Young's modulus, E, and hardness, H [41]. The load-displacement behavior can be expressed with Eqn. 1-5:

$$\frac{(1-\nu^2)}{E} = \frac{1}{E_r} - \frac{(1-\nu_i^2)}{E_i} \qquad (1\text{-}5)$$

where E and ν are the Young's modulus and Poisson's ratio of the film, and E_i and ν_i are the same properties for the indenter. The E_r is a measured mechanical property taken during the unloading step of the nanoindentation to gauge the elastic deformability of the specimen. The hardness is expressed as:

$$H = \frac{P_{max}}{A} \tag{1-6}$$

where P_{max} is the peak indentation load and A is the contact area of the indent. Whereas E is a measure of the material's elastic deformation properties, H is a measure of the material's resistance to permanent plastic deformation. The H calculation is highly sensitive to the calculated contact area, A, of the indenting tip. Both E and H are measured with units of pascals, typically in the range of MPa for E and GPa for H depending on the material. Fig. 1-6 presents an overview of a typical load-displacement curve taken during nanoindentation of a sample surface. Adjacent to the loading-unloading curve is an SEM micrograph of a nanoindentation into a Cu-Mo multilayer film at a strain rate of $\sim 1 \times 10^3$/s.

Several flaws during indentation may arise to distort the measured E and H values. Material displacement during indentation can distort the contact area and generate artificial H values. This is especially true with highly malleable materials such as Cu, which has a Young's Modulus of 121 GPa [24], that can exhibit material shifting and pile-up at the edges of the indentation causing an overestimation in hardness and elastic modulus values [42]. Further issues include the substrate affecting the film's properties, inconsistent mechanical performance as a function of indentation depth or due to surface defects, and insufficient data resolution in the unloading regime for accurate E calculation. There is a plethora of literature regarding theoretical and experimental improvements to the original Oliver and Pharr model, formalism by Saha and Nix [42] presents stiffness as a measurable property and normalizes the applied load by

the square of the stiffness to provide a metric insensitive to indentation depth and contact area. Other work by Merle *et al.* [43] represents the indenter as a damped harmonic oscillator to relax assumptions of elasticity which become constraining at high strain rate indentation.

Indentation at different strain rates will activate distinct deformation mechanisms that vary based on the crystalline structure of the constituent element material. In the present work, both the Cu and BCC Group V, VI metal have variable mechanical response at different loading conditions. Compressive loading of Cu at room temperature and at quasi-static strain rates (1×10^{-3}/s to 1×10^{0}/s) generates dislocations which slip through grains in the microstructure [44]. The low stacking fault energy of Cu, which has a FCC crystal lattice, promotes the formation of partial dislocations which ultimately leads to twin formation at high strain rate ($\sim 1 \times 10^{3}$/s to 1×10^{5}/s) and dynamic ($> 1 \times 10^{5}$/s) loading conditions [45]. A sample Group V BCC element, Ta, has a relatively high stacking fault energy which indicates that dislocation slip dominates the deformation behavior at quasi-static to high strain rate loading (1×10^{-3}/s to 1×10^{5}/s). Specific conditions of reduced temperature, 77 K, and severe strain localization will induce twinning in Ta at high strain rates [46]. Otherwise, Ta will undergo twinning only in response to dynamic or shock loading conditions ($> 1 \times 10^{6}$/s) [47]. The significant caveat to this discussion is the microstructure grain size which will ultimately influence any recrystallization, grain boundary sliding or grain boundary rotation which may occur in either Cu or Ta.

Strain rate sensitivity can provide a qualitative understanding of the changing deformation mechanisms as a function of strain rate. The strain rate sensitivity, m, is given by the expression:

$$m = \frac{\ln \sigma_{flow}}{\ln \dot{\epsilon}} \tag{1-7}$$

with σ_{flow} being the material's flow stress and $\dot{\epsilon}$ is the strain rate. The flow stress can be approximated with nanoindentation as $\sigma_{flow} \sim H/3$. The experimental measurement of H, E,and m can be used to directly compare the mechanical properties of hierarchical morphologies to multilayer and concentration modulation morphologies in immiscible alloy systems.

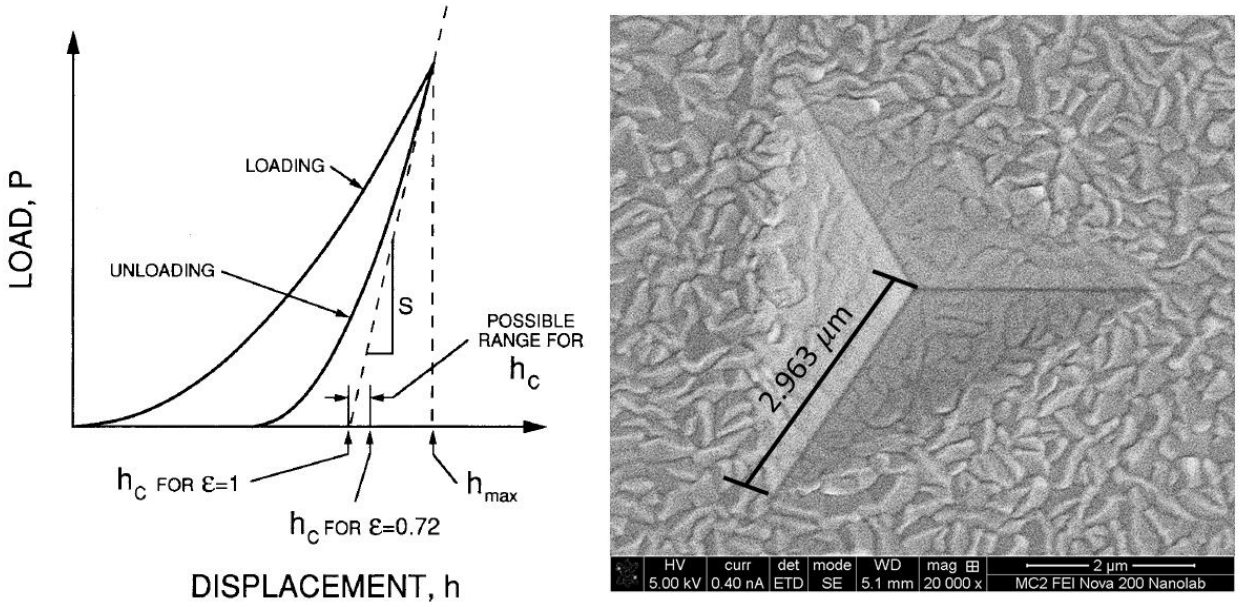

Figure 1-6: (left) Load, P, and displacement, h, sample curve that is acquired during nanoindentation. The elastic modulus is calculated from the sharp, localized, first derivative with respect to displacement (noted on graph as h-critical) at the beginning of the unloading curve, and the hardness is calculated using the maximum load from this curve. Further properties of stiffness and compliance can be evaluated. (right) sample nanoindentation onto a thin film surface. Image from [41].

1.5 Present Work, Included Studies, and Hypothesis

The focus of this dissertation will be to determine the processing-microstructure-properties relationship for hierarchical morphologies that arise in co-deposited immiscible alloy thin films. The work will build upon the present understanding of phase-separating systems used

to describe monomodal systems, increasing the complexity to incorporate the formation of multimodal morphologies.

The proceeding chapters will cover the following topics: Chapter 2 illustrates the experimental methods and processing parameters used to probe the conditions necessary for hierarchical structures to form. Chapter 3 describes the self-organization of co-deposited Cu-Ta thin films under a variety of kinetic conditions. The Cu-Ta microstructure is characterized in terms of cross-sectional microstructure and thin film surface topology. Chapter 4 is a comprehensive examination of multiple co-deposited immiscible alloys in order to systematically identify the processing parameters and conditions necessary for hierarchical growth. Microscopy of deposited films is used to elucidate the kinetic pathways likely responsible for multimodal growth. The presence of metastable states on the smaller characteristic length scale are also considered. Chapter 5 applies a mesoscale modeling framework to study the effect of a localized compositional driving force on microstructural evolution. Chapter 6 completes the mechanical characterization of the co-deposited immiscible thin films at strain rates applicable to commercial nanoindentation. Finally, Chapter 7 concludes the work and introduces topics for future research and discussion.

In this dissertation, we hypothesize that the formation of multimodal hierarchical microstructures is possible in the conditions of low deposition rate, elevated deposition temperature during a co-deposition of metallic immiscible alloy films via PVD. The kinetic condition necessary is the significantly enhanced mobility of one species relative to the other during the film growth process. The phase-separation of the equimolar co-deposited films occurs simultaneously on both macroscopic and nanoscopic length scales, influenced by local regions of highly disparate composition which promote precipitate formation at the nanoscale. Ultimately,

the unique architecture will display advantageous mechanical properties in comparison to monolithic films of the constituent elements. The mechanical results will be highly contingent on microstructural heterogeneities and will display limited strain rate sensitivity at the loading rate range tested by a commercial nanoindenter (1×10^{-3}/s to 1×10^{3}/s).

References

[1] M. Mozetic. Surface modification to improve properties of materials. *Materials*, 12:441, 2019.

[2] A. Chen, Q. Su, H. Han, E. Enriquez, and Q. Jia. Metal oxide nanocomposites : a perspective from strain , defect , and interface. *Advanced Materials*, 31:1803241, 2019.

[3] Y. Zhao and G. Lu. First-principles simulations of copper diffusion in tantalum and tantalum nitride. *Physical Review B*, 79:214104, 2009.

[4] M. C. Rao and M. S. Shekhawat. A brief survey on basic properties of thin films for device application. *International Journal of Modern Physics: Conference Series*, 22:576–582, 2013.

[5] P. Fratzl and R. Weinkamer. Nature's hierarchical materials. *Progress in Materials Science*, 52:1263–1334, 2007.

[6] A. Khalajhedayati, Z. Pan, and T. J. Rupert. Manipulating the interfacial structure of nanomaterials to achieve a unique combination of strength and ductility. *Nature Communications*, 7:10801, 2016.

[7] S.Shao, H.M. Zbib, I.N. Mastorakos, and D.F. Bahr. Deformation mechanisms, size effects, and strain hardening in nanoscale metallic multilayers under nanoindentation. *Journal of Applied Physics*, 112:044307, 2012.

[8] E.O. Hall. The deformation and ageing of mild steel: III discussion of results. *Proceedings of the Physical Society - Section B*, 64:747, 1951.

[9] N.J. Petch. The cleavage strength of polycrystals. *The Journal of the Iron and Steel Institute*. 174:25-28, 1953

[10] A. Misra, J. P. Hirth, and R. G. Hoagland. Length-scale-dependent deformation mechanisms in incoherent metallic multilayered composites. *Acta Materialia*. 53:4817–4824, 2005.

[11] M. J. Buehler and A. Misra. Mechanical behavior of nanocomposites. *MRS Bulletin*. 44:19–24, 2019.

[12] J. Y. Zhang, J.J. Niu, X. Zhang, P. Zhang, G. Liu, G.J. Zhang, and J. Sun. Tailoring nanostructured Cu / Cr multilayer films with enhanced hardness and tunable modulus. *Materials Science and Engineering A*. 543:139–144, 2012.

[13] Y. Chen, N. Li, D.C. Bufford, J. Li, K. Hattar, H. Wang, and X. Zhang. In situ study of heavy ion irradiation response of immiscible Cu / Fe multilayers," *Journal of Nuclear Materials*. 475:274–279, 2016.

[14] J. Wang, R. G. Hoagland, J. P. Hirth, and A. Misra. Atomistic simulations of the shear strength and sliding mechanisms of copper–niobium interfaces. *Acta Materialia*. 56:3109–3119, 2008.

[15] T. Xie, L. Fu, X. Cao, J. Zhu, W. Yang, D. Li, and L. Zhou. Self-assembled binary immiscible Cu-transition metal multilayers prepared by co-sputtering deposition. *Thin Solid Films*. 705:138037, 2020.

[16] B. Derby, Y. Cui, J. K. Baldwin, and A. Misra. Effects of substrate temperature and deposition rate on the phase separated morphology of co-sputtered, Cu-Mo thin films. *Thin Solid Films*. 647:50–56, 2018.

[17] N. A. Mara and I. J. Beyerlein. Review : effect of bimetal interface structure on the mechanical behavior of Cu – Nb fcc – bcc nanolayered composites. *Journal of Materials Science*. 49:6497–6516, 2014.

[18] Y. Cui, N. Li, and A. Misra. An overview of interface-dominated deformation mechanisms in metallic nanocomposites elucidated using in situ straining in a TEM. *Journal of Materials Research*. 34(9):1469-1478, 2019.

[19] Y. Cui, B. Derby, N. Li, and A. Misra. Design of bicontinuous metallic nanocomposites for high-strength and plasticity. *Materials and Design*. 166:107602, 2019.

[20] B. Derby, Y. Cui, J. Baldwin, R. Arróyave, J. Demkowicz, and A. Misra. Processing of novel pseudomorphic Cu – Mo hierarchies in thin films. *Materials Research Letters*. 7(1): 1-11, 2019.

[21] K. Ankit, B. Derby, R. Raghavan, A. Misra, and M. Demkowicz. 3-D phase-field simulations of self-organized composite morphologies in physical vapor deposited phase-separating binary alloys. *Journal of Applied Physics.* 126:075306, 2019.

[22] Y. Cui, B. Derby, N. Li, N. A. Mara, and A. Misra. Suppression of shear banding in high-strength Cu/Mo nanocomposites with hierarchical bicontinuous intertwined structures. *Materials Research Letters*. 6(3):184-190, 2018.

[23] Y. Cui, B. Derby, N. Li, and A. Misra. Fracture resistance of hierarchical Cu–Mo nanocomposite thin films. *Materials Science & Engineering A*. 799:139891, 2021.

[24] M. Ohring. *Materials Science of Thin Films*. Elsevier, 2001.

[25] J. A. Thornton. Influence of substrate temperature and deposition rate on structure of thick sputtered Cu coatings. *Journal of Vacuum Science & Technology*. 12(4): 830-835, 1975.

[26] C. V Thompson and R. Carel. Stress and grain growth in thin films. *Journal of the Mechanics and Physics of Solids*. 44(5): 657-673, 1996.

[27] C. V Thompson. Structure evolution during processing of polycrystalline films. *Annual Review of Materials Science*. 20:159-190, 2000.

[28] M. Nastasi, F.W. Saris, L. S. Hung, and J.W. Mayer. Stability of amorphous Cu/Ta and Cu/ W alloys. *Journal of Applied Physics*. 58:3052-3058, 1985.

[29] T. Raghu, R. Sundaresan, P. Ramakrishnan, and T. R. R. Mohan. Synthesis of nanocrystalline copper–tungsten alloys by mechanical alloying. *Materials Science and Engineering A*. 306:438–441, 2001.

[30] F. T. N. Vüllers and R. Spolenak. From solid solutions to fully phase separated interpenetrating networks in sputter deposited " immiscible " W–Cu thin films. *Acta Materialia*. 99:213-217, 2015.

[31] A. J. Bray. Theory of phase-ordering kinetics. *Advances in Physics*. 51(2):481-587, 2002.

[32] W.C. Carter. Class Lecture, Topic: "Spinodal Decomposition." 3.00, Massachusetts Institute of Technology, Massachusetts, USA, Dec. 2002.

[33] K. Fukutani, K. Tanji, T. Saito, T. Den. Fabrication of well-aligned Al nanowire array embedded in Si matrix using limited spinodal decompositon. *Japanese Journal of Applied Physics*. 47(2):1140-1146, 2008.

[34] J. A. Stewart and R. Dingreville. Microstructure morphology and concentration modulation of nanocomposite thin-films during simulated physical vapor deposition. *Acta Materialia*. 188:181-191, 2020.

[35] G. Kairaitis and A. Galdikas. Mechanisms and dynamics of layered structure formation during co-deposition of binary compound thin films. *Coatings*. 10:21, 2020.

[36] M. Atzmon, D.A. Kessler, and D.J. Srolovitz. Phase separation during film growth. *Journal of Applied Physics*. 72:442, 1992.

[37] C. M. Muller, S. Parviainen, F. Djurabekova, K. Nordlund, and R. Spolenak. The as-deposited structure of co-sputtered Cu–Ta alloys, studied by X-ray diffraction and

molecular dynamics simulations. *Acta Materialia*. 82:51-63, 2015.

[38] C.D. Adams, M. Atzmon, Y.T. Cheng, D.J. Srolovitz. Phase separation during co-deposition of Al-Ge thin films. *Journal of Materials Research*. 7(3):653-666, 1992.

[39] M. Powers, B. Derby, E. Raeker, N. Champion, and A. Misra. Hillock formation in co-deposited thin films of immiscible metal alloy systems. *Thin Solid Films*. 693:137692, 2019.

[40] T. W. Heo, D. S. Shih, and L.Q. Chen, Kinetic pathways of phase transformations in two-phase Ti alloys. *Metallurgical and Materials Transactions A.* 45:3428-3445, 2014.

[41] W. C. Oliver and G. M. Pharr. An improved technique for determining hardness and elastic modulus using load and displacement sensing indentation experiments. *Journal of Materials Research*. 7(6):1564-1583, 1992.

[42] R. Saha and W. D. Nix. Effects of the substrate on the determination of thin film mechanical properties by nanoindentation. *Acta Materialia*. 50:23-38, 2002.

[43] B. Merle, W. H. Higgins, and G. M. Pharr. Extending the range of constant strain rate nanoindentation testing. *Journal of Materials Research.* 35(4): 343-352, 2019.

[44] Z. S. Basinski and S. J. Basinski. Dislocation distributions in deformed copper single crystals. *Philosophical Magazine*. 9:51-80, 2006.

[45] U. Andrade, M. A. Meyers, K. S. Vecchio, and A. H. Chokshi. Dynamic recrystallization in high-strain, high-strain-rate plastic deformation of copper. *Acta Metallurgica et Materialia*. 42(9):3183–3195, 1994.

[46] H. Lim, J. D. Carroll, C. C. Battaile, T. E. Buchheit, B. L. Boyce, and C. R. Weinberger. Grain-scale experimental validation of crystal plasticity finite element simulations of tantalum oligocrystals. *International Journal of Plasticity*. 60:1–18, 2014.

[47] B. Jiang, A. Tu, H. Wang, H. Duan, S. He, H. Ye, and K. Du. Direct observation of deformation twinning under stress gradient in body-centered cubic metals. *Acta Materialia*. 155:56-68, 2018.

Chapter 2

Experimental and Computational Methods

We employ a two prong, experimental and computational approach to test the hypotheses of the previous chapter and establish the processing-microstructure-properties relationship for hierarchical morphologies in immiscible alloy thin films. Thus, this methodology chapter is divided into two sections. The first section focuses on the experimental component with the fabrication of metallic thin films via co-deposition of model face-centered cubic (FCC) and body-centered cubic (BCC) under a variety of processing conditions. The first section includes the electron microscopy characterization techniques and the nanoindentation performed on the film surfaces. The second section emphasizes the phase-field modeling framework used to determine the compositional influence on the material flux and microstructure formation during film growth. The simulation framework is reviewed along with the relevant input conditions.

2.1 Co-Deposition of FCC-BCC Immiscible Alloys Metallic Thin Films with DC Magnetron Sputtering

As mentioned in the previous chapter, we select Cu and a refractory metal from the Group V or VI of the periodic table, including Ta, Mo, Nb, and W, as the model FCC-BCC alloy systems. The rationale is twofold, stemming from the desired microstructure and mechanical properties. The Cu-BCC pairing is nearly completely immiscible across a wide compositional and temperature range, up to approximately the melting point of Cu in some cases [1].

Furthermore, Cu-BCC will not form intermetallics which would significantly embrittle the material.

The introductory chapter hypothesized that the hierarchical structure forms as the result of simultaneous phase-separating activity occurring on separate length scales facilitated by the kinetic activity of one highly mobile element and one relatively immobile element during the co-deposition of an immiscible system. We predict that elevated deposition temperatures and low deposition rates will encourage larger differences in surface interdiffusion lengths that promote the agglomeration necessary for hierarchical formation. To test these hypotheses, different Cu-BCC systems were co-deposited to probe the relative mobility of the constituent species and how that influences any preferential agglomeration. The BCC metals include Ta, Mo, and Fe. Ag was used in some instances for a comparative FCC metal with a mobility close to that of Cu at elevated temperatures.

All thin films were co-deposited onto thermally oxidized Si substrates by DC magnetron sputtering in a Kurt J Lesker PVD 75 deposition system. The substrates were 3'' diameter Si with a 1000 nm thick SiO_2 surface layer. Before deposition, the substrates were ultrasonically cleaned in acetone, rinsed with isoproponal alcohol, and dried with filtered compressed air. Five different 2'' diameter targets were used (Cu, Mo, Ag, Fe, Ta), all with at least 99.95% purity, for the various combinations of the binary alloys and sole ternary alloy. The alloys were deposited at equimolar compositions to generate bicontinuous morphologies and prevent the targeted formation of discrete particles. The targets were oriented confocally with a 5'' throw distance towards a rotating substrate at 10 rpm. The sputtering occurs in a vertical direction with the targets depositing material upwards onto the substrates. Base pressure in the chamber prior to sputtering was less than 2.7×10^{-5} Pa or 2.02×10^{-7} Torr. The process gas of Ar was

maintained at a pressure of 3 mTorr during operation. The Ar partial pressure was selected to minimize the number of voids captured in the film during deposition and to reduce the residual growth stresses present in the BCC phases in the microstructure [2,3]. The vacancies in the present experiment had a minimal, negligible effect on film microstructure and properties.

Precise deposition rates were governed by controlling the DC power supplied to each target. For any film fabrication at an elevated deposition temperature, a substrate heater resistor coil would heat and maintain a requisite temperature throughout the deposition period. The deposition temperature was monitored with a thermocouple located between the heater and the substrate. The specific deposition rates and temperatures varied as we explored different factors that influence hierarchical formation, and so those parameters will be specified in each chapter. Fig. 2-1 is a diagram of the PVD chamber showing the co-deposition of two species under direct current magnetron sputtering.

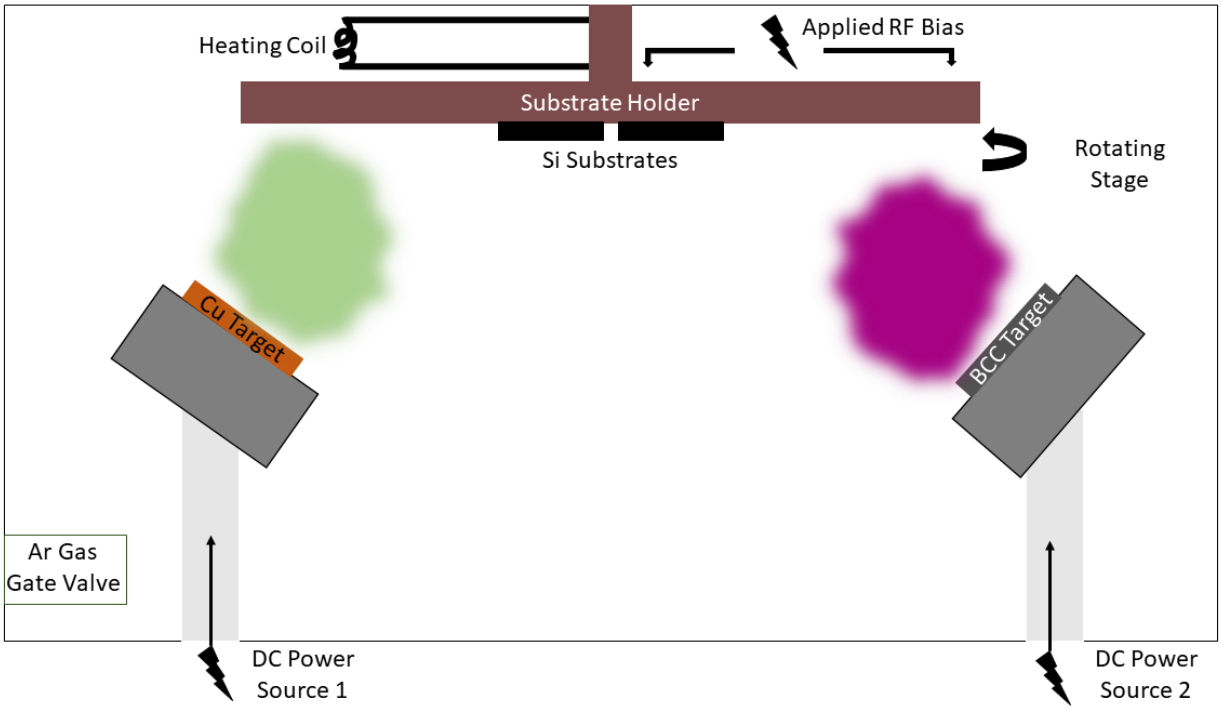

Figure 2-1: Schematic of two target co-deposition in a PVD chamber. Note, the heating element is an external component above the substrate that heats the substrate holder plate which in turn heats the Si substrates during deposition.

2.2 Experimental Characterization

2.2.1 X-Ray Fluorescence Spectroscopy

The bulk composition of the alloy films was confirmed via x-ray fluorescence spectroscopy (XRF) using a Rigaku Supermini200. To ensure accurate composition, targeted scans in the keV energy ranges for the Cu Lβ, Ta Mα, Mo Kα, Fe Kα, and Ag Lα peaks were performed in addition to a general sweep of metallic elemental peaks. Therefore, each film was scanned a total of eight times with Gaussian peak fits were applied to reduce noise. The average standard deviation in composition was <3.5 at. %.

2.2.2 X-Ray Diffraction

X-ray diffraction (XRD) with a Rigaku SmartLab XRD with a Cu source (λ=1.54 Å) was used to determine the phase composition and crystallographic texture in the film samples. The samples were mounted onto a thin film stage that was aligned for optimal signal-to-noise ratio. An initial XRD scan was run continuously at 2θ range from 10° to 90° with a speed of 4°/second and a step size of 0.02°. To increase data resolution, a second detailed scan was run at 2θ from 32° to 52° with s scanning speed of 1°/second and a step size of 0.005°. The data peaks were normalized to reduce the influence of the background noise. The XRD results for the Cu-Ta films are depicted in the following chapter [4].

2.2.3 Transmission Electron Microscopy and Scanning Transmission Electron Microscopy

Scanning/transmission electron microscopy (S/TEM) foils were prepared using focused ion beam (FIB) milling techniques in a TFS Helios 650 Nanolab SEM/FIB and a TFS Nova 200 Nanolab SEM/FIB. The foils were lifted out and attached to either Si or Mo grids to prevent interference during chemical composition scans. After thinning, the samples were plasma cleaned for a period of 5 to 8 minutes prior to S/TEM characterization on two microscopes, JEOL 3100R05 double-Cs corrected S/TEM and JEOL 200 C-ARM (used for one-time access in the Cu-Ta characterization). The JEOL 3100 R05 was operated at 300 keV to achieve a point-to-point resolution of 0.055 nm for high angle annular darkfield (HAADF) and brightfield (BF) imaging. The convergent angle for all image collection 111° with a camera length of 8 cm to true elemental Z-contrast HAADF imaging. Energy dispersive X-ray spectroscopy (EDS) compositional maps were collected using a JEOL SDD X-ray detector with a 60 mm^2 active area. The JEOL 200 C-ARM was similarly employed with a 200 keV working voltage [4, 5, 6].

Scanning electron microscopy (SEM) images were taken using both secondary electron (SE) and backscattered electron (BSE) detection techniques. SEM images of film surfaces were taken with the aforementioned TFS Helios and TFS Nova microscopes. The surface indentation imaging was performed with a Tescan Mira3 FEG SEM.

2.2.4 Nanoindentation

A Hysitron TI 950 Triboindenter equipped with a diamond Berkovich tip was used to make indentations on the Cu-Ta film surfaces. A quick study of the indentation depths revealed substrate effects influenced mechanical response at depths exceeding 200 nm. Thus, experimental indentation data was collected at an indentation depth of 100 nm with force-controlled indentations to maintain a constant strain-rate during the loading-unloading cycle. To gauge Cu-Ta strain rate sensitivity, the indentations were applied over the strain rate range of $5 \times 10^{-3}\ s^{-1}$ to $10\ s^{-1}$ [7]. The Hysitron TI 950 is a conventional nanoindentor with tip displacement controlled by capacitance plate. Figure 2-2 is a diagram of the components in a capacitance plate nanoindenter. Limitations in the capacitance gauge resolution and data collection rates for tip displacement mean the Hysitron TI 950 cannot accurately measure displacement or load at strain rates exceeding $10\ s^{-1}$. Rates exceeding $10\ s^{-1}$ require deformation modeling with higher level approximations for material loading and higher data acquisition rates achievable with a laser receiver and piezoelectric activation to accurately evaluate displacement and load [8,9].

Indentations for strain rate sensitivity testing were spaced approximately 10 microns from each other and were organized in grids. A series of targeted indentations tested the effect of surface topology and underlying microstructure in the Cu-Ta. In this case, the indentations were directly on top of flattened regions and into protruding surface grains to test the self-assembled microstructure features.

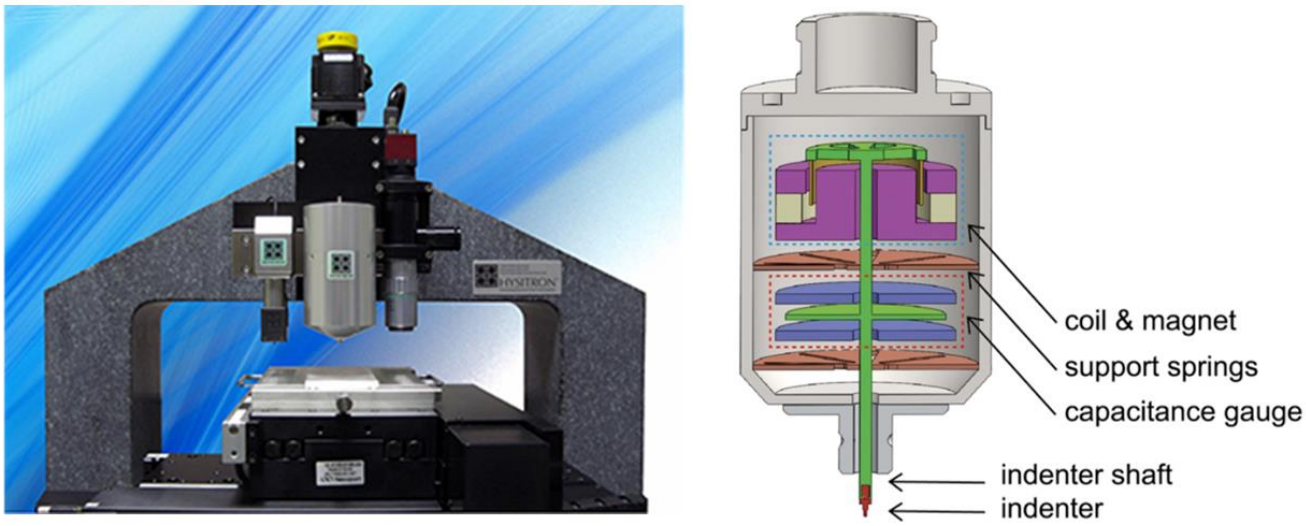

Figure 1198: (left) Sample Hysitron TI 950 Nanoindentator configuration, the Berkovich is installed in the middle loading column on the right is a high resolution optical camera and on the left is an optional loading column [10]. (right) A cross-sectional view of the loading column with a capacitance gauge to control force/displacement of the Berkovich tip indenter.

2.3 Mesoscale Modeling and Computational Approach

The mesoscale modeling presented in this work is an application of the coding framework "Mesoscale Multiphysics Phase-Field Simulator" (MEMPHIS) established by Stewart and Dingreville [11]. We simulated the deposition and growth of Cu-Mo thin films as a function of deposition conditions using the PVD phase-field model in the MEMPHIS framework [11, 12, 13, 14]. This model has been shown to capture a broad range of experimentally observed concentration modulations dependent on inputted deposition conditions and processing parameters. Figure 2-3 shows the PVD model successfully replicating a number of monomodal morphologies with concentration modulations at variable orientations. The model accounts for major aspects of the PVD process including: (i) the deposition of the incident vapor phase of a binary alloy onto a substrate, (ii) surface interdiffusion, and (iii) the subsequent phase ordering in the resulting inhomogeneous thin film.

In this model, the total free-energy functional used to describe the dynamics of the system is a function of two order parameters, one, ϕ, describing the vapor-solid transition and two, c, for the compositional ordering during thin film growth. For the evolution of the compositional field, we solve the Cahn-Hilliard equation in the solid thin film, using structurally and compositionally dependent mobility function. The free energy, $\mathcal{F}$, is given by:

$$\mathcal{F} = \int \left\{ f_\phi + \frac{\kappa_\phi^2}{2}(\nabla\phi)^2 + s(\phi)\left(f_c + \frac{\kappa_c^2}{2}(\nabla c)^2\right) \right\} d\Omega \qquad (2\text{-}1)$$

With κ_ϕ and κ_c representing gradient energy coefficients that influence structural and compositional homogeneity. The $s(\phi)$ is an interpolation function that separates the compositional effects in the vapor and solid phases with the expression $(1+\phi)^2/4$. The f_ϕ and f_c are functions representing the equilibrium Gibbs' free energy functionals for the solid-vapor and alloy phases respectively, typically represented with double-well functions with two minima representing two energetically favorable states.

The mobility function has the form:

$$M_c(\phi, c) = M^{bulk} + M^{surface} \qquad (2\text{-}2)$$

with an embedded switching function in the bulk mobility, M^{bulk}, and surface mobility $M^{surface}$expressions to effectively enforce separate solid diffusivities on the surface and in the bulk of the thin film. We describe the kinetics of thin film growth by solving the Cahn-Hilliard equation for the vapor-solid field variable and include a source term to couple thin film evolution to incident vapor flux. The transport and evolution of the incident vapor flux towards the thin film surface is modeled via the convection-diffusion equation. Elastic effects were neglected in this study. Further details on this model can be found in Ref. [11].

We numerically solved the set of coupled partial differential equations using the finite-difference method with second-order central difference stencils for all spatial derivatives. All simulations were performed in two-dimensions on uniform numerical mesh of 512x512 grid points with dimensionless numerical and physical parameters and a time step of $\Delta t = 10^{-2}$. The mobilities for Cu and Mo are based on calculated mobility and observation from experimental depositions [15]. The bulk mobility values for Cu and Mo are $8.17 \times 10^{-4} \frac{cm^2}{s/eV}$ and $1.37 \times 10^{-10} \frac{cm^2}{s/eV}$, respectively. The inputted bulk mobilities for both species were adimensionalized and their corresponding surface mobilities were set an order of magnitude greater. We simulated a dimensionless deposition rate of 0.8, which, based on the size of our computational domain and diffusivity parameters selected, corresponds to a 0.8 nm/s for a 1-μm-thick film. We used this model to simulate three different deposition conditions. The first condition corresponds to the deposition of a homogeneous 50-50 at.% alloy composition in the vapor for which we do not expect hierarchical structure formation. The second and third deposition conditions simulate a local imbalance in the phase composition near the surface of the thin film in order to test our hypothesis. For these last two conditions, we considered that the vapor composition was at 90-10 at.% composition in some localized region of the computational domain while the remainder of the vapor domain remained at 50-50 at.% composition. A small and large localized region for the imbalance in the vapor composition were considered in the second and third deposition conditions, respectively. Further detail on the simulation conditions can be found in Chapter V.

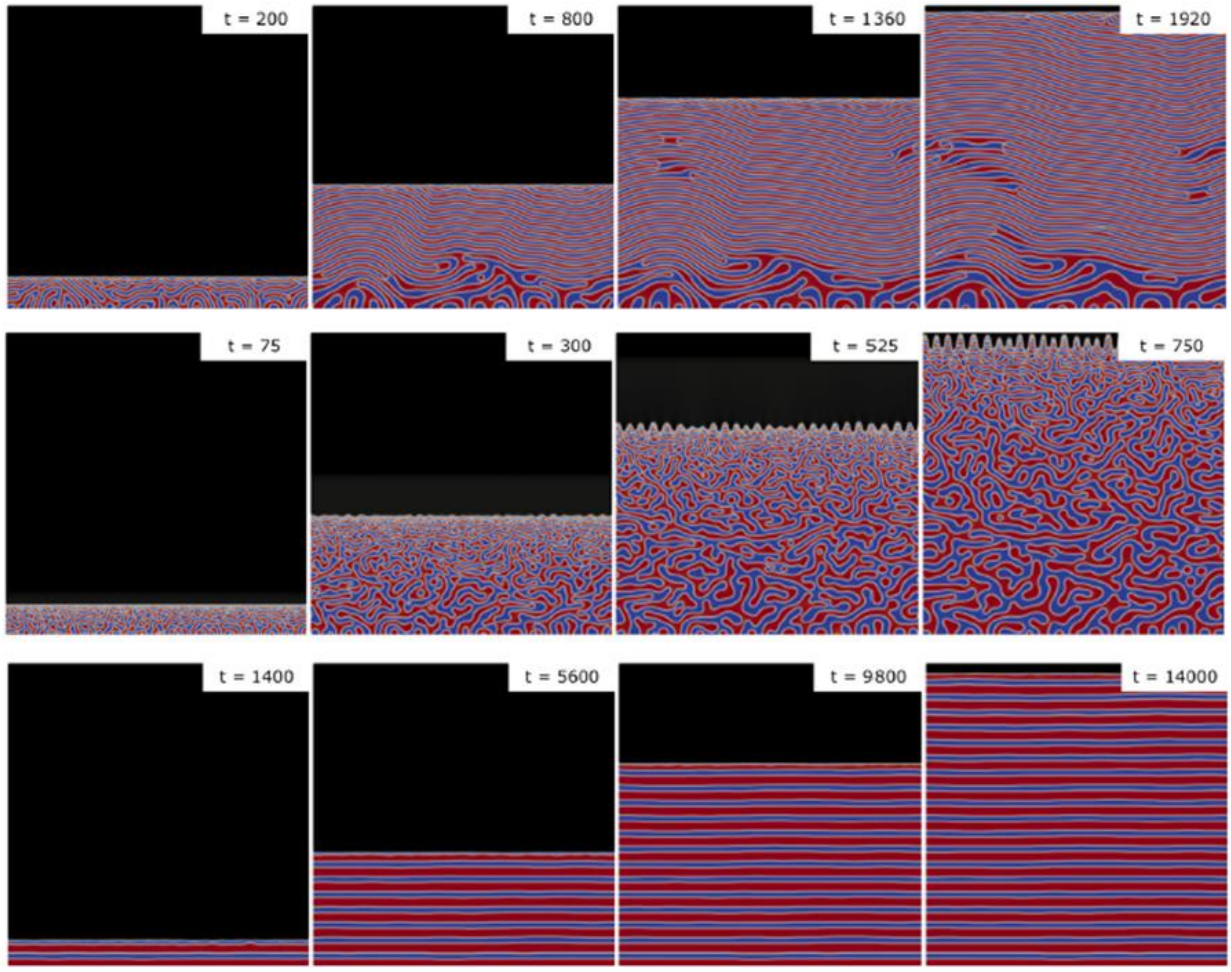

Figure 2-3: Co-deposition of two species using the MEMPHIS PVD coding framework simulating three different deposition rates. The spinodal decomposition and surface diffusion yields three distinct concentration modulation orientations (see Fig. 1.4), all monomodal morphologies. Figure adapted from Ref. [11].

References

[1] H.J. Lee, K.W. Kwon, C. Ryu, R. Sinclair. Thermal stability of a Cu/Ta multilayer: an intriguing interfacial reaction. *Acta Materialia*, 47(15):3965-3975, 1999.

[2] Y. G. Shen. Effect of deposition conditions on mechanical stresses and microstructure of sputter-deposited molybdenum and reactively sputter-deposited molybdenum nitride films. *Materials Science and Engineering A*, 359:158-167, 2003.

[3] D.W. Hoffman and J. A. Thornton. Internal stresses in Cr, Mo, Ta, and Pt films deposited by sputtering from a planar magnetron source. *Journal of Vacuum Science and Technology*, 20:355-358, 1982.

[4] M. Powers, B. Derby, A. Shaw, E. Raeker, A. Misra. Microstructural characterization of phase-separated co-deposited Cu-Ta immiscible alloy thin films. *Journal of Materials Research*, 35:1531-1542, 2020.

[5] M. Powers, B. Derby, S.N. Manjunath, A. Misra. Hierarchical morphologies in co-sputter deposited thin films. *Physical Review Materials*, 4(12):123801, 2020.

[6] M. Powers, B. Derby, E. Raeker, N. Champion, A. Misra. Hillock formation in co-deposition of immiscible metal alloy systems. *Thin Solid Films*, 693:137692, 2020.

[7] E. Raeker, M. Powers, A. Misra. Mechanical performance of co-deposited immiscible Cu-Ta thin films. *Scientific Reports*, 10(1):1-10, 2020.

[8] B. Merle, W.H. Higgins, G.M. Pharr. Extending the range of constant strain rate nanoindentation testing. *Journal of Materials Research*, 4:343-352, 2020.

[9] G. Guillonneau, M. Mieszala, J. Wehrs, J. Schwiedrzik, S. Grop, D. Frey, L. Philippe, J. Breguet, J. Michlet, J. Wheeler. Nanomechanical testing at high strain rates: new instrumentation for nanoindentation and microcompression. *Materials and Design*, 148:39-48, 2018.

[10] Eden Instruments, *TI 950 Triboindenter: Nanomechanical test instrument*. 2021. Accessed on: May 23, 2021. [Online]. Available: https://www.eden-instruments.com/en/nanoindentation-platforms/ti-950-triboindenter-nanomechanical-test-instrument

[11] J. A. Stewart and R. Dingreville. Microstructure morphology and concentration modulation of nanocomposite thin-films during simulated physical vapor deposition. *Acta Materialia*. 188:181-191, 2020.

[12] K. Ankit, B. Derby, R. Raghavan, A. Misra, and M. Demkowicz. 3-D phase-field simulations of self-organized composite morphologies in physical vapor deposited phase-separating binary alloys. *Journal of Applied Physics.* 126:075306, 2019.

[13] J.A. Stewart and D.E. Spearot. Phase-field models for simulating physical vapor deposition and grain evolution of isotropic single-phase polycrystalline thin films. *Computational Materials Science*. 123:111-120, 2016.

[14] E. Herman, J.A. Stewart, R. Dingreville. A Data-driven surrogate model to rapidly predict microstructure morphology during physical vapor deposition. *Applied Mathematical Modeling*. 88:589-603, 2020.

[15] M. Ohring. *Materials Science of Thin Films*. Elsevier, 2001.

Chapter 3

Microstructural Self-Assembly in Co-Deposited Cu-Ta

3.1 Introduction

To reiterate, the focus of the present work is to establish the processing-microstructure-properties relationship for hierarchical morphologies in immiscible alloy thin films. Previous work emphasized hierarchical morphologies in Cu-Mo films [1]. Explaining these hierarchical structures requires consideration of the adatoms' relative mobilities. While depositing at elevated temperatures, the mobility of Cu adatoms is orders of magnitude greater than that of Mo adatoms. The resultant calculated surface diffusion length of Cu is significantly larger than Mo which gave rise to a bimodal architecture separated on two length scales with large Cu and Mo regions containing embedded Cu and Mo minority clusters stabilized as metastable phases [1].

The Cu-Mo hierarchical microstructures prompted further exploration into Group V, VI BCC metal pairings. We turn to Cu-Ta, a binary immiscible alloy with closer lattice parameter misfit % than Cu-Mo (8% for Cu-Ta and 13% for Cu-Mo) [2]. Additionally, there is a 44% shear modulus mismatch for Cu-Ta in contrast to Cu-Mo's shear modulus mismatch of 150% [2]. The higher elemental weight and reduced bulk diffusivity of Ta as compared to Mo could be more conducive to hierarchical self-assembly during the phase-separating process of thin film solidification. The Cu-Ta system is well-studied in the semiconductor industry [3] but could have promising nanomechanical applications as evidenced by the high strength of the similar Cu-Nb

system [4]. There is a paucity of research on the processing-microstructure relationship of Cu-Ta and specifically how heterogeneities in the structure will form as the structure self-assembles.

Previous work on PVD co-sputtered Cu-Ta shows that the as-deposited structure will vary with respect to alloy composition [5]. Muller *et al.* reported that across all compositions, the Cu tends to form into a FCC structure while Ta will form into either BCC also noted as α-Ta with BCC structure, or as β-Ta, which is a metastable state with tetragonal structure. In a second work, Muller focuses on as-deposited Cu-34 at.% Ta to deduce the formation mechanism of α or β-Ta [6]. The as-deposited film formed nanocrystalline Cu-Ta grains arranged in a superlattice. Upon annealing at 400 and later 600 °C, the Cu coalesced into clusters inside a β-Ta matrix via spinodal decomposition as proven by signs of "uphill" diffusion in tomographic imaging.

The orientation relationship between phase separated regions provides critical information on the interface character and its influence on mechanical behavior. However, it is difficult to ascertain meaningful orientation relationships in co-sputtered Cu-Ta due to reduced feature size and far-from-equilibrium structures. Work by Kwon *et al.* [7] on consecutively deposited Cu-Ta layers (with β-Ta and FCC Cu phases) depicts a heteroepitaxial relationship at the interface of $\mathrm{Cu}_{(111)[2\bar{2}0]}||\beta\text{-}\mathrm{Ta}_{(001)[3\bar{3}0]}$ observed with electron diffraction. Other work on as-deposited Cu-Ta multilayers denotes metastable β-Ta (002) and Cu (111) preferred texture as seen in x-ray diffraction [8]. After annealing, β-Ta undergoes a phase transformation into α-Ta BCC structure, as identified by six-fold symmetry in the electron diffraction pattern, with a ~2-5 nm thick amorphous interface between Cu-Ta. Co-deposited Cu-Mo [9] and multi-layer Cu-Nb [4] have both shown Kurdjumov-Sachs (K-S) orientation relationship, $\mathrm{Cu}_{(111)[110]}||\mathrm{Mo, Nb}_{(110)[111]}$. Phase separated regions in co-deposited Cu-Ta may organize into K-S, Nishiyama-Wassermann (NW), or a variant orientation relationship.

The objectives of this study are thus enumerated: determine the processing-microstructure relationship of PVD co-deposited Cu-Ta, characterize the microstructure and determine the phases present at multiple length scales with possible crystallographic orientation relationships, and develop an empirical understanding of the self-assembly mechanisms for future development of immiscible alloy systems with tailored mechanical performance.

3.1.1 Sample Fabrication and Characterization

Cu-Ta thin films were co-deposited via the PVD process of DC magnetron sputtering using a pressure chamber with a base pressure $< 6 \times 10^{-7}$ Pa, or $<4.5 \times 10^{-9}$ Torr. The Cu and Ta targets were simultaneously powered to co-deposit a film with 50-50 at. % Cu-Ta composition onto Si-SiO_2 substrates with millimeter thickness. The top 1000 nm of the substrate, contacting the film surface, is SiO_2 while the remainder is Si. The 50 at. % was selected to focus bicontinuous morphologies rather than minority phase segregation of either element. The deposition chamber was a Kurt Lesker PVD 75 with 2'' disk Cu and Ta targets with nominal purities of 99.999% for Cu and 99.95% for Ta with a target throw distance of 5''. The substrates were cleaned with an RF bias of 50 W for 120 seconds before deposition. Cu-Ta films were deposited at a combined co-deposition rate of 1.52 Å/sec to 700 nm thickness at four temperatures: 25 (room temperature), 400, 600, and 800 °C. The DC power supplied to the targets was 40 W for the Cu and 60 W for the Ta. A substrate bias of 20 W was applied to the film and the target was rotated at 10 rotations-per-minute (rpm). The deposition temperature refers to the temperature of the substrate that is heated via a heating coil to a consistent temperature during the deposition. All the films were deposited then left to cool to room temperature in the deposition chamber to prevent oxide formation on the film surface.

The bulk composition of the alloy films was confirmed via x-ray fluorescence spectroscopy (XRF) using a Rigaku Supermini200. X-ray diffraction (XRD) with a Rigaku SmartLab XRD with a Cu source (λ=1.54 Å) was used to determine the phase composition of the four samples. An initial XRD scan was run continuously at 2θ range from 10° to 90° with a speed of 4°/second and a step size of 0.02°. To increase data resolution, a second detailed scan was run at 2θ from 32° to 52° with s scanning speed of 1°/second and a step size of 0.005°.

Scanning/transmission electron microscopy (S/TEM) cross-sectional samples of the film were prepared using focused ion beam milling techniques in a FEI Helios 650 nanolab SEM/FIB. The foils were attached to Mo grids to minimize any interference to compositional mapping. Transmission electron microscopy was performed with a JEOL 2010F AEM with 200 KV voltage. Two scanning transmission electron microscopes, JEOL 2100F STEM and JEOL 200 C-ARM (operated at Northwestern University in a one-use period) operated at 200 keV using Gatan and JEOL detectors were used for high resolution characterization of film cross-sectional samples. Energy dispersive spectroscopy (EDS) on the JEOL 200 C-ARM was used for compositional spatial mapping of the samples.

3.2 Experimental Observations and Results: Monomodal and Multimodal Structures in Cu-Ta

All four deposited films depict prominent phase separation between the co-deposited Cu-Ta. Although the composition of all the films was constant at 50-50 at. % Cu-Ta, as confirmed by XRF, the extent of phase separation and the phases present varied significantly across the 25, 400, 600, and 800 °C films giving each a distinct microstructure morphology. XRD profiles for all four films are shown in Fig. 3-1. In the 25 °C film, one broad peak with low intensity was noted for 2θ from 33 to 39° which is consistent with nanocrystalline (002) and (410) β-Ta. A

low intensity peak at 43° aligns with diffraction of the Cu (111) plane. This agrees with literature [10] that notes β-Ta as the preferred Ta phase for Ta films deposited at room temperature. As previously stated, β-Ta is a metastable state whose stability has previously been affiliated with the presence of oxygen during deposition. Although, recent work has refuted oxygen's stabilizing effect as β-Ta was observed in Ta depositions under ultra-high vacuum [11]. The present work also employed high vacuum conditions, $< 6 \times 10^{-7}$ Pa, which reduces the likelihood of oxygen contributing to β-Ta stability.

The crystalline peaks for β-Ta, α-Ta, and Cu were all present in the XRDs of the 400 to 800 °C films. The location and appearance of the β-Ta diffraction peaks agree with the tetragonal structure and lattice parameter spacings, *a*, *c*, first posed by Read and Altman [12] and later elaborated by Jiang *et al*. [13]. The β-Ta (002) peak is significant in the 400 and 600 °C films but sharply declines in intensity in the 800 °C films. A similar decline with respect to increasing temperatures is true for higher index β-Ta (400) peak. The α-Ta (110) at 38° becomes increasingly prominent with increased deposition temperature. Furthermore, α-Ta (200) and (211) peaks were negligible at 400 °C but become noticeable at 600 and 800 °C. The descent of the β-Ta and rise of the α-Ta peaks with respect to temperatures is likely due to phase transformation from β-Ta to α-Ta that typically occurs at 750 °C [14] but will occur at approximately 400 °C in the presence of Cu as previously noted in a study of Cu-Ta interfaces during annealing [8]. The rationale being that the high deposition temperatures and lengthy deposition time of this experiment are akin to an annealing environment. The metastable and equilibrium phases of Ta will be further discussed later. Cu (111), (200) and (220) peaks were present and maintained the same or increasing intensity with respect to increasing deposition

temperature suggesting a consistent FCC Cu presence for all films deposited at elevated temperatures.

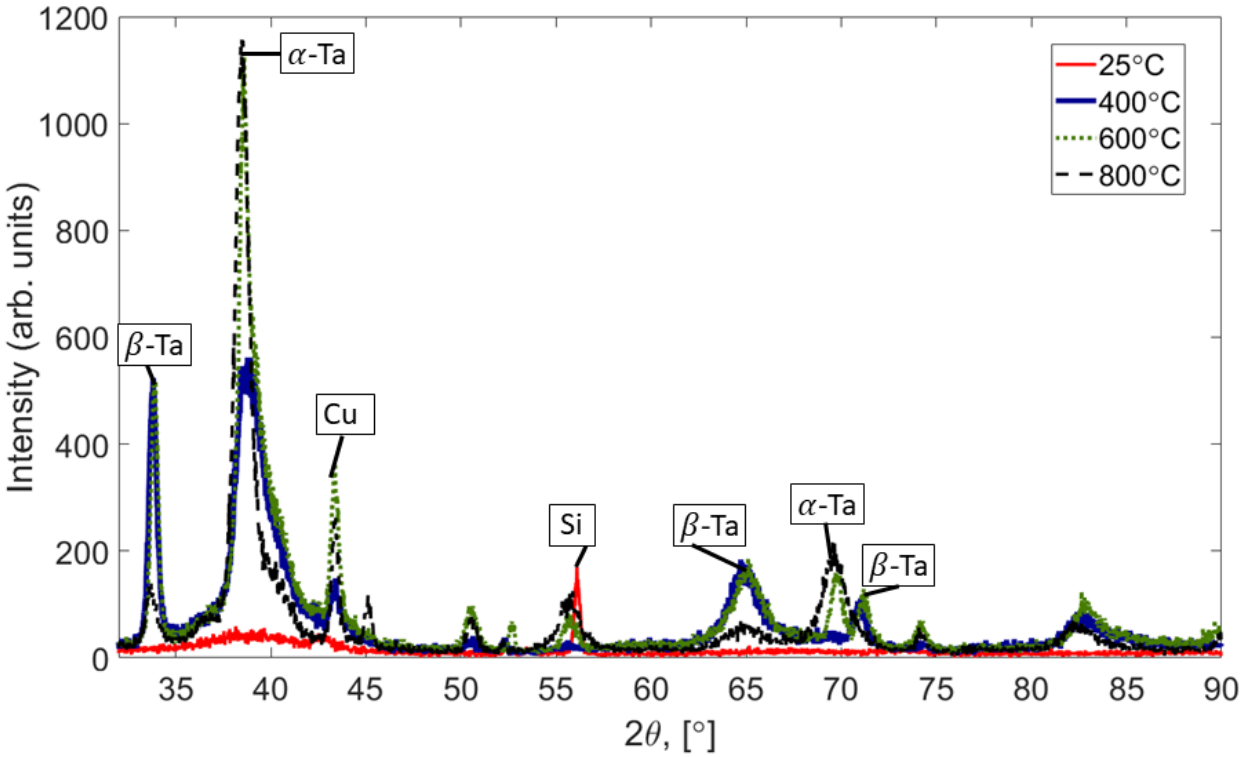

Figure 3-1: XRD spectra of the Cu-Ta films deposited at 25, 400, 600, and 800 °C. The 25 °C film has a broad peak with low intensity and a single sharp peak corresponding to Ta and Cu nanocrystals, respectively. The crystalline content of 400, 600, and 800 °C films greatly increases with high intensity peaks for planes Cu (111), β-Ta (110), and α-Ta (110) and others corresponding those three crystalline phases.

S/TEM micrographs reveal the variant morphology of the four films. Fig. 3-2 contains cross-sectional TEM images of the 25 °C film. EDS mapping of Fig. 2(a) confirms the omnipresence of Cu and Ta across the film. High resolution TEM (HR TEM), Fig. 3-2(b) images show adjacent nanocrystals of Cu and Ta with diameters on the order of ~5 nm homogeneously distributed throughout the film. The selected area diffraction pattern (SADP), Fig. 3-2 (c), of the room temperature film has diffuse concentric rings consistent with a texture-less polycrystalline

microstructure. The ring diameters align with Ta (110), (211) and Cu (111) planar spacings. The polycrystallinity is further supported by the Cu and broad β-Ta crystalline peaks in the XRD spectra of Fig 3-1. Unlike the co-sputtered Cu-34 at. % Ta films reported in the literature [6], the room temperature Cu-Ta film in this experiment did not exhibit any superlattice organization.

Micrographs of the 400 °C film shown in Fig. 3-3 depict interwoven Cu-rich and Ta-rich regions. The Cu-rich and Ta-rich regions form a bicontinuous ribbon-like structure with wavy features oriented perpendicular to the growth direction that are reminiscent of the vertical concentration modulation (VCM) morphology [1]. STEM high angle annular darkfield (HAADF) Z number contrast imaging, Fig. 3-3(a), confirms the wavy nature of the domains and that the average widths of the Ta-rich and Cu-rich bands are 124 ± 5 nm and 83 ± 4 nm respectively. The Ta-rich bands are composed of nanocrystalline grains organized into columns approximately 15 nm in width that are elongated in the growth direction. Striations within the HR TEM image of Fig. 3-3(c) depicts planar defects present within the grains that are likely stacking faults that are generated to relax the high internal stresses that arise during film deposition [2]. It is also plausible the defects are nanoscale growth twins [15] but the resolution of the planar defects is distorted due to a lack of texture within the Ta columns and Angstrom-scale spacing between defect layers. HR TEM imaging, Fig. 3-3(d) within the Cu-rich bands show that the Cu maintains a semi-coherent boundary with the surrounding Ta. Examination of the phase separated interface in and the inset fast Fourier transforms (FFTs) reveal a Kurdjumov-Sachs orientation relationship at the semi-coherent boundary with Cu $<10\bar{1}>$// Ta $<11\bar{1}>$ and Cu (111)//Ta (011). Z-contrast imaging and HR TEM imaging reveals Ta nanocrystals present in limited areas within the Cu-rich bands. The ~4 nm in diameter Ta nanocrystals were likely trapped during the deposition process. Conversely, there are Cu nanocrystals, ~ 5 nm in diameter

present in the Ta columnar grain as seen in Fig 3-3(b) which are identified by FFT (inset) depicting an FCC crystalline structure. The presence of both the Ta and Cu nanocrystals will be further explored in the following paragraphs as the feature fineness at 400 °C increased the difficulty for comprehensive characterization.

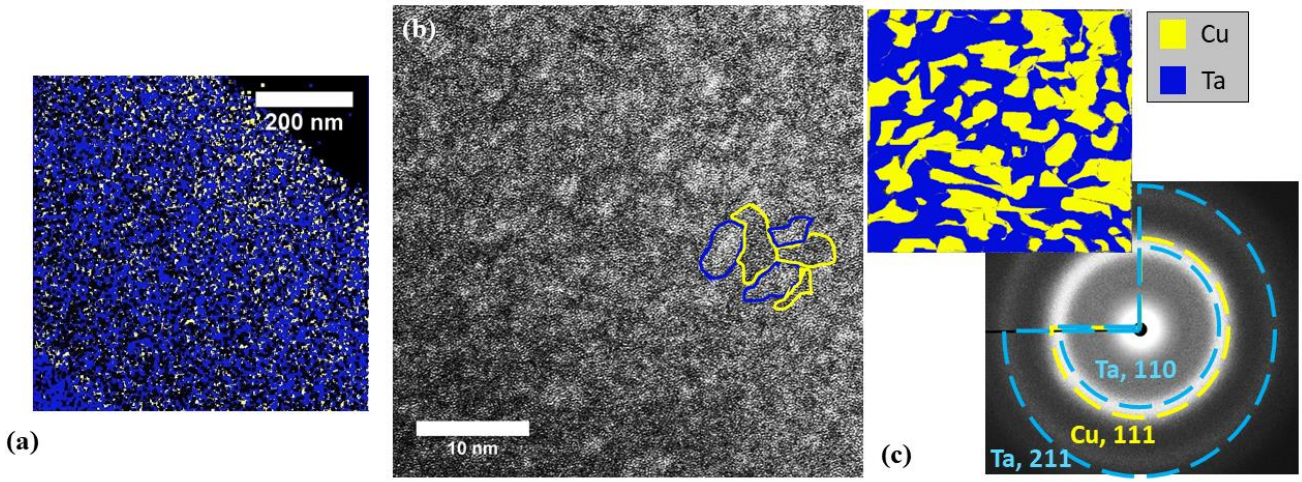

Figure 3-2: Characterization of film deposited at room temperature, **(a)** EDS map of homogenously distributed Cu-Ta nanocrystals, **(b)** HR TEM image of film cross section depicting fine nanocrystalline structure, a few nanocrystals are outlined in the image **(c)** SADP of same section and a cartoon schematic of microstructure colored to represent the phase region distribution in the microstructure

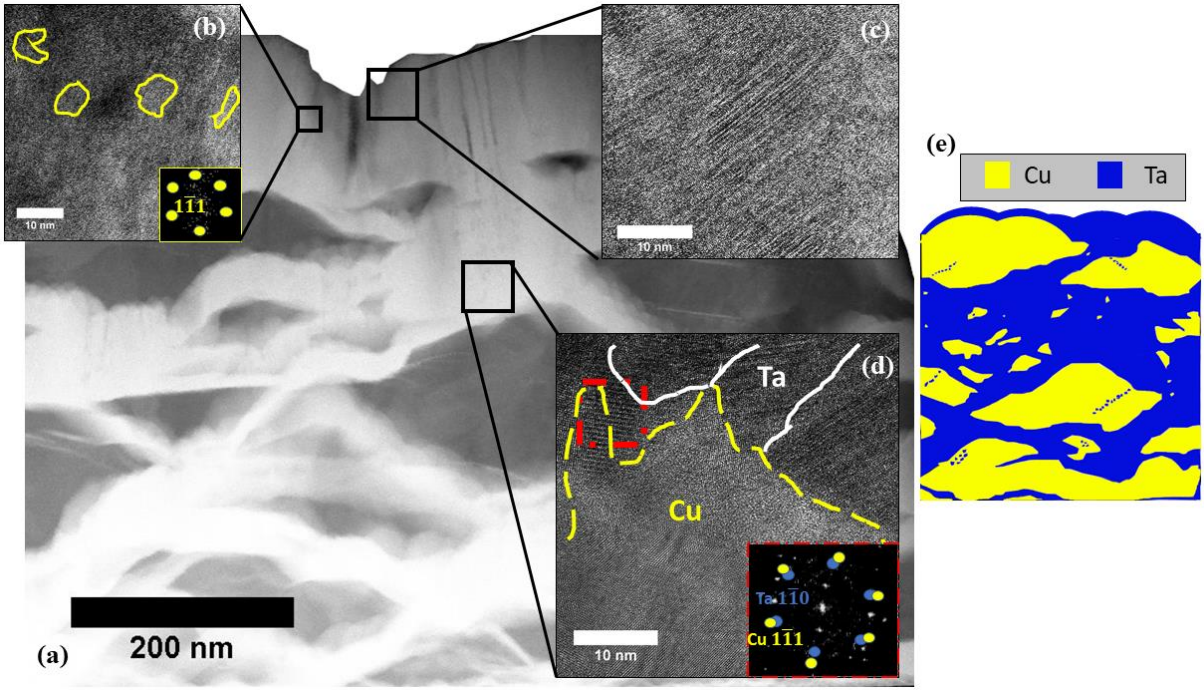

Figure 3-3: (a, background) STEM HAADF micrograph with atomic number contrast of Cu-Ta deposited at 400 °C. The white regions corresponding to Ta and darker regions are Cu bands. Within the Cu bands, trace Ta precipitates are noted. In the Ta-rich bands, Cu nanocrystals are present (b) as confirmed by HR TEM and FFT (inset) revealing a zone axis = $(1\bar{1}0)$ for an FCC Cu structure. (c) HR TEM in Ta-rich band showing planar defects aligned with angle to growth direction of film. (d) HR TEM of semi-coherent interface between Cu band and Ta band. FFT (inset) provides a Kurdjumov-Sachs orientation relationship Cu $<10\bar{1}>$// Ta $<11\bar{1}>$ and Cu (111)//Ta (011) (e) Cartoon schematic of the microstructure.

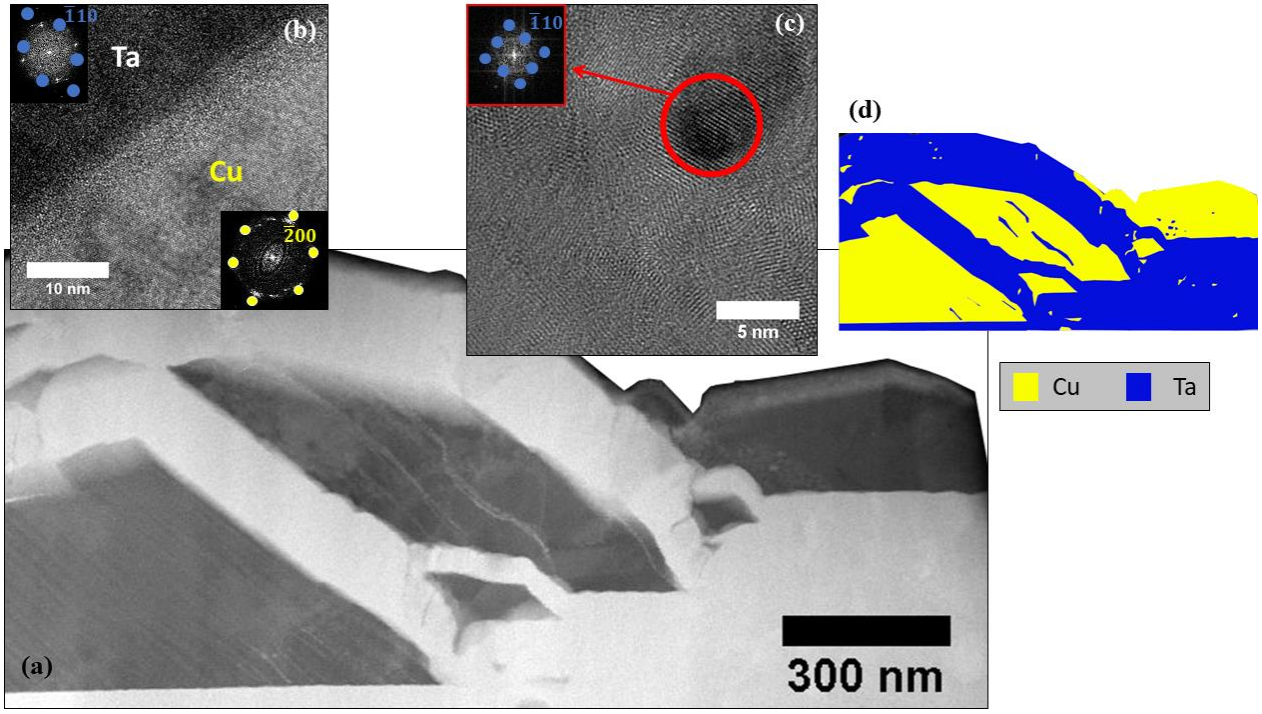

Figure 3-4: (a)STEM HAADF micrograph of Cu-Ta film deposited at 600 °C. White regions are Ta-rich veins and dark regions are Cu-rich agglomerates. (b) HR TEM image of the boundary between Ta veins and Cu agglomerates shows a semi-coherent interface with Nishiyama-Wassermann orientation relationship Cu <0$\bar{1}$1>// Ta <001> and Cu ($\bar{1}$11)//Ta ($\bar{1}$10) as confirmed by FFTs (inset). (c) HR TEM of a single Ta precipitate (encircled in red) in the Cu agglomerate, this is confirmed by FFT (inset) showing BCC Ta crystal, zone axis=<001> (inset). (d) Cartoon schematic of microstructure.

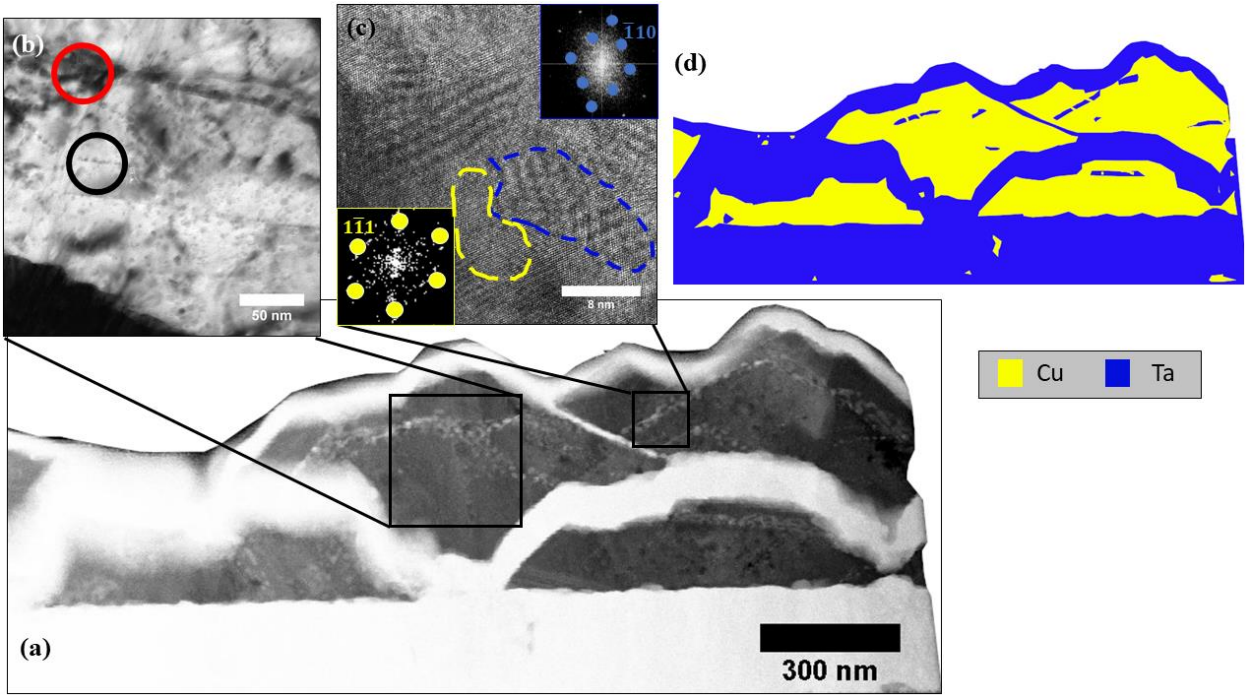

Figure 3-5: (a) STEM HAADF micrograph of Cu-Ta film deposited at 800 °C, white/lighter regions are Ta-rich veins and darker regions are Cu-rich agglomerates. (b) Brightfield (BF) TEM image to show dichotomy of Ta precipitates sizes present in the Cu-rich agglomerate, red circle shows precipitates ~10 nm in diameter while black circle shows precipitates ~5 nm in diameter. (c) HR TEM micrograph of Ta precipitates within the Cu-rich agglomerate with a semi-coherent interface and Nishiyama-Wassermann orientation relationship Cu <0$\bar{1}$1>// Ta <001> and Cu ($\bar{1}$11)//Ta ($\bar{1}$10) as confirmed by FFTs (inset). Difference in lattice parameters (Ta (BCC) a = 3.3 pm and Cu a =3.6 pm) is source of Moiré fringes. (d) Cartoon schematic of microstructure.

Increasing the deposition temperature to 600 °C significantly altered the microstructure morphology. The substantial difference between the mobilities of Cu and Ta at 600 °C led to self-assembly of Cu into Cu-rich agglomerates spaced tens of microns apart while the Ta remained in Ta-rich vein-like structure either surrounding the islands or comprising the film between the Cu-rich agglomerates. Fig. 3-4 portrays an overview of the film morphology along with HR TEM images for phase identification within the microstructure features. The self-assembly of Cu-Ta here is akin to that seen in Cu-Nb films which formed large spherulitic grains encompassed by an amorphous matrix [16]. As seen in Fig. 3-4 (a), the Cu-rich islands, ranging from 30 to 500 nm in diameter, are composed of FCC Cu homogeneously interspersed with fine Ta precipitates approximately 5 nm in diameter. Due to the relatively low mobility of Ta at 600 °C, the Ta adatoms landing within the Cu-rich agglomerates were able to diffuse small distances on the film surface before being trapped by the oncoming deposition layer. Fig. 3-4(c) provides a HR TEM image of a Ta precipitate ~5 nm in diameter inside of a Cu-rich agglomerate, the FFT of the circled region (inset) aligns with a BCC α-Ta structure. The presence of Ta clusters in the Cu-rich agglomerates is reminiscent of 90-10 at. % Cu-Ta alloys formed with equal channel angular extrusion which developed Ta nanoclusters and particles within a Cu matrix due to severe plastic deformation [17]. The interface between the Cu-rich agglomerates and the Ta-rich veins is clarified with HR TEM, Fig. 3-4 (b), that depicts semi-coherent boundary with a Nishiyama-Wassermann orientation relationship Cu $<0\bar{1}1>$// Ta <001> and Cu $(\bar{1}11)$//Ta $(\bar{1}10)$ which is just a 5.26 ° rotation from the Kurdjumov-Sachs orientation relationship present in the 400 °C film. Within the Ta-rich veins, the nanocrystals arranged in columns elongated in the growth direction persist. Again, planar defects are noted in these nanocrystals as was the case in the 400 °C film. A key feature is a homogeneous distribution of Cu nanocrystals present within

the Ta-rich veins. Similar to those identified from Fig. 4-3(b), the Cu nanocrystals are small clusters of Cu adatoms that were buried during deposition and were unable to diffuse substantial distances to reach the larger Cu agglomerates due to limited bulk diffusivity as will be discussed further in this publication. The presence of features at two different length scales classifies this microstructure as a hierarchical structure. The first is microscale Cu-agglomeration and Ta-rich veins, the second being nanoscale Ta precipitates in the Cu-rich agglomerations and Cu nanocrystals in the Ta-rich veins. In the cross-sectional micrographs, the Cu-agglomerates account for just 33% of the area fraction which differs from the 50-50 at.% Cu-Ta of the XRF results. This suggests that upwards of 17% of the Cu content in the thin film is present in nanocrystalline form within the Ta veins.

As seen in Fig. 3-5(a), the final 800 °C film had a similar microstructure as the 600 °C film with Cu-rich agglomerations enshrouded by Ta-rich veins and again having hierarchical microstructure features present on the micron and nanoscale. The key difference being the coarseness of microstructure features in both the Cu-rich and Ta-rich regions. The Ta-precipitates present in the Cu-rich agglomerates, Fig. 3-5(b), have a bimodal distribution with a first population of small Ta precipitates approximately 5 nm diameter; some interspersed randomly and others clustered along inhomogeneities such as dislocations within the Cu-rich islands. A second population of larger precipitates approximately 10 nm in diameter are heterogeneously distributed in the Cu-rich islands. Atomically resolved HR-STEM imaging and the associated FFT patterns of Fig. 3-5(c) depict both precipitate populations maintain a Nishiyama-Wassermann orientation relationship with the Cu-rich agglomerate, Cu $<0\bar{1}1>$// Ta $<001>$ and Cu $(\bar{1}11)$//Ta $(\bar{1}10)$ and a semi-coherent boundary. The Ta-rich veins again contain planar defects as well as trace quantities of Cu nanocrystals. The interface between the Ta-rich

veins and the Cu agglomerates has a semi-coherent boundary with the Nishiyama-Wassermann orientation relationship. FFTs show the prominence of α-Ta due to a phase change from β to α-Ta as suggested by the XRD results. Similar to the 600 °C film, there is a discrepancy in the Cu-rich area fraction being approximately 30.2% and the 50-50 at.% Cu-Ta confirmed via XRF. This suggests that approximately 19.8% of the Cu content in the thin film is embedded nanocrystals within the Ta veins.

The results of this experiment showed that Cu-Ta film morphology varied as a direct function of deposition temperature. As the deposition temperature increased, the film microstructure evolved from phase separated nanocrystals to a wavy structure with concentration modulations approximately along the film growth direction (denoted as vertical concentration modulation or VCM) to hierarchical structures of Cu-rich agglomerations surrounded by Ta-rich veins. In the 600 and 800 °C case, Ta precipitates were noted within the Cu-rich islands and Cu nanocrystals were present within the Ta-rich veins. The cross-sectional SEM images of Fig. 3-6 provide a macroscopic view of the film cross-sections. The Cu-Ta maintains a bicontinuous structure in the 400 °C film. While the 600 and 800 °C films both depict Cu-rich agglomerations, the agglomerates are spaced further apart separated by large sections of predominantly Ta-rich veins in the 600 °C film in contrast to the 800 °C film which maintains a closer spatial distribution of the agglomerates. This research utilized changes in deposition temperature to influence the kinetics of phase separation during deposition. Other important factors such as deposition rate, chamber pressure, inert gas pressure, and energy of the oncoming adatoms could all be varied and are worthy of future inspection as they may yield interesting microstructural results.

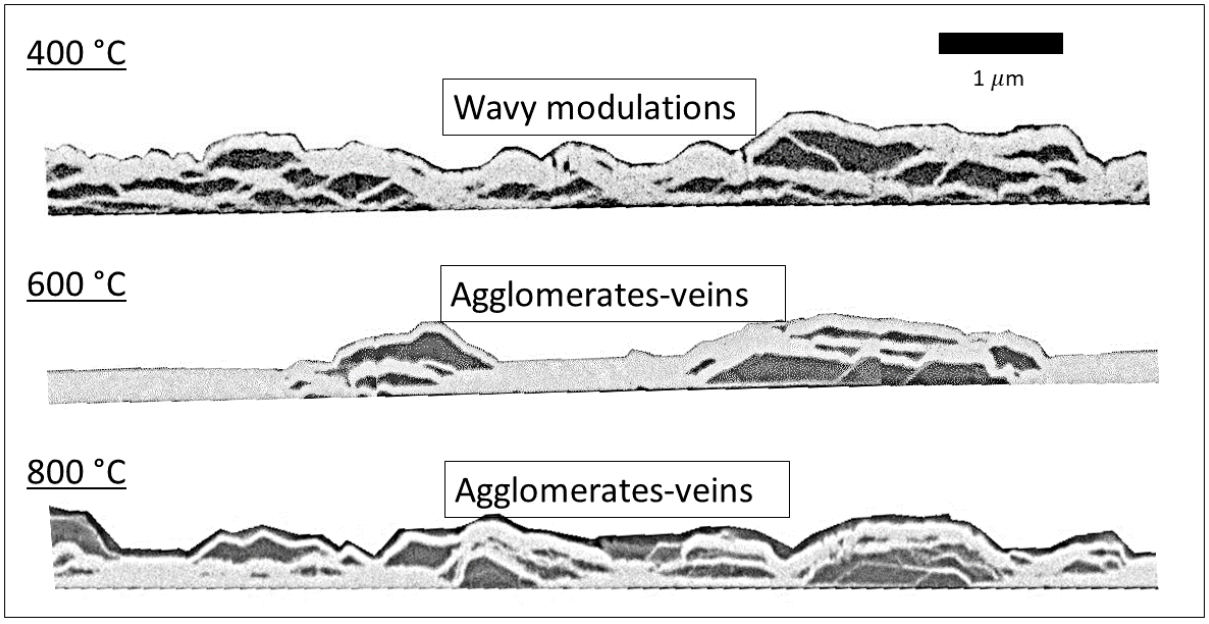

Figure 3-6: Backscattered electron (BSE) SEM images of 400, 600, 800 °C film cross sections. The white regions are Ta-rich and the dark regions are Cu-rich.

3.3 Discussion

3.3.1 Microstructural Analysis

The positive enthalpy of mixing, and differences in atomic size and crystal structure induced phase separation between Cu and Ta regions. The self-assembled phase separated microstructure of these co-deposited Cu-Ta heterogeneous thin films maintain moderate qualitative agreement with literature results. XRD results from PVD co-deposited Cu-Ta films by Muller *et al*. [5], depict x-ray amorphous as-deposited samples that crystallize into FCC-Cu and β-Ta after annealing at 600 and 800 °C. Nastasi *et al*. [18] annealed electron beam deposited 50-50 at. % Cu-Ta films and reported similar initially amorphous as-deposited samples. To the contrary, the 25 °C film in this experiment was nanocrystalline as evidenced by the broadened XRD crystalline peaks for Cu (111) and β-Ta (200), Fig. 3-1, and HR TEM and SADP of Fig. 3-

2. The presence of crystallinity, compared to its absence in the two literature cases, can be explained by the significantly lower deposition rate of the co-deposition which gives the adatoms sufficient time to diffuse and form nanocrystals before being arrested by the subsequent layer despite their relatively low kinetic energy. The kinetics and thermodynamics of PVD co-deposition will be further explained in this section.

The results of this experiment show a continuous evolution of film microstructure morphology as the deposition temperature increases from 400 to 800 °C. Literature Cu-Ta films depict an increase in crystalline character after annealing with larger Ta grains and Cu forming interwoven clusters throughout the sample [5,6]. In this work, the microstructures of the 400 to 800 °C films follow the same crystallization trend but differ greatly in morphology. The wavy, VCM structure of the 400 °C film is akin to that observed in co-deposited Cu-Mo [1] and sputtered Cu-W both at 400 °C [19]. The Cu-rich agglomerations surrounded by Ta-rich bands along with features on different length scales in the 600 and 800 °C films align with the hierarchical microstructures of Cu-Mo [9] which formed macroscale Cu-Mo modulations along with Cu-rich islands containing nanoscale Mo precipitates. The Mo precipitates were either the BCC or FCC crystal structure depending on the precipitate's size that influenced its susceptibility towards mismatch strain relative to the surrounding Cu FCC lattice. Thus, the Mo was either strained to form a coherent interface or formed a semi-coherent interface with a Kurdjumov-Sachs orientation relationship to the Cu. For the Ta precipitates within the 600 and 800 °C Cu-Ta films, the Ta maintained its BCC structure and Nishiyama-Wassermann orientation relationship with the surrounding FCC Cu-rich agglomerate.

With increased deposition temperature, the Cu and Ta grains coarsened along with a

phase transformation from β-Ta to α-Ta. XRD and HAADF of Fig. 3-1 and Figs. 3-4 and 3-5 confirm this transformation that is already a consistently observed phenomena [8].

3.3.2 Phase Separation Phenomena

Multiple competing internal forces influence the movement of species during deposition of a co-sputtered metallic thin film. The complex relationship of PVD kinetics and thermodynamics gives rise to metastable states and non-equilibrium microstructures in the resulting metallic films as noted in past literature cases [1, 5, 9, 20]. In this experiment, Cu and Ta adatoms landing on the substrate surface will diffuse with respect to chemical potential and stress gradients into phase separated regions due to immiscibility at the deposition temperatures. The adatoms will move a limited distance on the film surface before being buried by the oncoming deposition layer and could essentially be frozen into place, especially at relatively low homologous temperatures. as their bulk diffusivity is orders of magnitude lower than their surface diffusivity. For example, in the self-diffusion of Cu, the bulk diffusivity is $3.8\times10^{-6}\ \frac{m^2}{s}$ versus the surface diffusivity of $2.5\times10^{-4}\ \frac{m^2}{s}$ at 500 °C [21]. The effects of bulk diffusion on the resultant microstructure are minimal to an extent they can be ignored which is termed the “frozen bulk approximation” in literature for deposition at relatively low homologous temperatures [22]. Thus, the surface diffusion is the dominant kinetic process during thin film growth at low homologous temperatures, and is controlled by the deposition rate, which determines the time between consecutive oncoming layers, and by the deposition temperature which is directly proportional to diffusivity.

Prior research related the spacing of phase separated regions in PVD immiscible alloy systems to calculated surface diffusion distances [20,23]. While valid, surface diffusion distances

cannot fully explain the agglomeration and precipitate formation seen in Cu-Ta deposited at 600 and 800 °C. Instead, an empirical understanding of these features is best formed by evaluating the mobilities of the constituent species at the various deposition temperatures. Direct comparison of the mobility will provide perspective of how one element may move relative to the other. Work by Fukutani *et al*. [24] uses a mobility-dependent Cahn-Hilliard expression to describe an Al-Si thin film system that readily phase separates during growth via spinodal decomposition with the separation limited to the growth surface. The similarities between the Al-Si system and the present work allow for an adaptation of the mobility expression to examine the Cu-Ta microstructures. Mobility (M) is defined as:

$$M = \frac{D * c_0(1 - c_0)}{k_b T} \tag{3-1}$$

Where c_0 is the overall composition of one component, k_b is Boltzmann's constant, T is deposition temperature, and D is the diffusivity of the species which is in turn solved with the well-known expression (as mentioned in the Introduction) [2]:

$$D = D_0 \exp\left(\frac{-Q}{k_b T}\right) \tag{3-2}$$

With D_0 as a diffusivity coefficient and Q is the activation energy required for the movement of an atom to an available adjacent site. As surface diffusion is dominant, the surface diffusion values for D_0 and Q are selected for each species. The mobility is defined as a velocity of particles per unit of force and in the case of Cu-Ta film growth, the force is the phase separating driving force. The units are $\frac{\frac{\mathrm{cm}^2}{\mathrm{sec}}}{\mathrm{eV}}$.

From Eqn. 3-2, the mobility of the Cu and Ta adatoms plotted as a function of deposition temperature in Fig. 3-7 depicts a high mobility of Cu compared to the relatively immobile Ta at 25, 400, 600, and 800 °C. With such low mobility values, the Ta adatoms are essentially frozen

once they land on the surface. At 25 °C both Cu and Ta are immobile with limited diffusion which accounts for the ~5 nm diameter nanocrystalline structure of the relevant film. For the 400, 600, and 800 °C films, the highly mobile Cu adatoms perform the majority of the material diffusion for the phase separation during deposition. With moderately high mobility, the Cu moves to form the VCM-like structure of the 400 °C film. In the 600 and 800 °C films, the Cu has significantly elevated mobility which, paired with the low deposition rate of 1.52 Å/sec that provides ample time for surface diffusion before burial by the subsequent depositing layer, enabled Cu agglomeration. The Ta precipitates are formed by immobile Ta adatoms trapped within the Cu agglomerations. The Ta is capable of small-scale diffusion at elevated temperatures and thus clustered into precipitates before being enveloped by the Cu. While most Cu adatoms landing on the surface of Ta-rich veins moved to form the Cu-rich sections, some Cu adatoms were trapped and surrounded by the Ta to form the small Cu nanocrystals seen inside the columnar grains of the Ta-rich veins.

The mobility argument explains the difference between the Cu-Ta microstructures of this work and those of Muller *et al*. [5,6]. In Muller *et al*., the Cu-Ta is deposited at room temperature where both species have low mobilities. The samples were annealed to enable coarsening via bulk diffusion and formation of Cu-rich regions along with large Ta grains. In the present research, the co-deposition of Cu-Ta at elevated temperatures, where Cu is significantly more mobile than the higher melting point Ta, accentuates the disparity of the constituent element mobilities leading to the entrapment of Ta as precipitates within the Cu-rich regions and the Cu clusters within the Ta-rich veins.

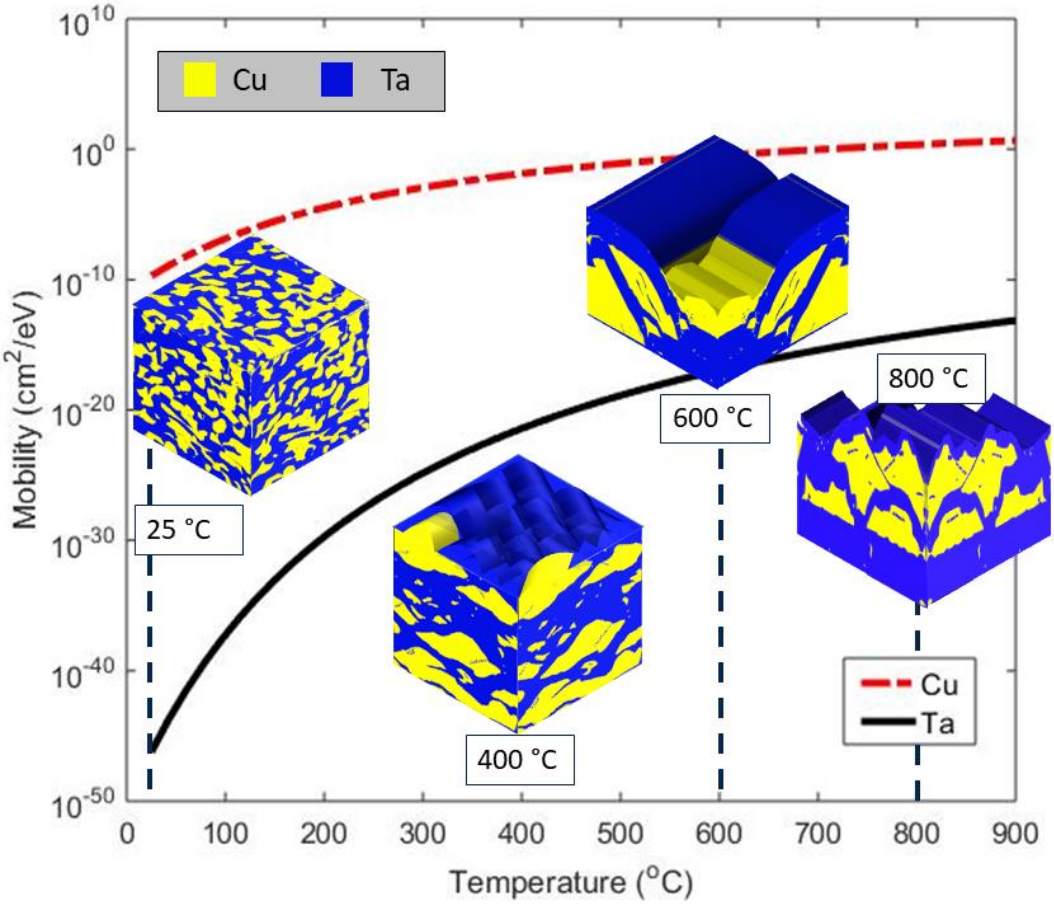

Figure 3-7: Mobility of the constituent Cu and Ta adatoms as a function of temperature during PVD. (Inset) Cartoon schematics of the film morphologies at the respective temperatures (constant deposition rate, 1.52 Å/sec for all).

3.3.3 Metastable States

It is worthwhile to discuss the driving force behind the stability of the metastable β-Ta and how β-Ta transitions to the equilibrium state α-Ta as a function of increasing deposition temperature. In the case of immiscible Cu-Nb systems, nanoscale phase separation reduces the free energy and incentivizes the metastable amorphous phase [25]. For Cu-Ta, β-Ta stability and later phase transition to α-Ta is best explained with the thermodynamic driving forces and the surface energy of the phases as they nucleate and grow during deposition. As seen in Fig. 3-5,

the Ta adatoms are not landing on a coherent crystal lattice but rather a series of nanocrystals or clusters with a variety of orientations. Therefore, the system can be represented as Ta crystals growing on an amorphous substrate. Classical nucleation theory can be used to express the nucleation rate as:

$$R \propto \exp\left(\frac{-E_1}{kT}\right) \exp\left(\frac{-W^*}{kT}\right) \tag{3-3}$$

Where the nucleation rate, R, is proportional to the exponential of the activation energy for adatoms to diffuse to the nuclei, E_1, Boltzmann's constant, k, temperature, T, and the nucleation barrier related to Gibbs free energy, W^*. The nucleation barrier is expressed as:

$$W^* = \frac{1}{3}\pi\left[\frac{(\Delta\gamma_{a-c}^{interface} + 2\Delta\gamma_{a-c}^{surface}}{(\Delta g_{a-c}^{Ta})}\right] \tag{3-4}$$

The $\Delta\gamma_{a-c}^{interface}$ is the change in interfacial energy and $\Delta\gamma_{a-c}^{surface}$ is the change in surface energy of the growing crystal nuclei on the amorphous substrate. The change in Gibbs free energy, Δg_{a-c}^{Ta}, acts as the driving force for chemical growth. The expression for the nucleation barrier and the W^* notation, is derived from the change in Gibbs free energy of formation at a critical nuclei radius, r^*.

Further details on the thermodynamic quantities, including the exact values of changes in Gibbs free energy and surface energies, are available in Colin *et al.* [11]. More importantly, the qualitative understanding is that the change in Gibbs free energy is larger for α-Ta than for β-Ta crystalline formation at room temperature. While this would normally prefer α-Ta nucleation rather than β-Ta, the surface energy provides a significant contribution to the overall free energy with $\Delta\gamma_{a-\alpha}^{surface} > \Delta\gamma_{a-\beta}^{surface}$. Factoring in the surface energy difference and change in Gibbs free energy into Eqn. 3-3 explains a preference for β-Ta nucleation and prevalence of β-Ta in the films deposited in this experiment up to 400 °C. Additionally, film growth residual stresses in

these low temperature films may induce the Ta crystallites to tetragonally distort into the β-Ta structure. Beyond 400 °C, the energy barrier for homogeneous nucleation of the β-Ta exceeds that of α-Ta, $W_{\beta}^{*} > W_{\alpha}^{*}$, leading to the preferred nucleation of α-Ta as seen from Eqn. 3-4. The change in preferred nucleation along with the phase transformation from β-Ta to α-Ta observed at 750 °C [13] both contribute to the decline of the β-Ta XRD peaks observed in both the 600 and 800 °C films. Future experimentation can determine if the phase transformation from β-Ta to α-Ta accounts for the planar defects omnipresent in the Ta-rich sections of the 400, 600, and 800 °C films or if the defects are chiefly the product of high internal film stress during deposition. On a final point, the phase separation of Cu and Ta will induce spatial heterogeneity in the interfacial energy term in the classical nucleation theory. In addition, strain energy in the film due to film growth residual stresses at low temperatures could contribute to a non-uniform Ta crystal structure. Both may have caused differences in preferred phase of Ta nucleation at different locations in the film within a constant deposition temperature.

3.4 Conclusions

The co-deposition of Cu-Ta at four temperatures yielded four unique microstructures that were previously unobserved in Cu-Ta systems. As the deposition temperature increased from 25 to 800 °C, the microstructure varied from nanocrystals to a wave-like vertical concentration modulated structure to Cu-rich agglomerations and Ta-rich veins with hierarchical features. The hierarchical structure, which describes having key features on two length scales, is particularly interesting in the 600 and 800 °C films. At the macroscale, the Cu and Ta organize into Cu-rich agglomerates and Ta-rich veins. At the nanoscale, examination of the Cu-rich agglomerates revealed a number of enclosed Ta precipitates while inspection of the Ta-rich veins showed small Cu nanocrystals entrapped within the Ta columnar grains. Prominent phase separation

occurred for all deposition temperatures and in the 400, 600, and 800 °C cases, semi-coherent grain boundaries were noted between the Cu-rich and Ta-rich regions. Two common orientation relationships, Nishiyama-Wasserman and Kurdjumov-Sachs were noted either between the Cu-rich agglomerations and Ta-rich veins or at the nanoscale with Ta precipitates enclosed in the Cu-rich clusters.

The various microstructures are the result of a large difference in constituent element mobility at the experimental film deposition temperatures. As the mobility of Cu is orders of magnitude higher than that of Ta, the resultant microstructures are chiefly the product of highly mobile Cu and relatively immobile Ta. Both species migrate via surface diffusion when depositing flux arrives on the substrate but is buried in the bulk after the next layer gets deposited, Cu may have limited bulk diffusivity whereas Ta will have negligible bulk diffusivity at the deposition temperatures used in these experiments. XRD and S/TEM micrographs have revealed equilibrium and metastable states of Cu and Ta: FCC Cu, α-Ta (BCC), β-Ta (tetragonal). Their presence is reasoned by changes in Gibbs free energy and interfacial energy which act as driving forces for phase organization. Future work will examine the mechanical performance of these microstructures which should yield interesting results due to the complex interfaces at a variety of length scales and the influence they will have on dislocation motion and plastic deformation.

References

[1] B. Derby, Y. Cui, J. Baldwin, R. Arróyave, J. Demkowicz, and A. Misra. Processing of novel pseudomorphic Cu – Mo hierarchies in thin films. *Materials Research Letters*. 7(1): 1-11, 2019.

[2] M. Ohring. *Materials Science of Thin Films*. Elsevier, 2001.

[3] K. Holloway, P. Fryer, C. Cabral, J.M.E. Harper, P.J. Bailer, K.H. Kelleher. Tantalum as a diffusion barrier between copper and silicon: failure mechanism and effect of nitrogen additions. *Journal of Applied Physics*. 71:5433, 1992.

[4] J. Avallone, T. Nizolek, T. Pollock, M. Begley. A model for high temperature deformation of nanolaminate Cu-Nb composites. *Materials Science Engineering A.* 761:138016, 2019.

[5] C. M. Muller, S. Parviainen, F. Djurabekova, K. Nordlund, R. Spolenak. The as-deposited structure of co-sputtered Cu-Ta alloys, studied by X-ray diffraction and molecular dynamics simulations. *Acta Materialia.* 82:51-63, 2015.

[6] C.M. Muller, A. Sologubenko, S. Gerstl, R. Spolenak. On spinodal decomposition in Cu-34 at.% Ta thin films – an atom probe tomography and transmission electron microscopy study. *Acta Materialia.* 89:181-192, 2015.

[7] K. W. Kwon, C. Ryu, R. Sinclair, S. S. Wong. Evidence of heteroepitaxial growth of copper on beta-tantalum. *Applied Physics Letters*. 71:3069, 1997.

[8] H. J. Lee, K.W. Kwon, C. Ryu, R. Sinclair: Thermal stability of a Cu/Ta multilayer: an intriguing interfacial reaction. *Acta Materialia*. 47**(**15):3965-3975, 1999.

[9] B. Derby, Y. Cui, J. K. Baldwin, and A. Misra. Effects of substrate temperature and deposition rate on the phase separated morphology of co-sputtered, Cu-Mo thin films. *Thin Solid Films*. 647:50–56, 2018.

[10] A. Jiang, T. A. Tyson, L. Axe, L. Gladczuk, M. Sosnowski, P. Cote. The structure and stability of beta-Ta thin films. *Thin Solid Films*. 479(1):166-173, 2005.

[11] J. J. Colin, G. Abadias, A. Michel, C. Jaouen. On the origin of the metastable beta-Ta phase stabilization in sputtered thin films. *Acta Materialia*. 126:481-493, 2017.

[12] M. Read, C. Altman. A new structure in tantalum thin films. *Applied Physics Letters*. 7:51 1965.

[13] A. Jiang, A. Yohannan, N. Nnolim, T.A. Tyson, L. Axe, S. Lee, P. Cote. Investigation of the structure of beta-Ta. *Thin Solid Films*. 437:116-122, 2003.

[14] S.L. Lee, M. Doxbeck, J. Mueller, M. Cipollo, P. Cote. Texture, structure, and phase transformation in sputter beta tantalum coating. *Surface Coating Technology*. 177:44-51 2004.

[15] J. Wang, X. Zhang. Twinning effects on strength and plasticity of metallic materials. *MRS Bulletin*. 41(4):274-281, 2016.

[16] A. Puthucode, A. Devaraj, S. Nag, S. Bose, P. Ayyub, M. J. Kaufman, R. Banerjee. Devitrification of nanoscale phase-separated amorphous thin films in the immiscible copper-niobium system. *Philosophical Magazine*. 94(15):1622-1641, 2014.

[17] M. Rajagopalan, K. Darling, S. Turnage, R.K. Koju, B. Hornbuckle, Y. Mishin, K.N. Solanki. Microstructural evolution in a nanocrystalline Cu-Ta alloy: a combined *in-situ* TEM and atomistic study. *Materials & Design*. 113:178-185, 2017.

[18] M. Natasi, F.W. Saris, L.S. Hung, J.W. Mayer. Stability of amorphous Cu/Ta and Cu/W alloys. *Journal of Applied Physics*. 58:3052-3058, 1985.

[19] F.T.N. Vullers, R. Spolenak. From solid solutions to fully phase separated interpenetrating networks in sputter deposited "immiscible" W-Cu thin films. *Acta Materialia*. 99:213-227, 2015.

[20] J. Xue, Y. Li, L. Hao, L. Gao, D. Qian, Z. Song, J. Chen. Investigation on the interfacial stability of multilayered Cu-W films at elevated deposition temperatures during co-sputtering. *Vacuum.* 166:162-169, 2019.

[21] H. Mehrer. *Diffusion in solid metals and alloys*. Springer-Verlag, 1990.

[22] C.D. Adams, M. Atzmon, Y.T. Cheng, D.J. Srolovitz. Phase separation during co-deposition of Al-Ge thin films. *Journal of Materials Research*. 7(3):653-666, 1991.

[23] M. Powers, B. Derby, E. Raeker, N. Champion, A. Misra. Hillock formation in co-deposited thin films of immiscible metal alloy systems. *Thin Solid Films*. 693:137692, 2020.

[24] K. Fukutani, K. Tanji, T. Saito, T. Den. Fabrication of well-aligned Al nanowire array embedded in Si matrix using limited spinodal decomposition. *Japanese Journal of Applied Physics*. 47(2):1140-1146, 2008.

[25] R. Banerjee, A. Puthcode, S. Bose, P. Ayyub. Nanoscale phase separation in amorphous immiscible copper-niobium alloy thin films. *Applied Physics Letters*. 90:021904, 2007.

Chapter 4

Hillock Formation in Co-Deposited Thin Films of Immiscible Metal Alloys

4.1 Introduction

The formation of protruding grains, or hillocks, on the surface of metal thin films has been noted in research for many decades [1]. These hillocks have been thoroughly studied in monolithic films comprised of Sn, Pb, or Al [2,3], and are typically linked to internal residual stresses within the films. It is worthwhile to study the presence of these hillocks and how they may arise during the co-deposition of immiscible alloys since they can have significant, often detrimental, effects on a film's mechanical performance. High temperature depositions paired with a substantial difference in thermal expansion coefficients of the film and substrate result in these internal stresses. During deposition, the metallic thin film will experience higher expansion but is confined by the more rigid substrate material leading to compressive internal stresses. Upon cooling, the film contracts and experiences tensile internal stress [4]. The resulting stress gradients cannot be fully relaxed by diffusional creep over the timescale of film deposition. Localized differential relaxation will generate a difference in the chemical potential of vacancies in the stressed and unstressed regions. This chemical potential gradient acts as a driving force for long range mass transport of atoms as they diffuse from the surrounding volume to isolated regions in the film. The resulting plastic relaxation will form strain-free extrusions, or hillocks

[1,4]. The formation of these hillocks is chiefly influenced by the magnitude of the stress gradients, the film thickness, and the substrate-film interfacial energy.

Recent studies have revealed hillock formation in mutually soluble binary alloy metallic thin films such as Sn-Cu [3], Pt-Ti [5], and Au-Pd [6]. However, there are limited publications that discuss the presence of hillock features in phase-separated films of immiscible alloys. Additionally, it is worthwhile to examine whether hillock formation is caused by a variety of forces rather than solely stress gradients. To examine the contribution a phase separation driving force has on surface morphology features, we again select the binary Cu-Ta system. With the Cu-Ta being immiscible, the components will phase separate to pure Cu and Ta regions with atomically resolved interfaces due to a large heat of mixing, even at fairly high processing temperatures [7]. The potential convolution of phase separation and hillock formation may also be present in tertiary immiscible metal alloys, such as Cu-Mo-Ag.

With PVD, immiscible metals can be co-deposited at various temperatures and deposition rates to provide insight on the forces for phase separation and the kinetics during film growth [8]. In the case of Cu-Ta, co-sputtered Cu and Ta adatoms will contact the substrate surface and diffuse according to phase separation with a temperature-dependent mobility before being buried by the subsequent deposition layer. The ratio of the deposition temperature to the melting temperature of an element, known as the homologous temperature, T_H, will directly influence the mobility of a species. At increasing deposition temperatures, the lower Cu melting temperature yields a greater T_H value and a more mobile Cu species compared to Ta [9]. The difference in diffusion lengths of Cu-Ta adatoms will influence the resultant microstructure morphologies as seen in Cu-Mo systems [10, 11]. In the case of Cu-Mo, there was a direct correlation between deposition temperature and morphology as the Cu-Mo moved from vertical to lateral to random

concentration modulations with increasing temperature and thus increasing diffusion length of Cu and Ta. In the Cu-Ta system, the more mobile Cu can form Cu-rich agglomerations which can affect the surface features of the film. The disparity in constituent element mobility is also noted for Cu-Mo-Ag in which the Cu and Ag atoms have much higher T_H values than Mo at a given deposition temperature.

This work will use co-sputtering to grow thin films of Cu-Ta and of Cu-Mo-Ag at various deposition temperatures to examine different T_H values and elemental diffusion lengths. The resultant film microstructures and surface morphologies will verify any connection between hillock formation and phase separation within systems of highly disparate constituent elemental mobilities during processing. The comparison of binary and tertiary alloys will measure the effect of having single versus multiple highly mobile species during deposition.

4.1.1 Experimental Methods

All Cu-Ta films were co-deposited via direct current magnetron sputtering at a composition of 50-50 at. % Cu-Ta onto Si-SiO_2 substrates with millimeter thickness. The top 50 nm of the substrate, contacting the film surface, is SiO_2 while the remainder is Si. The 50 at. % was selected to emphasize bicontinuous structure morphology rather than minority phase segregation. The Cu-Mo-Ag films were deposited onto Si-SiO_2 substrates with millimeter thickness and target compositions of 40-30-30 at. % Cu-Mo-Ag. The deposition chamber was a Kurt Lesker PVD 75 with 2'' disk Cu, Ta, Mo, and Ag targets with purities of 99.999% for Cu, 99.99% for Ag, and 99.95% for Mo and Ta. The base pressure utilized was less than 6 x 10^{-7} Pa, with a target throw distance of 5 inches. Cu-Ta films were deposited at a combined rate of 1.5 Angstroms/sec to 700 nm thickness at four temperatures: 25, 400, 600, and 800 °C. Cu-Mo-Ag films were deposited at a combined rate of 20 Angstroms/sec to 300 nm thickness at three

temperatures: 400, 600, and 800 °C. All the films were deposited then left to cool to room temperature in the deposition chamber to prevent oxide formation on the film surface. The deposition rates were confirmed using film thickness measurements taken during sample preparation. The Cu-Ta films were deposited with 40 W DC power to the Cu target and 60 W DC power to the Ta target. The Cu-Mo-Ag films were deposited with DC power, 40 W to the Cu, 60 W to the Mo, and 40 W to the Ag targets. A substrate bias of 20 W was applied to each film and the substrates were rotated at 10 rpm during deposition. The bulk composition of the alloy films was measured via x-ray fluorescence spectroscopy using a Rigaku Supermini200. The surface morphology of the films was imaged using scanning electron microscopy (SEM), Tescan MIRA3 FEG SEM, operated at 30 keV and 2.4 nA for surface imaging and 20 keV for energy dispersive spectroscopy (EDS) for local surface composition mapping. Cross-sectional samples of the film were prepared with focused ion beam milling to generate foils that were lifted out and attached to Mo grids. The foils were further milled to ~150 nm thickness for transmission electron microscope (TEM) imaging. A scanning transmission electron microscope, JEOL 2100F STEM, operated at 200 keV was utilized for high resolution characterization of the cross-sectional samples.

4.2 Experimental Observations: Factors Inducing Hillock Formation in Cu-Ta and Cu-Mo-Ag

The SEM images of the Cu-Ta films, Fig. 4-1 (a-d), show the hillock formation was prominent only in the films deposited at 600 and 800 °C. The film deposited at 25 °C is predominantly flat. The 400 °C film had mild surface roughness with a limited number of hemispherical hillocks confined to a few select regions. The number of hillocks was too few to accurately determine any size or spatial distributions. For the 600 and 800 °C films, there was a

homogeneous distribution of faceted hillocks over the film surfaces. The 800 °C film had larger hillocks and reduced inter-hillock spacing compared to the 600 °C film. The EDS maps, Fig. 4-1(e-h), of all samples depict the majority of the film surface to be Ta with various regions of Cu present on top of the hillock facets. The distribution of the elements in the EDS maps suggest phase separation at the surface.

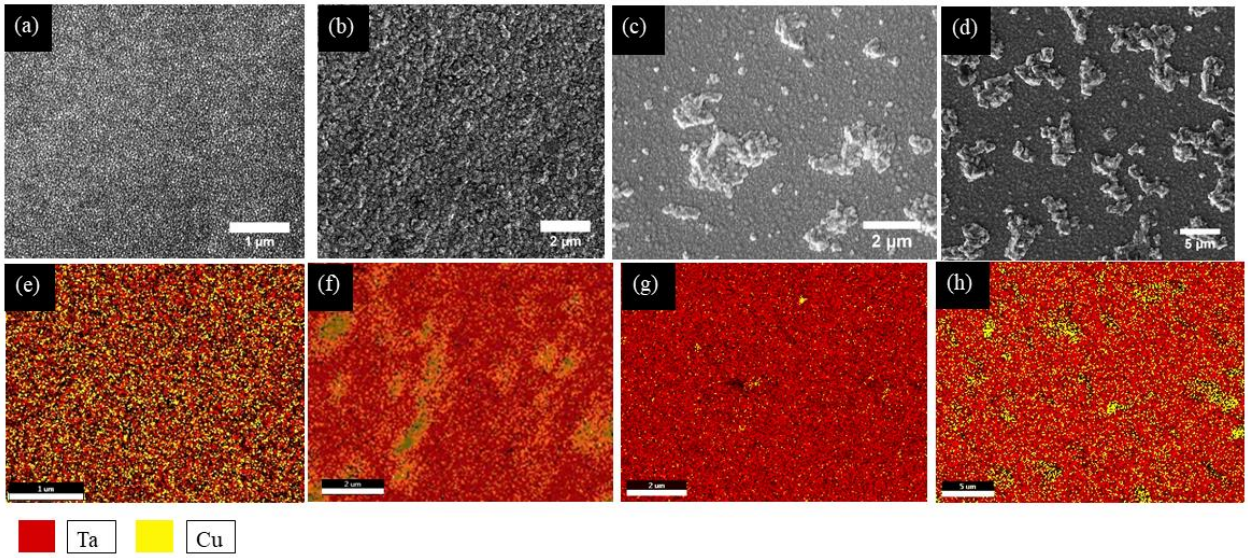

Figure 4-1: Secondary electron (SE) SEM (top row) images for the surfaces of Cu-Ta films deposited at (a) 25, (b) 400, (c) 600, and (d) 800 °C. Corresponding EDS images (bottom row) are (e) 25, (f) 400, (g) 600, and (h) 800 °C. The 25 °C sample reveals a flat, smooth surface while the 400 °C sample emphasizes one specific hillock in an otherwise flat film surface. SEM images of the 600 and 800 °C films reflect the homogeneous distribution of hillocks across the entire film. EDS mapping reveals noticeable concentrations of Cu on the hillock facets, while Ta is omnipresent on the film surface.

STEM HAADF and TEM imaging of the Cu-Ta film cross-sections, Fig. 4-2 (a-d), revealed strong phase separation within the film bulk. The film deposited at 25 °C depicted phase-separated polycrystalline Cu-Ta nanograins with grain diameters under ten nanometers. The 400 °C film contained layered Cu bands within a Cu-Ta nanocrystalline matrix. The Cu bands were oriented parallel to the film-substrate interface. Both the 25 °C and 400 °C films had

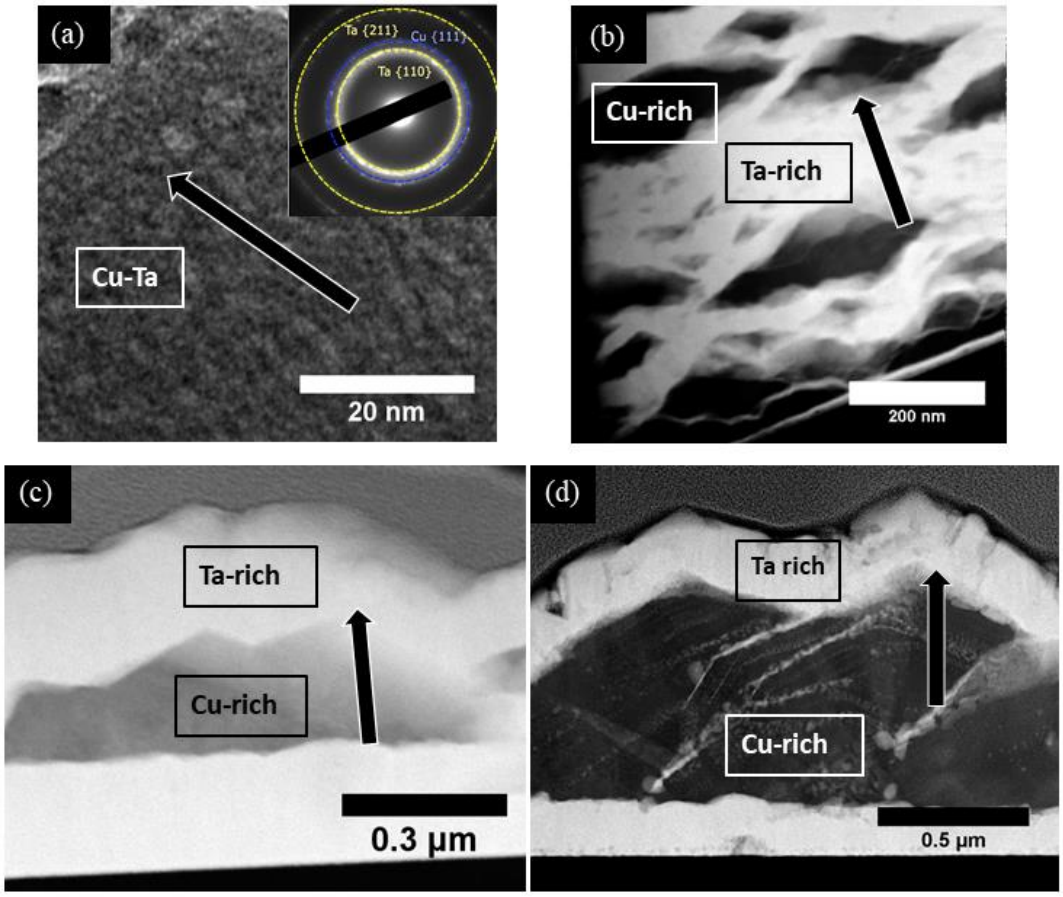

Figure 4-2: (a) TEM cross-sectional image of the Cu-Ta film deposited at 25 °C. STEM HAADF cross-sectional images of the Cu-Ta film deposited at (b) 400, (c) 600, and (d) 800 °C. The arrow in the images denotes film growth direction. For the 25 °C deposition, the entire film is nanocrystalline Cu-Ta as evidenced by the small contrasting grains and confirmed by selective area diffraction pattern (inset) suggesting polycrystalline presence. In the remainder of the films, the darker contrast suggests Cu-rich regions while lighter contrast suggests Ta-rich regions. The light veins in (d) indicate Ta precipitates in the Cu-rich regions. The cross-sectional images confirm there are no voids or cavitation within the hillocks.

a consistent film thickness of 700 nm. The 600 °C film had a dichotomy of film regions: hillock regions that were 800 nm thick and "matrix" regions located between hillocks that were 500 nm thick. The "matrix" regions were predominantly Ta with trace amounts of Cu. The hillocks consisted of sizable Cu-rich agglomerations within a Cu-Ta nanocrystalline matrix. The 800 °C film shows a similar "matrix"- hillock distribution, but with an increased hillock height of

approximately 900 nm. The 800 °C hillocks had larger Cu-rich agglomerations while the "matrix" regions maintained their majority Ta composition.

The SEM images of the Cu-Mo-Ag, Fig. 4-3 (a-c), display hillock formation only for the 600 and 800 °C films. The 400 °C film surface was generally flat and smooth. Both the 600 and 800 °C films contained a high density of hillocks evenly distributed throughout the surface with similar hillock morphology as Cu-Ta. The 600 °C film had faceted protruding grains while the 800 °C film had hemispherical hillocks with equivalent inter-hillock spacing. Both films had smaller average hillock sizes than the Cu-Ta films deposited at equivalent temperatures.

HAADF images of the Cu-Mo-Ag cross-sections, Fig. 4-4 (a-c), depict three distinct microstructure morphologies at the three deposition temperatures. The 400 °C film has nanoscale phase-separated Cu, Mo, and Ag grains. The 600 °C film contains large Cu agglomerations underneath the hillocks surrounded by nanoscale Mo-Ag modulations. As previously mentioned, modulations are morphologies of alternating compositions oriented in the lateral, vertical, or random directions. The Mo-Ag modulations in the 600 °C film are laterally oriented, meaning perpendicular to growth direction. Within the modulations, specific regions of Ag clustered into small-scale agglomerates. The modulations are typical for thin films grown under these conditions as discussed in the Anders' structure zone diagram [12]. The 800 °C film has larger Cu agglomerations capped by the nanoscale randomly oriented Mo-Ag modulations. Within the modulation regions of Fig. 4-4(c), some Ag regions have clustered into small-scale agglomerates that are slightly larger than those present in the 600 °C film modulations. EDS mapping from Fig. 4-4 reveals that trace amounts of all elements appear throughout the 600 and 800 °C films, e.g. small clusters of Cu in the Ag-Mo modulations and small amounts of Ag and Mo within the Cu-rich regions.

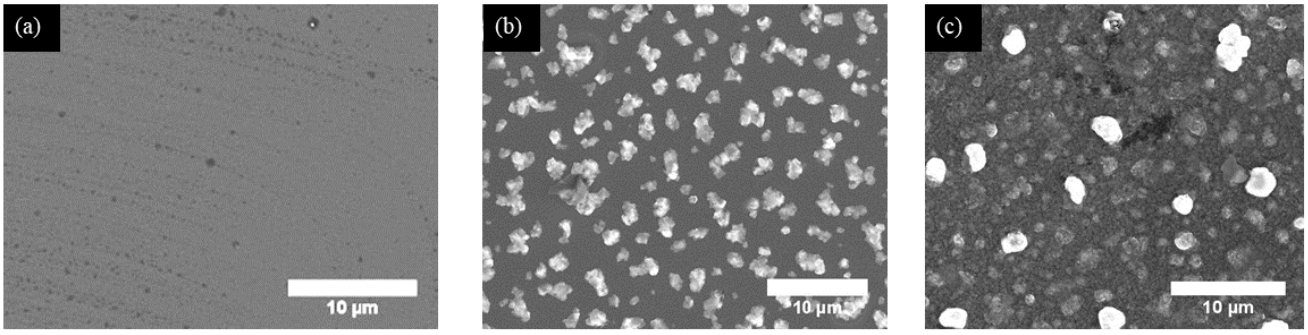

Figure 4-3: SE SEM images of Cu-Mo-Ag films deposited at (a) 400, (b) 600, and (c) 800 °C. Hillocks are only noticeable in the 600 and 800 °C films. The hillocks in both films are approximately the same size and have the same spatial distribution.

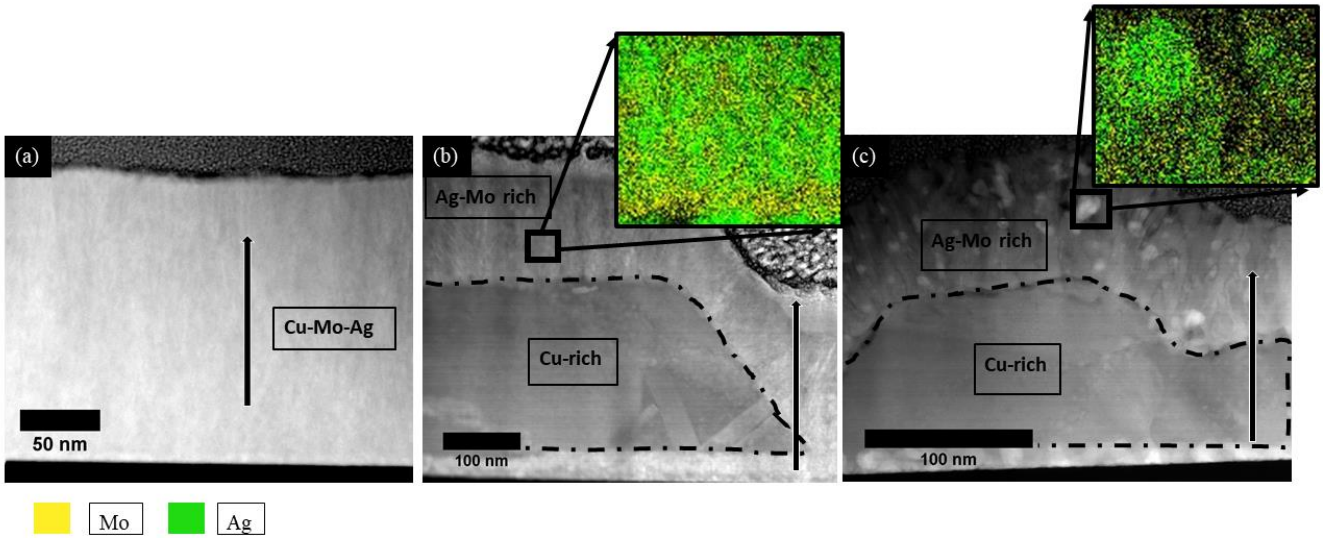

Figure 4-4: STEM HAADF cross-sectional images of the Cu-Mo-Ag films deposited at (a) 400, (b) 600, and (c) 800 °C. The arrows refer to the growth direction of the film. The 400 °C film is homogeneously Cu-Mo-Ag nanocrystals. In the 600 and 800 °C films, there is a Cu-rich core with a shell (hillock) consisting of Ag-Mo modulations as revealed by the inset EDS maps.

As previously discussed, [1,3] hillocks arise in monolithic films due to stress gradients in the film caused by the difference in substrate and film thermal expansion coefficients. This is especially true for Sn, Pb, and Ni films with relatively high coefficient of thermal expansion (CTE): 20, 29, and 13 $\times 10^{-6} m/(m\,K)$ respectively [13], compared to the CTE of Si, 2.6

$\times 10^{-6} m/(m\,K)$.

The immiscible Cu-Ta and Cu-Mo-Ag films contain significant volume fractions of BCC refractory metals with CTE's that are better matched with Si, e.g., $6.5 \times 10^{-6} m/(m\,K)$ for Ta and $5 \times 10^{-6} m/(m\,K)$ for Mo, and so the values of residual stresses due to CTE mismatch will be reduced. This can be further established by estimating the compressive stress present in the films. Using the simplified formula for biaxial stress based on CTE-mismatch induced strain, as detailed in [14], and a rule-of-mixtures based on film composition to select the modulus values, the calculated stress in the Cu-Ta film will reach 0.06 GPa at the 800 °C deposition. For the Cu-Mo-Ag film, the CTE-induced stress reaches 0.09 GPa at the 800 °C deposition. The biaxial stress values are lower with the corresponding lower deposition temperatures. The nanocrystalline Cu-BCC immiscible films exhibit ultra-high yield strengths, typically in excess of 2 GPa [15,16]. This makes the CTE mismatch induced residual stresses in Cu-Ta and Cu-Mo-Ag significantly lower than the yield strength.

The films also undergo an extended cooling period inside the chamber. The long cooling period prevents the formation of oxides on the film surface and eliminates oxides as a potential variable for hillock growth. It is worthwhile to note that the estimated residual compressive stress in the 400 °C film is comparable to those in the 600 and 800 °C films but the 400 °C film surface is flat, save for a small minority of regions. This indicates an additional mechanism beyond residual stress may be required to induce hillock growth. Thus, it is possible to conclude two things: first, the hillock formation mechanism may be different from the case of monolithic films of soft, low melting points metals such as Sn and Pb, second, hillock formation in the Cu-Ta and Cu-Mo-Ag films has been influenced by but cannot be wholly attributed to compressive residual stresses. The second statement can be further vindicated by considering the case of co-

deposited Cu-Mo thin films in [10,11] In those experiments, the Cu-Mo sputtered films were deposited at high deposition rates and equivalent temperatures to those in the current experiment. Meaning that the residual stresses present in the Cu-Mo were approximately the same as those seen in the Cu-Ta and Cu-Mo-Ag at equivalent deposition temperatures. However, the Cu-Mo does not form hillocks and has a relatively flat surface, suggesting an additional factor is required for hillock formation.

The additional impetus for hillock formation can be ascribed to the high difference in mobility of the constituent elements and the phase separation driving force of the immiscible alloy system. The mobility of the species during deposition can be viewed experimentally by noting the diffusion length of the arriving adatoms. The average diffusion distance at the surface of the film can be described with the expression, Eqn. 4-1 [17]:

$$X = \sqrt{2\,\nu\frac{a}{r}} * a * \exp\left(-\frac{Q_s}{2kT}\right) \tag{4-1}$$

Where X is the average diffusion distance, ν is the vibrational frequency of surface atoms ($\sim 10^{13}/s$) [17], k is Boltzmann constant ($1.38 \times 10^{-23} J/K$), a is individual jump distance which depends on interplanar spacing, r is deposition rate, T is deposition temperature, and Q_s is average activation energy for surface diffusion. This relationship emphasizes the sensitivity of the diffusion distance to temperature and deposition rate during processing.

Fig. 4-5 shows the average diffusion distance of the sputtered Cu-Ta and Cu-Mo-Ag elements evaluated by Eqn. 4-1, using Cu (111), Ta(110), Ag(111), Mo(110) interplanar spacing values along with tabulated surface diffusion activation energy values [18]. The calculated diffusion distances align with the microstructural morphologies found in Figs. 4-2 and 4-4. At lower deposition temperatures, the landing species have reduced mobilities and will diffuse short

distances before being buried by the oncoming deposition layer, which correlates to the nanocrystalline structures at 25 °C for Cu-Ta and 400 °C for Cu-Mo-Ag. At 600 and 800 °C, the more mobile Cu and Ag can diffuse hundreds of nm while the larger Ta and Mo will only diffuse tens of nm. This correlates to the large Cu aggregations forming the core of the hillocks covered by large regions of Mo-Ag modulations or Cu-Ta nanocrystalline matrices. The spacing between hillocks is on the order of 100's of nm and is proportional to Cu diffusion distance at 600 and 800 °C.

The disparate mobilities of the immiscible systems pairs with the phase separation driving force to produce the microstructure morphologies and surface features seen for the thin films of this experiment. In the case of Cu-Ta, the co-deposited species land on the substrate and will phase separate due to their high enthalpy of mixing. For the room temperature deposition, this led to the nanocrystalline Cu-Ta structure. However, a nanocrystalline structure has significant FCC-BCC interfacial energy. Therefore, at elevated deposition temperatures, the landing species will agglomerate to reduce the FCC-BCC interfacial energy of the system. The extent of the agglomeration is dictated by the temperature-dependent surface diffusion length as shown in Fig. 4-5. The initiation of this agglomeration is seen in the Cu-rich ribbons tens of nanometers apart in the 400 °C film. At the higher deposition temperatures of 600 and 800 °C, this agglomeration is more pronounced as the highly mobile Cu adatoms land on the surface and diffuse to Cu-rich regions. The low-mobility Ta diffuses small distances across the surface before being fixed by the incoming layer. While this explains the observed microstructure morphologies, further research is necessary to determine the exact mechanism of hillock growth and the specific contributions of residual stress and phase separation driving forces.

In a separate experiment with multilayered Cu-Mo systems [19], thermally induced

residual stress caused Cu protrusion towards the surface and hillock formation. The case of Cu-Ta suggests a different growth mechanism for hillocks as Cu agglomerates do not protrude upward and instead are present in isolated regions at the bottom, middle and surface of the metallic thin films. Again, further research is needed to clarify the hillock growth mechanism for Cu-Ta.

The hillock formation becomes even more complex in the case of the tertiary Cu-Mo-Ag. All three species have reduced mobilities during the 400 °C deposition, which result in nanoscale Cu, Mo, and Ag grains. The Cu and Ag become highly mobile during the 600 and 800 °C depositions and tend to agglomerate within the film. The Cu undergoes a large-scale agglomeration while the Ag forms smaller clusters within the Ag-Mo modulations as seen in Fig. 4-4 (b,c). The reasoning for the different Ag and Cu clustering tendencies may be related to different FCC-BCC interfacial energies. The Mo has relatively low mobility at all the experimental deposition temperatures and thus diffuses short distances before being trapped by the oncoming layer. Present research allows only speculation on the hillock growth mechanism of this complex tertiary system. Future research must consider the internal stress, phase separation, and interfacial energies to establish any sort of definitive hillock growth process.

As depicted in Figs. 4-1 and 4-4, the driving force for phase separation is prominent in both systems. This behavior has been present, to an extent, in the similar Cu-W immiscible alloy system [20]. Co-deposited Cu-W exhibits spherical surface protrusions on films deposited at 400 °C. However, the hillocks in Cu-Ta and Cu-Mo-Ag are significantly larger and more faceted than the Cu-W surface features. All three cases present a delicate interplay between film stresses and phase separation in co-deposited FCC-BCC immiscible metal films that gives rise to the hillock phenomena.

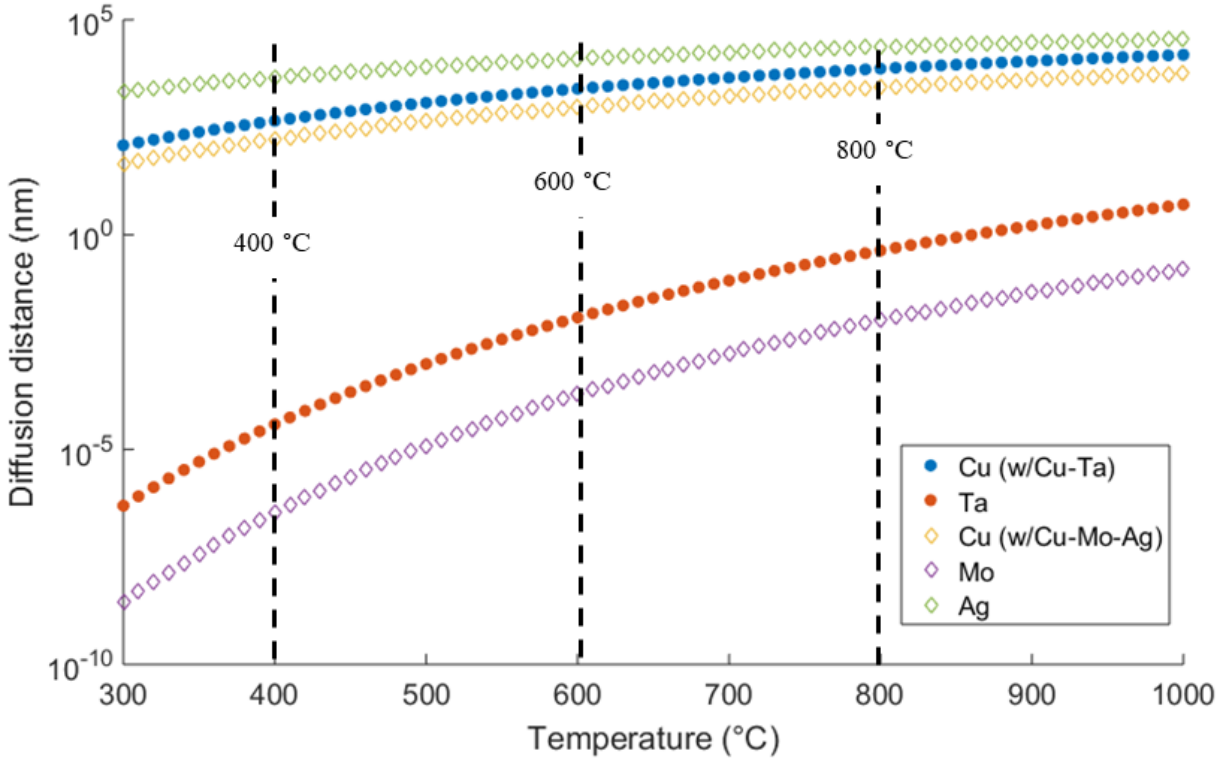

Figure 4-5: Calculated surface diffusion distance of elemental adatoms as a function of temperature.

4.3 Conclusions

Hillock formation that is typically affiliated with high temperature depositions of monolithic films has been observed for immiscible metal alloy films. Hillocks were present in the Cu-Ta and Cu-Mo-Ag films deposited at 600 and 800 °C, but not in films deposited at 25 and 400 °C. The thermally induced stress gradients that cause hillock formation in monolithic films are less significant in phase-separated films containing BCC refractory metals, requiring an additional factor to fully explain the hillock presence. The contribution of the phase separating driving force paired with the contrasting temperature-dependent mobilities of the constituent elements is considered. Average diffusional distance travelled by the deposited adatoms is an

analog for elemental mobility. The Cu and Ag have significantly higher diffusional distance compared to Mo and Ta, leading to agglomerations of Cu and Ag as evidenced in the HAADF cross-sectional images of the films. The microstructure morphologies and spacings align with the calculated diffusional distances, validating the proposed surface diffusion model. Thus, phase separation and disparate element mobility supplement internal stress driving forces to cause hillock formation in co-deposited immiscible Cu-Ta and Cu-Mo-Ag alloys.

References

[1] P. Chaudhari. Hillock growth in thin films. *Journal of Applied Physics*. 45:4339, 1974.

[2] S. Hwang, Y. Lee, Y. Park, J. Lee, C. Jeong, Y. Joo. *In situ* study of stress relaxation mechanisms of pure Al thin films during isothermal annealing. *Scripta Materialia*. 54:1841-1846, 2006.

[3] W. Boettinger, C. Johnson, L. Bendersky, K. Moon, M. Williams, G. Stafford. Whisker and Hillock formation on Sn, Sn-Cu, and Sn-Pb electrodeposits. *Acta Materialia*. 53:5033-5050, 2005.

[4] M. Jackson, C. Li. Stress relaxation and hillock growth in thin films. *Acta Metallurgica*. 30:1993-2000, 1982.

[5] H. Nam, D. Choi, W. Lee. Formation of hillocks in Pt/Ti electrodes and their effects on short phenomena of PZT films deposited by reactive sputtering. *Thin Solid Films*. 371:264-271, 2000.

[6] S. Nazarpour, O. Jambois, C. Zamani, F. Afshar, A. Cirera. Stress distribution and hillock formation in Au/Pd thin films as a function of aging treatment in capacitor applications. *Applied Surface Science*. 255:8995-8999, 2009.

[7] M. Nastasi, F. Saris, L. Hung, J. Mayer. Stability of amorphous Cu/Ta and Cu/W alloys. *Journal of Applied Physics*. 58:3052-3058, 1985.

[8] J. Thornton. Influence of apparatus geometry and deposition conditions on the structure and topography of thick sputtered coatings. *Journal of Vacuum Science and Technology*. 11:666-670, 1974.

[9] T. Frolov, K. Darling, L. Kecskes, Y. Mishin. Stabilization and strengthening of nanocrystalline copper by alloying with tantalum. *Acta Materialia*. 60:2158-2168, 2012.

[10] B. Derby, Y. Cui, J.K. Baldwin, A. Misra. Effects of substrate temperature and deposition rate on the phase separated morphology of co-sputtered Cu-Mo thin films. *Thin Solid Films*. 647:50-56, 2018.

[11] B. Derby, Y. Cui, J.K. Baldwin, R. Arroyave, M. Demkowicz, A. Misra. Processing of novel pseudomorphic Cu-Mo hierarchies in thin films. *Materials Research Letters*. 7(1):1-11, 2019.

[12] A. Anders. A structure zone diagram including plasma based deposition and ion etching. *Thin Solid Films*. 518(15):4087-4090, 2010.

[13] F. Cverna (Ed.). *ASM Ready Reference: Thermal Properties of Metals, ASM Materials Data Series*. ASM International, 2002.

[14] A. Segmuller, M. Murakami. X-ray diffraction analysis of strains and stresses in thin films. *Treatise on Materials Science & Technology*. 27:143-200, 1988.

[15] Y. Cui, B. Derby, N. Li, A. Misra. Design of bicontinuous metallic nanocomposites for high-strength and plasticity. *Materials & Design*. 166:107602, 2019.

[16] Y. Cui, B. Derby, N. Li, N.A. Mara, A. Misra. Suppression of shear banding in high-strength Cu/Mo nanocomposites with hierarchical bicontinuous intertwined structures. *Materials Research Letters*. 6(3):184-190, 2018.

[17] M. Ohring. *Materials Science of Thin Films*. Elsevier, 2001.

[18] H.P. Bonzel. *Surface Diffusion on Metal*. Springer-Verlag, 1990.

[19] S. Luby, E. Majkova, M. Jergel, M. Brunel, G. Leggieri, A. Luches, G. Majni, P. Mengucci. Stability of interfaces in Mo/Cu multilayered metallization. *Thin Solid Films*. 277:138-143, 1996.

[20] J. Xue, Y. Li, L. Hao, L. Gao, D. Qian, Z. Song, J. Chen. Investigation on the interfacial stability of multilayered Cu-W films at elevated deposition temperatures during co-sputtering. *Vacuum*. 166:162-169, 2019.

Chapter 5

Hierarchical Morphologies in Co-Sputter Deposited Thin Films

5.1 Introduction

A hierarchical microstructure has distinct phases and morphologies at multiple length scales, differing from a bimodal structure in which the same characteristic (e.g. equiaxed grains of the same phase) is emulated across two length scales [1]. With their complex multilength-scale structures that may include non-equilibrium states, hierarchical architectures have a wide range of applications in electrochemical processes [2] and as functional materials [3]. Recent work has shown these hierarchical morphologies may self-assemble during the magnetron co-sputtering of immiscible metallic alloy films [4-8]. There is extensive evidence that heterogeneous films may exhibit advantageous physical properties such as high strength and corrosion resistance [4], suppression of shear banding [5], enhanced strength and fracture toughness [6], and prominent radiation tolerance [7]. However, there is limited fundamental understanding as to the formation mechanisms of hierarchical features in immiscible alloy thin films due to self-organization during deposition.

It is well understood that immiscible elements co-deposited using physical vapor deposition (PVD) will self-organize into phase separated regions with chemically sharp interfaces [8]. The self-organization and mutual immiscibility may stem from a positive enthalpy of mixing, an equilibrium phase difference, e.g. FCC for one element and BCC for the other,

disparate lattice parameters, or a combination of the three. Previous work has emphasized homogeneous microstructure formation within immiscible alloy films, where homogeneous refers to a constant concentration modulation wavelength and morphology throughout the sample. Systems such as Cu-W [9,10], Cu-Ta [11,12], and Cu-Mo [13], have yielded concentration modulation structures whose specific orientations can be controlled by varying the PVD processing parameters. The monomodal co-deposited microstructures are categorized into three quintessential morphologies: vertical concentration modulation (VCM), lateral concentration modulation (LCM), and random concentration modulation (RCM) structures. To assist with the visualization of the two microstructures, Fig. 5-1 provides cartoons of a generic monomodal structure, Fig. 5-1a, and a generic multimodal hierarchical structure, Fig. 5-1b.

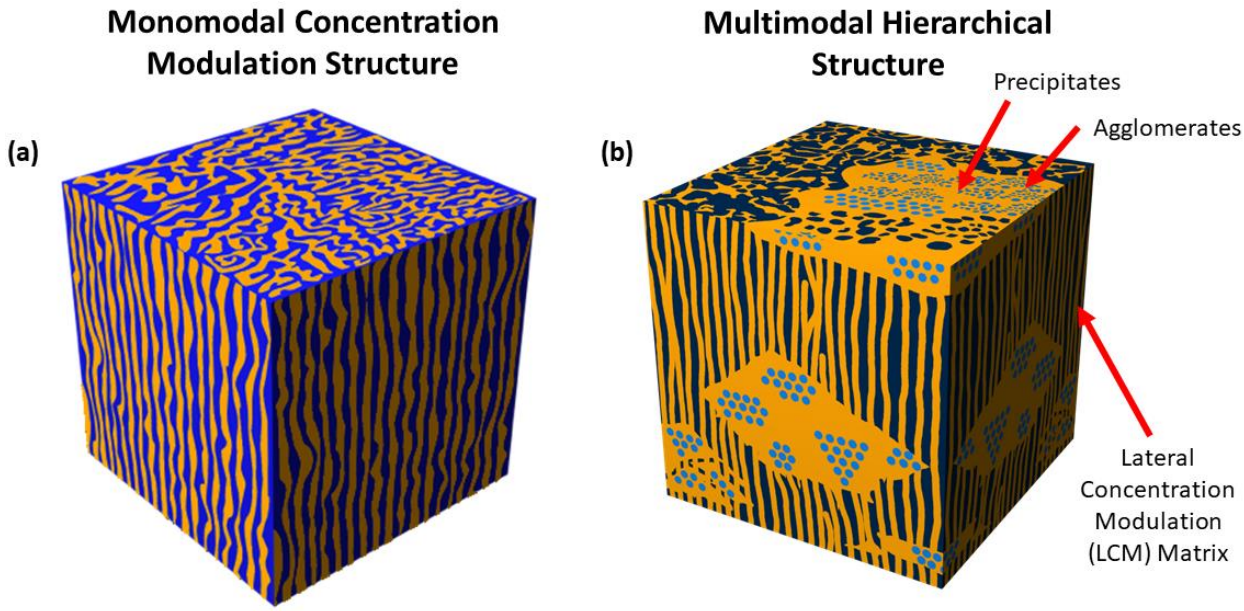

Figure 5-1: Cartoon visualization of the (a) monomodal structure and (b) multimodal hierarchical structure.

The concentration modulations refer to alternating regions rich in one constituent element. The kinetics of formation describing these monomodal structures can be described with an empirical relationship relating elemental interdiffusion length of the landing deposited atoms (adatoms) to deposition flux, surface inter-diffusivity, and width of the surface layer [14,15]. The formation mechanism is further elucidated by incorporating the influence of processing parameters on thin film growth [16] and considering the thermodynamics of phase separation. Indeed, multiple phase-field models have successfully demonstrated the formation mechanisms of the concentration modulation structures in thin films [17,18,19].

The model for monomodal morphologies is insufficient in describing the development of hierarchical film microstructures. Individual elemental interdiffusion length does not account for the formation of agglomerates with precipitates depicted in Fig. 5-1b. Additionally, the presence of pseudomorphism within hierarchical structures point to thermodynamic free-energy potentials that are more complex than previously considered. Psuedomorphism refers to localized metastable free energy minima that result in far-from-equilibrium structures, e.g., FCC structure in Mo-rich nanoprecipitates in Cu matrix [8]. The microstructure suggests that multiple global and local energy minima are present rather than the simple free energy double well potential commonly used to represent spinodal decomposition. This is coupled with interfacial and lattice coherency energies driving the fine-scale microstructure evolution in a manner that warrants further investigation. Certain molecular dynamics [18] and *ab initio* [8] calculations have explored the interface formation and metastability of phases during the phase separation process. A hierarchical morphology suggests that the atomic species are following multiple kinetic pathways during film deposition. The precise kinetic pathways for hierarchical morphology formation during film growth are unclear, although it should be noted that hierarchical structures

can also form due to multi-step solid-state phase transformations in bulk systems, e.g., (α + β) Ti alloys [20].

For the case of thin films, both Cu-Mo [8] and Cu-Ta [21] exhibited hierarchical structures when co-sputtered at deposition temperatures exceeding 600 °C at low deposition rates. The constituent elements were present in both equilibrium and pseudomorphic phases. The Cu-Mo structure contained large Cu-rich agglomerates (~100 nm diameter) and fine FCC Mo precipitates with the agglomerates surrounded by a coherent Cu-Mo BCC LCM matrix. The Cu-Ta structure displayed Ta nano-clusters inside of Cu-rich agglomerations all encompassed by Ta-rich veins. Current mesoscale simulation work [17-19] on co-deposition of immiscible alloys is unable to accurately depict the simultaneous progression of distinct features across multiple length scales reported experimentally in co-deposited PVD films of immiscible elements.

The emphasis of the current work is to probe various systems of co-deposited immiscible alloys to identify the processing conditions and material properties that lead to hierarchical morphologies. The work of Atzmon [14] and Adams [22] provides an important context for the results especially the conclusion that surface diffusion is the prominent method of material transport in a depositing film. The substrate surfaces of the present work are not atomically flat, giving a heterogeneity of surface diffusivity across any flat or faceted regions of the substrate. However, as we are not growing epitaxial films, the variations are negligible for our experiment. The present experiments will help answer the question: why do hierarchical structures exist in some co-deposited systems but not others? Cu-W deposited at room temperature then annealed at 750 °C will coarsen from a solid-solution to form interpenetrating bicontinuous networks but not a hierarchical morphology [23]. Even within the binary alloy of Cu-Ta, metallic thin films fabricated in comparable processing conditions as ref. [21] did not exhibit the trademark distinct

features across multiple length scales. Interestingly, experiments for Cu-Ta films co-sputtered at room temperature that varied the Ta content [24] and induced a Ta phase transformation from metastable β-Ta to equilibrium α-Ta with a heat treatment [25] did not result in a hierarchical structure.

A series of FCC-BCC immiscible alloys: Cu-Mo, Cu-Ag, Cu-Fe, Cu-Ta, Mo-Ag, Cu-Mo-Ag, were co-deposited and characterized to determine the processing parameters and elemental properties that could lead to hierarchical morphologies. The six systems represent a spectrum of elemental properties during phase-separated thin film growth to gauge the effect of the parameters of relative elemental interdiffusion length, the deposition rate, and increased deposition temperature. The resultant film microstructures will also elucidate the formation mechanisms that enable disparate phase-evolution on the micro- and nanoscale.

5.1.1 Co-Deposition and Fabrication Methods

All thin films were co-deposited onto thermally oxidized Si substrates by DC magnetron sputtering in a Kurt J Lesker PVD 75 deposition system. The substrates were 3'' diameter Si with a 1000 nm thick SiO_2 surface layer. Before deposition, the substrates were ultrasonically cleaned in acetone, rinsed with isoproponal alcohol, and dried with filtered compressed air. Five different 2'' diameter targets were used (Cu, Mo, Ag, Fe, Ta), all with at least 99.95% purity, for the various combinations of the binary and ternary alloys. The targets were oriented confocally with a 5'' throw distance towards a rotating substrate at 10 rpm. The sputtering occurs in a vertical direction with the targets depositing material upwards onto the substrates. Base pressure in the chamber prior to sputtering was less than 2.7×10^{-5} Pa. The process gas was Ar which was maintained at a pressure of 0.4 Pa during operation. Precise deposition rates were governed by controlling the DC power supplied to each target. For any film fabrication at an elevated

deposition temperature, a substrate heater resistor coil would heat and maintain a requisite temperature throughout the deposition period. The deposition temperature was monitored with a thermocouple located between the heater and the substrate.

The binary alloy pairings, Cu-Mo, Cu-Ag, Cu-Fe, Cu-Ta, Mo-Ag, were sputtered with nominally equi-atomic composition (e.g. 50 at. % for each element) to create bicontinuous morphologies of separating phases and avoid discrete particle development of a minority phase. The ternary alloy, Cu-Mo-Ag, had a 33.3 at. % composition for each element. The bulk composition of the alloy films was confirmed via x-ray fluorescence (XRF) spectroscopy using a Rigaku Supermini200. Accurate compositions were verified by targeting the appropriate elemental peaks and applying Gaussian peak fitting to reduce noise. A variety of deposition rates and deposition temperatures were used to probe different kinetic conditions for phase-separated thin film growth. The various deposition conditions are detailed below. All noted deposition rates are a combined co-deposition rate for the respective alloy combinations.

A series of Cu-Mo films were deposited at 400, 600, and 800°C with the Cu target activated at 40 W and the Mo target activated at 60 W to deposit at a combined rate of 0.12 nm/s. A second series of Cu-Mo was produced at 600°C with the Cu at 100 W and Mo at 100 W to deposited at a combined rate of 1.4 nm/s. The Cu-Ag was fabricated at 600°C with one film deposited at a combined rate of 0.12 nm/s, target powers of 150 W Cu and 120 W Ag, and a second at a combined rate of 1.4 nm/s, target powers of 250 W Cu and 220 W Ag. The Cu-Fe was sputtered at 300°C with a combined rate of 0.48 nm/s, target powers of 150 W Cu and 110 W Fe. Cu-Ta was deposited at 400, 600, and 800°C with DC power to the targets of 40 W Cu and 60 W Ta for a combined deposition rate of 0.15 nm/s. Mo-Ag was deposited at 600°C with one film deposited at the combined rate 0.12 nm/s, target powers of 60 W for Mo and 50 W for

Ag, and a second film at a deposition rate of 1.4 nm/s, with target powers of 100 W Mo and 100 W for Ag. The Cu-Mo-Ag ternary was deposited at 400, 600 and 800°C with DC power for each target of 100 W Cu, 120 W Mo, and 100 W Ag for a combined deposition rate of 2 nm/s. All films were deposited to a nominal 1 μm thickness with the exception of the Cu-Ta films whose thickness ranged from 700 nm to 1 μm due to coarse grains protruding from the film surface. Post-deposition, the films were left to cool to room temperature in the PVD chamber to inhibit surface oxide formation. Each film was deposited onto substrate rotating at 10 rotations per minute.

	300°C	400°C	600°C	800°C
Cu-Mo		*X*	*X,Y*	*X*
Cu-Ag			*X,Y*	
Cu-Fe	*Z*			
Cu-Ta		*W*	*W*	*W*
Mo-Ag			*X,Y*	
Cu-Mo-Ag		*V*	*V*	*V*

$X = 0.12$ nm/s, $Y = 1.4$ nm/s, $Z = 0.48$ nm/s, $W = 0.15$ nm/s, $V = 2$ nm/s

Table 5-1: List of samples fabricated with respective processing temperatures and deposition rates

5.1.2 Film Characterization Methods

Chemical and microstructural characterization was used to link the morphologies and the processing parameters. Scanning/transmission electron microscopy (S/TEM) foils were prepared using focused ion beam (FIB) milling techniques in a TFS Helios 650 Nanolab SEM/FIB and a TFS Nova 200 Nanolab SEM/FIB. The foils were lifted out and attached to either Si or Mo grids to prevent interference during chemical composition scans. After thinning, the samples were plasma cleaned for a period of 5 to 8 minutes prior to S/TEM characterization on two microscopes, JEOL 3100R05 double-Cs corrected S/TEM and JEOL 200 C-ARM (used in one

characterization period at Northwestern University). The JEOL 3100 R05 was operated at 300 keV to achieve a point-to-point resolution of 0.055 nm for HAADF and BF imaging. The convergent angle for all image collection 111° with a camera length of 8 cm to true Z-contrast HAADF imaging. Energy dispersive X-ray spectroscopy (EDS) compositional maps were collected using a JEOL SDD X-ray detector with a 60 mm^2 active area. The JEOL 200 C-ARM was similarly employed with a 200 keV working voltage.

5.2 Experimental Results

5.2.1 Key Kinetic Parameters

As all the deposited immiscible systems have a similar phase-separating driving force, it is useful to frame the systems in terms of the kinetics of the adatoms arriving on the film surface. While the physical mechanisms that lead to phase separation in bulk materials also occur in films, the process is complicated by two factors as outlined by Atzmon *et al.* [13]: 1) deposition occurs at a fixed, externally imposed rate, and 2) atomic transport occurs preferentially along the advancing surface. The implication is that surface diffusion is the dominant mechanism for film material flux and phase separation at the temperatures relevant to the current experiment. The prevalence of surface diffusion stems from the elemental surface diffusivity being orders of magnitude higher than that for bulk diffusivity. In literature, Al-Ge films deposited at 375°C for half an hour yielded bulk interdiffusion lengths of ~5 nm compared to surface interdiffusion lengths of ~400 nm [14]. In the present case, a “frozen bulk” approximation may be applied in which any elemental bulk diffusion is minimal and nearly negligible for films deposited at lower temperatures. As deposition temperatures increase, the contribution of bulk diffusion to microstructure development becomes more significant especially for films sputtered at T≥800°C. Additionally, the adatoms kinetics can be manipulated with variations in deposition

rate and temperature. It is important to note that during magnetron sputtering the adatoms land on the substrate with a finite incident kinetic energy. The changes in processing deposition rate and temperature further add to the elevated kinetic energy.

An adatom may traverse a specific distance along the film surface before being buried under the oncoming material flux. The distance is termed the surface interdiffusion length, ρ, and is a consequential parameter for phase-separated morphologies. The Atzmon *et al.* model describes the surface interdiffusion length as:

$$\rho = \sqrt{\frac{D_s \delta}{\nu}}, \tag{5-1}$$

where D_s is the surface diffusivity of the species, δ is the thickness of the most recently deposited layer (on the order of interatomic spacing), and ν is the deposition flux. Typically, the adatoms will locally de-mix to minimize system energy which influences the subsequent layers and grow into the homogeneous phase-separated regions. The deposition flux, ν, is in direct competition with the rate of phase separation as increases in ν equate to abbreviated surface interdiffusion lengths. The surface interdiffusion length and the mobility of an elemental adatom are related due to their mutual dependence on diffusivity [26].

Considering the surface interdiffusion length for an individual species is insufficient to explain the concurrent agglomeration and formation of concentration modulation depicted in Cu-Mo and Cu-Ta from literature [19,21]. Comparative systems with nearly identical surface interdiffusion lengths produced monomodal morphologies in some instances and multimodal morphologies in others. Instead, we propose a more accurate parameter is the difference in surface interdiffusion length for the constituent elements. The difference, $\Delta\rho$, is expressed as:

$$\Delta\rho = \sqrt{\frac{(D_s)_A \delta}{\nu}} - \sqrt{\frac{(D_s)_B \delta}{\nu}} \tag{5-2}$$

Where δ and ν are consistent with Eqn. 5-1. The surface diffusivity, D_s, is reliant on the species deposited, A, B, for the binary alloy. The surface diffusivity is given by the well-known expression [27]:

$$D_s = D_0 \exp\left(\frac{-Q}{k_b T}\right) \tag{5-3}$$

Where D_0 is a diffusivity coefficient, Q is the activation energy required for the movement of an atom to an available adjacent site, k_b is Boltzmann's constant [27] and T is temperature. Coupling equations 5-2 and 5-3 reveals the sensitivity of $\Delta\rho$ to temperature and deposition rate which can both be varied as processing parameters.

The Fig. 5-2 plots the $\Delta\rho$ as a function of temperature at the distinct deposition rates of $\nu = 0.12$ and 1.4 nm/s for each of the six co-deposited elemental pairings. For the case of Cu-Mo-Ag, the average between the $\Delta\rho$ for Cu-Mo and Cu-Ag was used. Fig. 5-2a shows the immiscible alloy pairings fall into three kinetic regimes, (i) $\Delta\rho$ steadily increases at T>200°C; (ii) $\Delta\rho$ is muted then rapidly increases at T>600°C; (iii) $\Delta\rho$ increases at T>200°C to a peak at $\approx$ 600 $^\circ$ C, followed by a rapid decrease to $\Delta\rho$ value of zero. The three regimes can be explained by the relative surface mobilities as a function of temperatures for the depositing elements. Regime (i) describes the Mo-Ag system in which both elements have the same proportional increase in surface mobility with respect to increasing temperatures. The regime (ii) alloys of Cu-Ta, Cu-Mo, Cu-Mo-Ag, and Cu-Fe follow a different pattern. As the deposition temperature exceeds 600°C, the surface interdiffusion length of Cu increases at a significantly higher rate than its complementary element which yields a swift escalation in $\Delta\rho$. In regime (iii) Cu-Ag the difference in surface interdiffusion length becomes pronounced above T>200°C in which Ag is

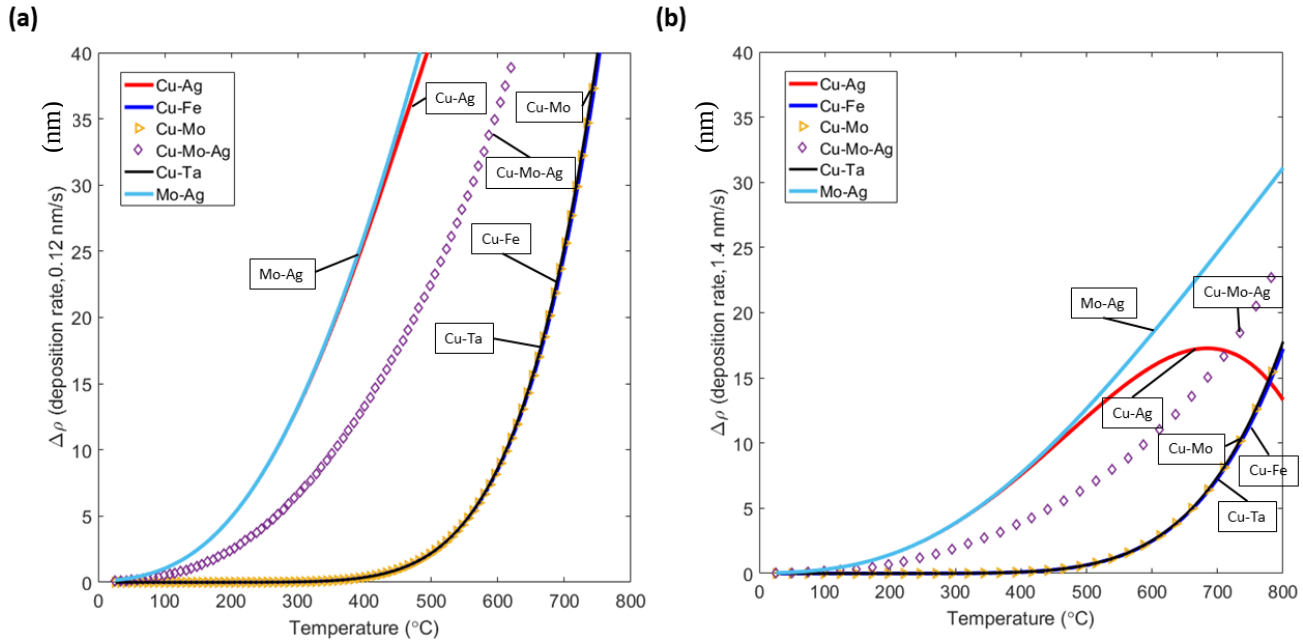

Figure 5-2: The kinetic parameter, $\Delta\rho$, as a function of deposition temperature for the deposition rates (a) ν=0.12 nm/s and (b) ν=1.4 nm/s for the six co-deposited immiscible alloy systems of the present experiment. The elevated deposition temperature increases $\Delta\rho$ for all systems but to different degrees.

significantly more mobile than Cu. However, at T>600°C, both the Cu and Ag have nearly identical ρ which minimizes $\Delta\rho$ to zero.

Fig. 5-2b reveals that increasing the deposition rate to 1.4 nm/s decreases the calculated $\Delta\rho$ for the co-deposited alloys and delays the onset for increased $\Delta\rho$ as a function of elevated temperature. The three kinetic regimes and respective behaviors are still present for the six immiscible systems but the steady increase in $\Delta\rho$ for regime (i) now initiates at 225°C, regime (ii) now exhibits a drastic increase at T>625°C, and the peak and dip of regime (iii) are shifted by 25°C. Fig. 5-2 demonstrates that a lower deposition rate and an elevated deposition temperature allot greater time for surface diffusion and facilitate the movement of a highly mobile species. The agglomeration of that highly mobile species will depend on the kinetic regime. From Fig. 5-2a, the regime (i) will likely form agglomerates with T>400°C. For regime

(ii), agglomeration appears likely with T>700°C. In regime (iii), the temperature window for agglomeration is between 400 and 800°C. With an increased deposition rate in Fig. 5-2b, agglomeration is only likely for regime (ii) at deposition temperatures exceeding 800°C.

Probabilities for agglomeration related to $\Delta\rho$ do not fully encompass the kinetics of hierarchical architectures. The influence of the deposition temperature on the movement of an individual species must also be considered. The direct impact of increased temperature on an element can be quantified with the homologous temperature, T_H. The homologous temperature can be defined as:

$$T_H = \frac{T_{Deposition}}{T_m} \tag{5-4}$$

With $T_{Deposition}$ being the PVD processing temperature and T_m being the melting temperature of a specific element, in Kelvin. Table 2 provides the T_H for the elements relevant to the current immiscible alloy systems. It is important to note that the adatoms of a species is considered highly mobile at T_H > 0.35. The $\Delta\rho$ and T_H create a kinetic threshold above which a hierarchical structure will likely form. Two conditions must be satisfied, the co-deposited immiscible alloy has a significant $\Delta\rho$ value and one element must be in the highly mobile T_H domain.

Deposition temperature	Cu	Ag	Fe	Mo	Ta
673 K	0.495	0.545	0.372	0.232	0.205
873 K	0.642	0.707	0.482	0.301	0.265
1073 K	0.789	0.869	0.592	0.371	0.592

Table 5-2: Homologous temperatures of deposited elements.

5.2.2 Processing-Microstructure Relationship in Immiscible Alloy Films

The fabricated thin films of the six immiscible alloys systems: Cu-Mo, Cu-Ag, Cu-Fe, Cu-Ta, Mo-Ag, Cu-Mo-Ag, contain either monomodal phase-separated microstructure or multimodal hierarchical microstructure. Monomodal, in the present context, is defined as a morphology described by phase-separated concentration modulations of a single length scale (e.g., 10 nm wavelength from start of Cu-rich region to end of Ta-rich region). Fig. 5-3 portrays a monomodal morphology observed in Cu-Fe deposited at 300°C and 0.48 nm/sec. STEM-HAADF images in Fig. 5-3a show Cu and Fe self-assembled into Cu-rich and Fe-rich phase-separated regions, ~20 nm in width, organized into lateral concentration modulation (LCM). The EDS of Fig. 3b further demonstrates the alternating Cu-rich and Fe-rich regions. Planar imaging (not pictured) confirmed the grains of Cu and Fe extending to the film surface. Fig. 5-2a rationalizes the monomodal morphology as Cu-Fe under these processing conditions has a calculated $\Delta\rho$ of approximately 15 nm.

In contrast, the multimodal hierarchical architectures display different features at various length scales in the film. STEM-HAADF images in Fig. 5-4 reveal that Cu-Ta deposited at 600°C and 0.15 nm/sec presents a hierarchical structure as it contains large Cu-rich domains, ~200 to 500 nm in size, surrounded by Ta-rich veins on the microscale but further examination of the Cu-rich regions show an interspersion of Ta clusters on the nanoscale. The Ta clusters are identified by high resolution HAADF images and corresponding FFTs, Fig. 5-4b, indicating a Ta BCC crystalline structure. The hierarchical microstructure is explained by the calculated kinetic parameters. The co-sputtered Cu-Ta has $\Delta\rho$=87 nm and T_H^{Cu}= 0.642, T_H^{Ta}= 0.265. While $\Delta\rho$ is a reduced value, the homologous temperatures denote a highly mobile Cu and a relatively immobile Ta which favors the preferential agglomeration of Cu and leads to the observed

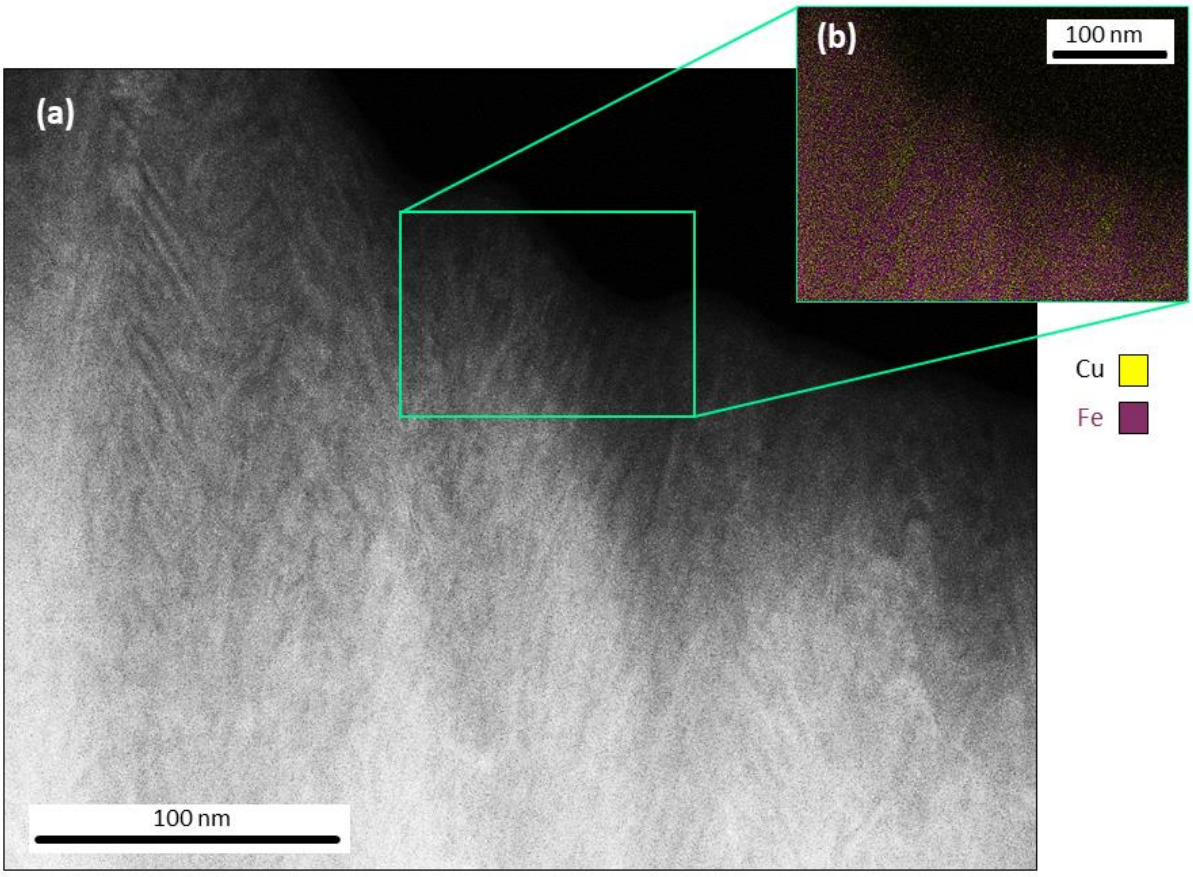

Figure 5-3: (a) Scanning transmission electron microscopy (STEM) high-angle annular darkfield (HAADF) micrograph with atomic number contrast of Cu-Fe with homogeneous LCM morphology. (b) energy dispersive X-ray spectroscopy (EDS) imaging of Cu-Fe demonstrating the alternating Cu-Fe layers.

morphology. Figs. 5-3 and 5-4 provide general examples of monomodal and hierarchical structures. From this point, the discussion will focus upon the underlying mechanisms and the conditions that give rise to hierarchical features in select co-deposited systems.

The processing parameters of deposition rate, ν, and the deposition temperature were varied to determine the influence of $\Delta\rho$ and T_H on the resultant microstructure within an alloy system and comparatively across multiple alloy systems. Fig. 5-5 presents HAADF STEM images of Cu-Mo deposited at ν = 0.12 nm/s and ν = 1.4 nm/s both at 600°C. The micrographs

show hierarchical structure at low ν and homogeneous lateral concentration modulation at higher ν. Although the T_H is constant between Fig. 5-5a and 5-5b, lowering ν by an order of magnitude yields a threefold increase in $\Delta\rho$, from 25 nm to 87 nm. The elevated $\Delta\rho$ for Cu-Mo in Fig. 5-5a thereby surpasses a kinetic threshold for difference in surface interdiffusion length and presents a multimodal morphology.

Fig. 5-6 shows HAADF STEM, HR TEM, FFTs and EDS images of Cu-Mo films co-deposited at 400, 600, and 800°C with ν=0.12 nm/s. Phase contrast within the HAADF images depict large Cu-rich agglomerates surrounded by Cu-Mo bicontinuous matrix for the three films. The presence of a hierarchical structure at 400°C despite a relatively lower $\Delta\rho$ value is consistent with the hypothesis that multiple variables contribute to the immiscible alloy thin film kinetics. The agglomeration behavior for Cu is expected as it is highly mobile at 400, 600, and 800°C [28] with T_H^{Cu} = 0.495, 0.642, and 0.789 respectively. The Mo is relatively immobile, reaching moderate mobility only at 800°C with a T_H^{Mo} of 0.371. In all cases, the Cu-rich agglomerates contained Mo precipitates. The size and nature of the Mo precipitates varied with respect to deposition temperature as elevated temperature led to feature coarsening and a change in crystal structure. Fig. 5-6a reveals the 400°C film has pseudomorphic FCC-Mo precipitates which are energetically preferred as confirmed with literature MD calculations for excess energy in a system due to precipitates [29]. The simulations confirmed that at sizes less than 10 nm, a Mo precipitate prefers an FCC structure within a Cu FCC matrix due to coherency stresses and reduced interfacial energy. From 10 to 20 nm, FCC and BCC Mo have equivalent energy penalties. Above 20 nm in size, BCC Mo precipitates are energetically favorable. Fig. 5-6c shows a size dichotomy for the Mo precipitates in the 800°C film. The population of coarsened

Mo precipitates revert to the equilibrium BCC phase while a number of smaller Mo precipitates remained in the FCC phase.

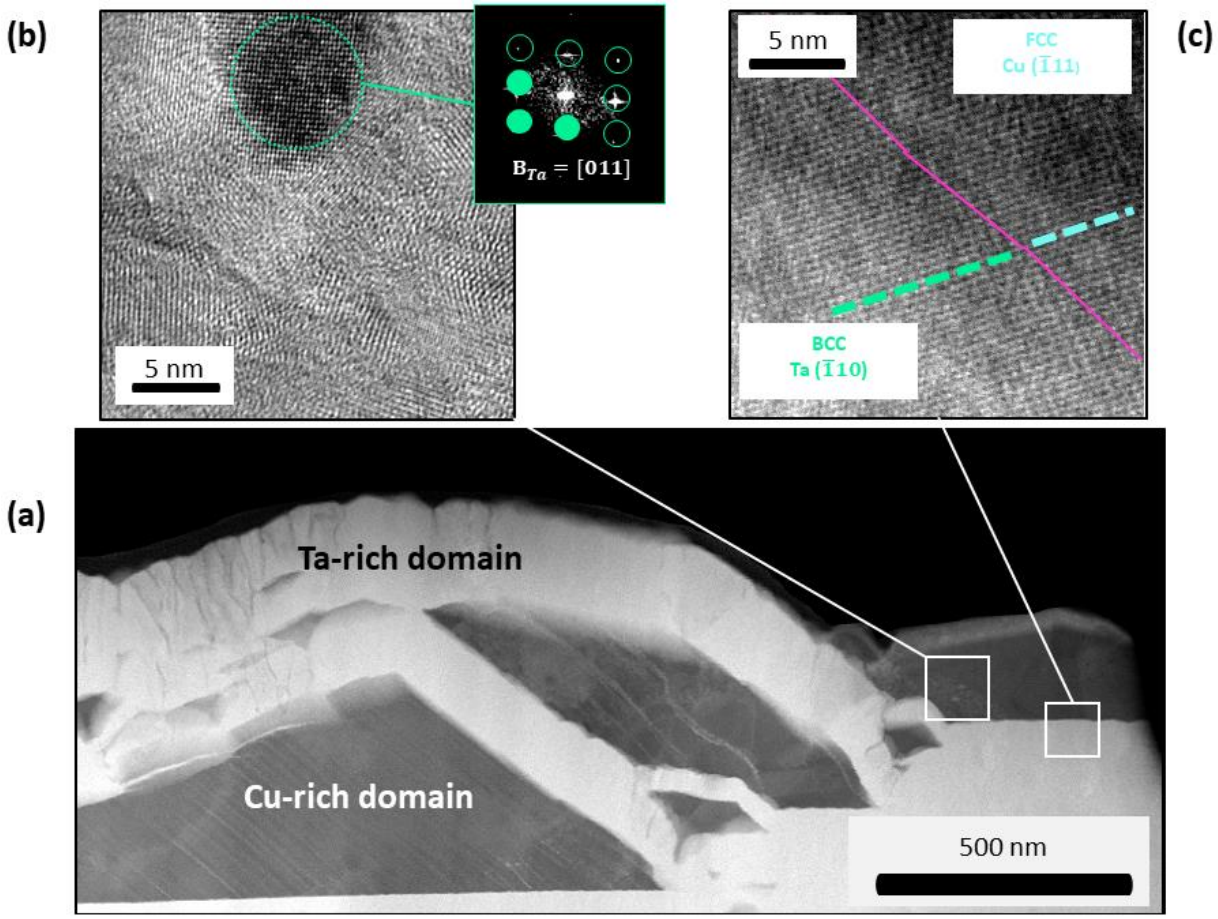

Figure 5-4: (a) STEM-HAADF image of Cu-Ta with hierarchical microstructure morphology. Darker contrast regions are Cu-rich agglomerates which contain a minority of light contrast Ta precipitates. The agglomerates are surrounded by Ta-rich veins. (b) High resolution transmission electron microscopy (HR TEM) micrograph of the Cu agglomerate and incorporated Ta precipitate. The FFT of the encircled area confirms a BCC Ta structure. (c) HR TEM image of the Cu-rich agglomerate and Ta-rich vein interface. The Cu ($\bar{1}$11) plane aligns with the Ta ($\bar{1}$10) plane across the semi-coherent interface.

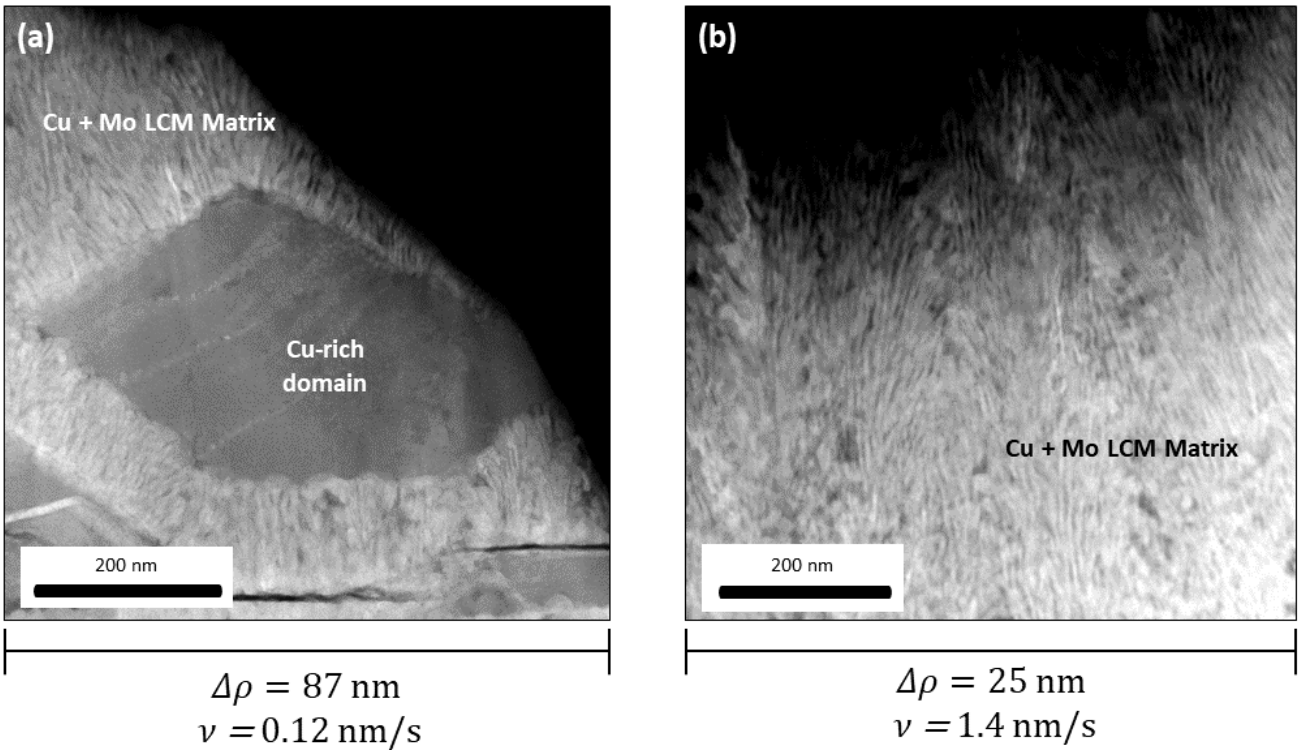

Figure 5-5: STEM-HAADF images of Cu-Mo deposited in identical conditions except for deposition rate. (a) With ν=0.12 nm/s, the Cu-Mo self-segregated in a Cu-rich agglomerate surrounded by a Cu-Mo LCM matrix. (b) With ν=1.4 nm/s, the Cu-Mo formed solely a Cu-Mo LCM structure. Altering the deposition rate by an order of magnitude and subsequentially altering $\Delta\rho$ yielded significant morphological change from a hierarchical to a homogeneous structure.

The HAADF STEM micrographs of Fig. 5-7 compare Cu-Ag and Mo-Ag deposited under identical processing conditions. The Cu and Ag formed equiaxed, Cu-rich and Ag-rich grains ~100 nm in size with equilibrium FCC phases [30]. The features of Cu-Ag resemble those of a similar Ni-Mo-W film which imply a random, soluble initial layer but later phase separation as the deposition proceeded [31]. The Mo-Ag phase separated into Ag-rich domains surrounded by an Ag-Mo LCM matrix. Both films had significant calculated $\Delta\rho$ values of 159 nm for Cu-Ag and 184 nm for Mo-Ag, showing quantitative inclination towards a multimodal morphology according to Fig. 5-2. The rationale for the homogeneity of the Cu-Ag and the heterogeneity of

the Mo-Ag films lies in the T_H values which were T_H^{Cu} = 0.642, T_H^{Ag}= 0.707, and T_H^{Mo}=0.301. The disparity between $T_H^{Mo}$and T_H^{Ag} led to preferential agglomeration of Ag while the closeness of $T_H^{Ag}$and T_H^{Cu}resulted in concurrent equiaxed grain formation.

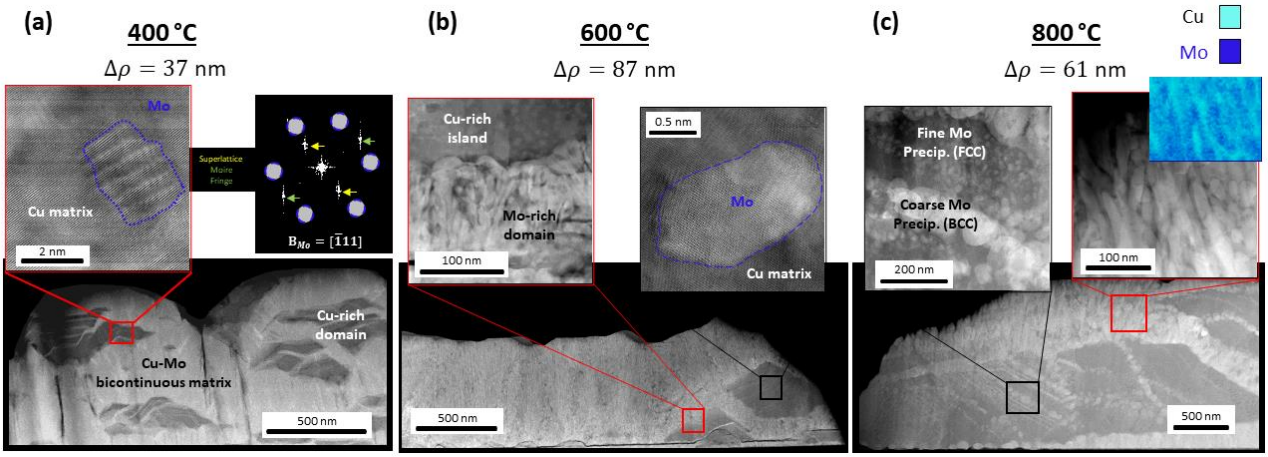

Figure 5-6: Cu-Mo films fabricated at three distinct deposition temperatures (a) 400, (b) 600, (c) 800°C. STEM-HAADF imaging for all three films (bottom row for all three temperatures) with darker contrast regions that are Cu-rich and lighter contrast regions that are Cu-Mo bicontinuous matrix demonstrate hierarchical structures for each deposition with significant Cu-agglomerations containing trace Mo precipitates. The key difference between the three films is the organization of the Mo precipitates. Seen in the 400 °C film (a), the Mo precipitates are ~5 nm in diameter and are organized in a superlattice structure as confirmed by fast Fourier transform (FFT). At 600 °C (b) the Mo precipitates are approximately the same diameter but lose the superlattice structure. The Mo precipitates are noted to be in non-equilibrium FCC Mo phase. At 800 °C (c), there is a size dichotomy in Mo precipitates with a population that is > 20 nm in diameter and some ~10 nm in diameter. The smaller precipitates maintain the non-equilibrium phase while the larger are equilibrium FCC Mo. The energy dispersive X-ray spectroscopy (EDS) in (c) confirms the Cu-Mo bicontinuous matrix.

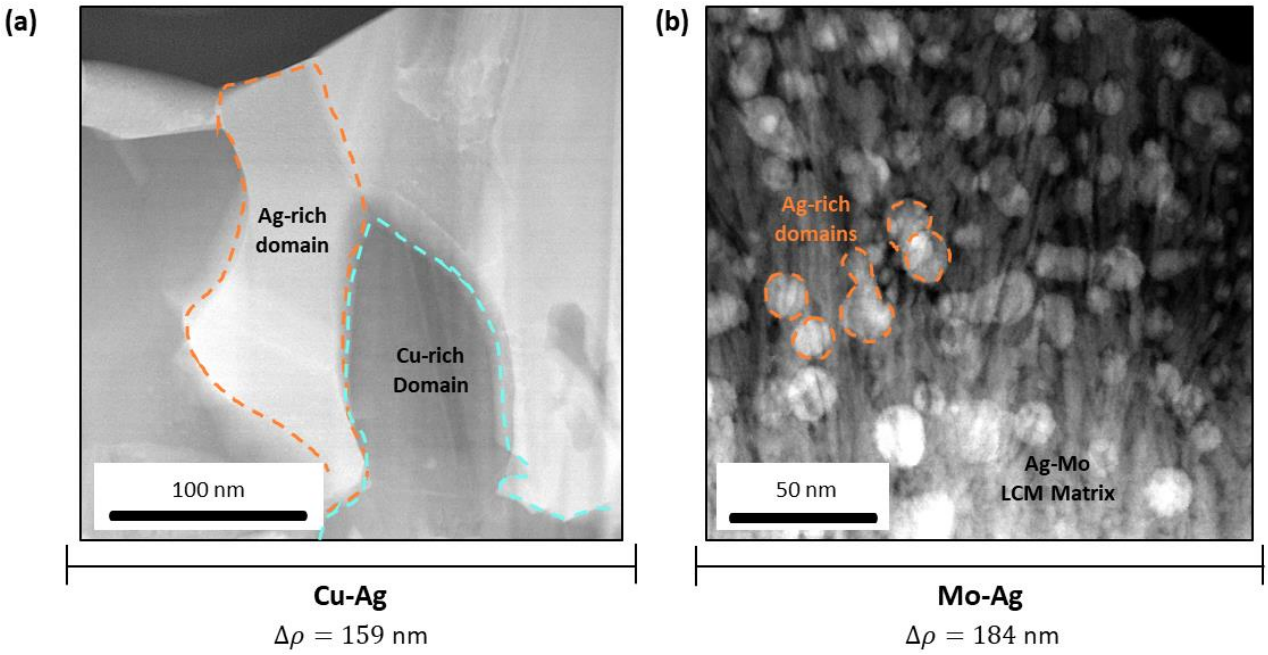

Figure 5-7: STEM-HAADF micrographs of (a)Cu-Ag and (b)Mo-Ag deposited with the same processing parameters, ν = 1.4 nm/s, temperature = 600° C. The Cu-Ag has phase separated into equiaxed Cu and Ag grains while the Mo-Ag displays the hierarchical structure. The significant $\Delta\rho$ in both cases indicate some additional kinetics influencing the formation of hierarchical architecture.

5.2.3 Hierarchical Structures Across Multiple Systems

Co-deposited Cu-Ta, Cu-Mo, Cu-Mo-Ag, and Mo-Ag films all presented hierarchical morphologies when fabricated at an elevated deposition temperature, 600°C, and a reduced deposition rate, ν=0.12 nm/s. STEM-HAADF imaging in Fig. 5-8 shows a similar agglomeration-matrix/vein microstructure on the microscale with precipitate-matrix features on the nanoscale for the four alloys. We observed $\Delta\rho \geq 87$ nm and $T_H \geq 0.35$ for at least one species but $T_H < 0.35$ for the remaining element(s).

The hierarchical architecture of the four systems can be juxtaposed by the scale on which the sample is observed. Cu-Ta in Fig. 5-8a portrays large Cu-rich agglomerates with a non-uniform interspersion of Ta precipitates in their equilibrium BCC phase. The Cu-rich

agglomerates are surrounded by Ta-rich veins which lack any concentration modulations observed in the other three systems. Cu-Mo, as previously discussed in Fig. 5-6, displays Cu-rich agglomerates containing pseudomorphic FCC Mo precipitates all surrounded by Cu-Mo LCM matrix in Fig. 5-8b. In the ternary alloy Cu-Mo-Ag, both Cu and Ag are considered highly mobile with similar surface interdiffusion lengths, ρ = 120 nm, and homologous temperatures, $T_H \geq 0.35$, in contrast to the immobile Mo, ρ = 10 nm. The Cu-Mo-Ag film in Fig. 5-8c depicts a microscopic Cu-rich agglomerate surrounded by a Mo-Ag RCM matrix. Nanoscale inhomogeneities are present in both the Cu-rich agglomerate and RCM matrix. Fine Mo and Ag-rich clusters are observed in the Cu-rich region while spherical Ag-rich domains punctuate the RCM matrix. Lastly, Fig. 5-8d shows the Mo-Ag system consists of Ag-rich domains encapsulated by a Mo-Ag LCM matrix. The nanoscopic features in Cu-Mo-Ag and Mo-Ag are in their equilibrium phases.

5.3 Discussion of Experimental Results

The development of hierarchical morphologies presented in this work depends on the kinetics of thin film growth and the thermodynamics of immiscible systems. To deconvolve the underlying driving forces, it is pertinent to examine the phase-separation process for each length scale separately then combine them to understand the growth of the entire structure. First, the microscopic evolution will be examined to identify what induces the heterogeneous phase separation with simultaneous agglomeration and concentration modulation formation in hierarchical morphologies. Second, the energetics of nanoscale features will be discussed in the context of coherency stresses and interfacial energies to explain any metastable phases or lack thereof in the microstructure.

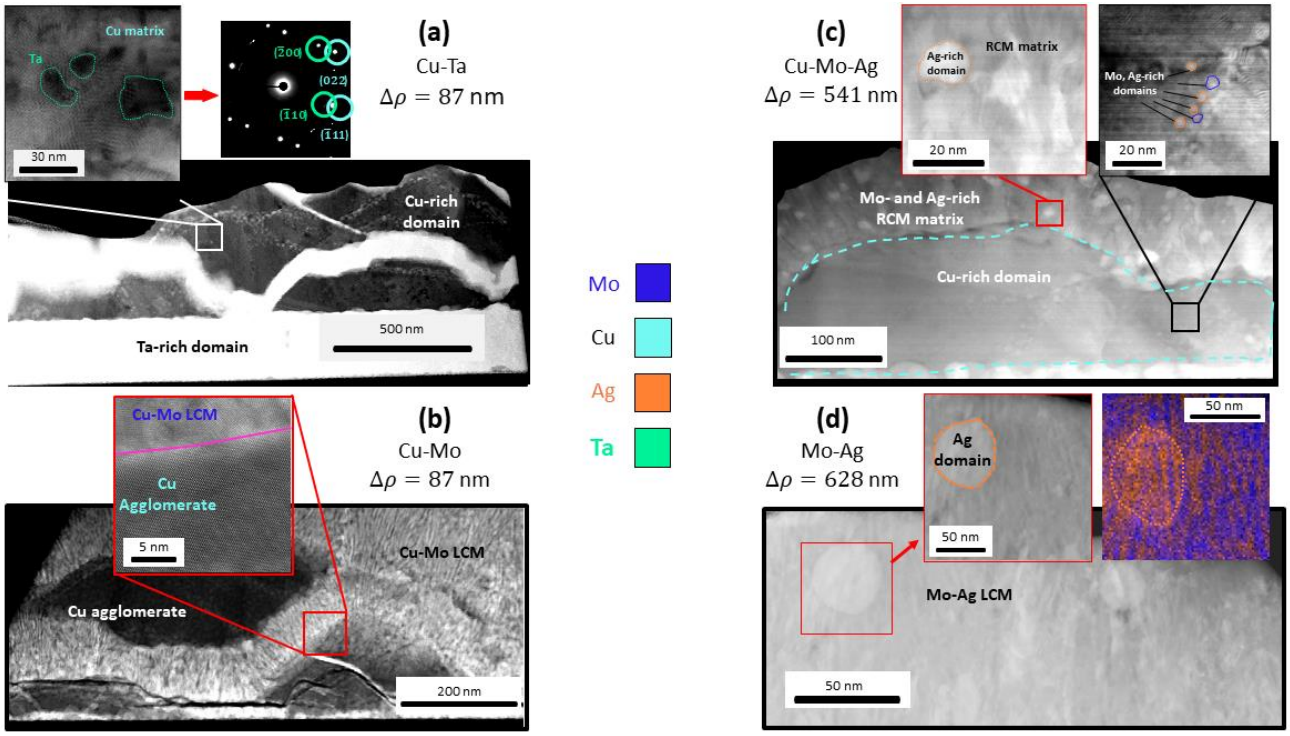

Figure 5-8: STEM-HAADF image (larger images) of multiple systems presenting hierarchical morphologies for films deposited at ν = 0.15 nm/s (Cu-Ta) and ν = 0.12 nm/s (Cu-Mo, Cu-Mo-Ag, Mo-Ag), temperature = 600° C. The immiscible alloys (a) Cu-Ta, (b) Cu-Mo, (c) Cu-Mo-Ag, and (d) Mo-Ag, have a range of $\Delta\rho$ values from 0.0087 to 0.0628 but all consistently display "structures composed of structures". Various insets of HR TEM micrographs (a,b,c), FFTs (a), and an EDS (d) image confirm the existence of features on multiple length scales for all four systems and suggests similar kinetic pathways during the formation process despite the variety of deposited species.

5.3.1 Primary Microscopic Phase Separation

Equilibrium thermodynamics favor phase separation for all binary and ternary co-deposited samples discussed in this experiment [32]. Each set of elements was immiscible at the processing temperatures used during PVD. Thus, the comparative morphological variation across the six tested systems can be attributed to the film growth kinetics and constituent kinetic parameters of $\Delta\rho$ and T_H. The hierarchical structures were only noted in film processed with $\Delta\rho \geq 20$ nm while also containing at least one element with $T_H \geq 0.35$ and one element

T_H <0.35. As shown from Fig. 5-2 and Table 5-1, these conditions only arise at reduced deposition rates and elevated temperatures. The result is a strong disparity in elemental mobility during deposition. Normally, once the landing adatoms reach the substrate surface they will phase-separate as described in the original model of Atzmon *et al*. [14] In the conditions of significant elemental mobility difference, the highly mobile element will de-mix from the other element(s) and diffuse along the film surface into agglomerates during the deposition to reduce the interfacial energy between phase-separated regions. The less mobile element will diffuse relatively short distances before being buried and "frozen" by the oncoming deposition flux. The rapid agglomeration engulfs the less-mobile element which then become minority precipitates; a key characteristic of the hierarchical structures. Of interest is the phase fraction of the thin film and its influence on morphology. All the experimental binary alloys are 50-50 at.% as confirmed by XRF. However, as the highly mobile element agglomerates it induces localized regions of highly unequal phase fractions. Area image analysis shows the agglomerates and minority less-mobile element phase fraction ranges between 90-10 to 95-5 at.% which drive precipitate development. The remaining quantities which do not form the agglomerates and precipitates will concurrently phase separate into concentration modulations or a vein-like structure as specifically noted in Cu-Ta of Fig. 5-8a. The microscopic phase separation can be termed the "primary phase separation".

Fig. 5-5 demonstrates the morphological sensitivity towards deposition rate and $\Delta\rho$ within the single Cu-Mo system. Although there is a consistent mobility difference for both depositions at 600°C as $T_H^{Cu} = 0.642$ and T_H^{Mo}=0.301, a significant change in ν and a relatively small change in $\Delta\rho$ yielded distinct monomodal and hierarchical microstructures. Increasing the deposition temperature and consequentially the elemental mobility difference in Fig. 5-6 led to

the same general microscopic features. The higher temperature equated to greater Cu agglomeration and activates the bulk diffusion which allows coarsening of the Mo precipitates. Fig. 5-7 proved that a system with $\Delta\rho \geq 37$ nm requires the homologous temperature difference to yield a hierarchical structure. The Cu and Ag adatoms have approximately equal mobility with an equal propensity for agglomeration leading to the equiaxed Cu-Ag grains. In contrast, Ag-Mo had a T_H^{Ag}= 0.707 and a T_H^{Mo}=0.301 resulting in Ag agglomerations and the characteristic multimodal microstructure.

Any *in situ* observation of the exact microscopic growth phenomena for hierarchical structures is complicated. Pausing the film deposition for a few minutes [9] or limiting the kinetic energy by depositing at room temperature [33] will yield amorphous or nanocrystalline phase separated regions incomparable to the present experiment. Mesoscale modeling arises as the likely candidate for true comprehension of the multi-component multimodal architectures [34]. Coding frameworks have successful replicated the formation of monomodal morphologies in immiscible systems [17, 35]. Other phase-field models have incorporated non-equilibrium oxide formation into phase separation during binary film growth [36]. However, a framework has yet to replicate the simultaneous multiscale evolution of hierarchical structures with appropriate scaling and both equilibrium and pseudomorphic phases present.

5.3.2 Secondary Nanoscale Phase Separation

As established in the previous section, immiscible alloy vapor deposited films at elevated temperatures exhibit phase separation reaction on account of high enthalpy of mixing. The large disparity in mobilities of participating species and differing surface self-diffusivities have resulted in preferential agglomeration of one species and a microscopic mechanism leading to hierarchical structures shown comprehensively in Fig. 5-8.

Nanoprecipitates thus formed are observed to be uniformly interspersed in specific regions of the agglomerates. The nature of the precipitates reveals some important features. Firstly, the atoms forming these precipitates belong to species that is already chemically lean in the surrounding medium. Secondly, the medium in which these precipitates are embedded in is an agglomerate that was formed earlier during primary phase separation reaction. Thirdly, the precipitates share either coherent or semi coherent interface with the medium. Thin film studies on the Cu-W system synthesized by magnetron co-sputtering [9] linked interface coherency with spinodal-like modulations in self-assembled multilayered structures. Further, the size and distribution of precipitates indicate that the atoms involved in their formation travelled infinitesimally small distances to cluster locally and form several nano sized precipitates. This process is kinetically limited by the lower mobility of these atoms as the reaction occurs in the bulk where activation energies are significantly higher than that on the surface [37]. There is also limited supply of these precipitate forming atoms because the medium in which they form are already compositionally lean in their respective species after having undergone primary phase separation reaction earlier. Very limited availability of atoms combined with higher barrier to diffuse over significant distances results in small precipitate-clusters interspersed inside the agglomerates.

The above observations suggest that in addition to primary phase separation reaction that enabled diffusion over long distances and allowed for initial agglomeration of highly mobile species, a possible secondary phase separation reaction that is akin to diffusion-less transformation or a spinodal decay at a lesser degree is in the offing leading towards formation of nanoprecipitates. Typically, the phase separation in immiscible alloy-system is represented by double-welled Gibbs' free energy curve with material flux guided via spinodal decomposition

[38]. The underlying Gibb's equation combines enthalpy of mixing, ΔH, and entropy of mixing, ΔS, as:

$$\Delta G = \Delta H - T\Delta S \tag{5-5}$$

While the entropy curve by definition is concave upwards ($\Delta S = -R\sum x_i ln\, x_i$, with x_i representing the population of a species), enthalpy acts as a strong factor in deciding the shape of the Gibb's curve. A strong, positive enthalpy of mixing gives rise to a double-welled Gibb's free energy curve of Eqn. 5-6 with a localized maxima and two inflection points. This is especially true at elevated temperatures when the competition between enthalpy and entropy is equally strong in magnitude. Conventionally, enthalpy of mixing, ΔH_{mix}, is calculated using a simple linear model based on the following equation:

$$\Delta H_{mix} = H_{mixture} - \sum x_i\, H_i \tag{5-6}$$

with $H_{mixture}$ being the constant enthalpy of mixing, and $\sum x_i\, H_i$ is the summed product of energetics of the respective species. The resulting parabolic curve is similar to entropy but with opposite concavity. A more complex model for enthalpy of mixing involving a higher degree polynomial causing multiple maxima with corresponding inflection points in the Gibbs' free energy profile. In addition to this, majority of the thermodynamic analysis is carried out assuming ideal conditions of thermodynamic equilibrium achieved in a reversible manner without restriction on kinetic aspects of phase separation. Any possible secondary or higher order phase separation reactions leading towards formation of metastable phases are often overlooked and difficult to capture when subjected to unique processing conditions like vapor deposition.

As the characterization in the present experiment occurred post-deposition, there is ambiguity that inhibits a definitive statement on the vehicle for secondary phase separation. Empirical evidence points to either a nucleation and growth transformation or a complex

spinodal decomposition being the likely mechanisms for nanoprecipitate evolution. However, the exact nature of such spinodal decomposition is complicated by metastable phases and their implied complex Gibbs' free energy curve with additional local minima, $\frac{\partial G}{\partial c} = 0$, and multiple wells. Two phase ($\alpha + \beta$) Ti alloys provide some insight on nanostructure evolution as they have nanoscale features comparable to the current work [20]. The kinetic pathways and phase transitions in the Ti alloys are reliant on undercooling, the concentrations of existing composition, and processing pressures. The co-deposited immiscible alloys likely follow a similar dependency with different non-conventional processing conditions [39] emphasizing different pathways and leading to small nuances in the nanoscale evolution as evidenced in Fig. 5-6.

5.3.3 Pseudomorphism in Nanoprecipitates

Metastable phases formed during growth are a consequence of material processing under forced constraints. While thermodynamics determines the potential for phase separation, vapor deposition techniques can kinetically limit this phase separation reaction by varying the flux of freshly deposited layers and by altering the substrate temperature either to suppress or enhance the mobility of participating atoms. Nanoprecipitates formed under such metastable conditions show pseudomorphic lattice structures in Cu-Mo and Cu-Ta systems as seen in Figs. 5-6 and 5-8.

Pseudomorphism has been studied extensively in thin films deposited by molecular beam epitaxy techniques where a deposited layer assumes the lattice structure corresponding to substrate that is different from bulk equilibrium structure. The ensuing coherent interface between deposited material and substrate results in elastic misfit strain and is sensitive to critical thickness of the deposited layer above which transition to bulk equilibrium structures is observed [40,41]. Contrastingly, the pseudomorphism observed in hierarchical structures are seen in

precipitates that appear to have formed during secondary phase separation reaction by migrating and clustering locally inside already agglomerated majority phase with lattice structures not observed in bulk equilibrium conditions.

Structural stability of these pseudomorphic nanoprecipitates incur an energy penalty during the formation of an interface and the associated pseudomorphic crystal structure. The interplay between surface-interface coherency [42] and system size [43] permits local minima in free energy corresponding to metastable pseudomorphic states accessible only with specific processing conditions. First-principles calculations by Aguayo *et al.* [44] on Ti, Zr and Hf demonstrate existence of a locally stable FCC structure based on elastic stability criteria. Analytical studies by Tomanek *et al.* [45] on structural stability of nanosized clusters show close-packed FCC structures to be more stable than bulk BCC structure in metals like V, Nb, Cr, Mo, W and Ta. Relating these studies to the present work, at early stages of precipitate formation there is a tendency towards close-packed FCC structure to align with the matrix-agglomerate material. As the precipitate size increases, it will undergo a martensitic transformation to bulk equilibrium BCC structure. Such transition is noted in the Cu-Mo system from Fig. 5-6b to 5-6c. The transformation occurs at a critical size which is decided by the competition between precipitate-matrix interfacial energy and cohesive energy of the respective lattice structures at prevailing temperatures. Similar structural evolution has been reported in W nanoclusters during decomposition of $W(CO)_6$ vapors evolving from an amorphous to crystalline FCC structure before assuming a final bulk equilibrium BCC structure [46]. with increasing cluster size.

The analytical model by Tomanek *et al.* [45] provides energy-based criterion at which a cluster's lattice structure transforms from closed packed FCC to equilibrium BCC structure. Smaller clusters will have a higher proportional of surface atoms which contribute to high

surface energy values. It is likely that the observed transformation in lattice structures is to minimize this surface energy and the condition for this transformation is given by the following equation [45]:

$$\frac{E_{bcc}-E_{fcc}}{E_{bcc}} = \frac{1}{N}\left\{\sum_{i=1}^{N_s}\left[\left(\frac{Z_i}{Z_b}\right)^{\frac{1}{2}}-1\right]_{fcc} - \sum_{i=1}^{N_s}\left[\left(\frac{Z_i}{Z_b}\right)^{\frac{1}{2}}-1\right]_{bcc}\right\}, \qquad (5\text{-}7)$$

Where the left-hand side of the equation represented as ΔE in the Fig. 5-9 is the difference in formation energies between BCC structure and FCC structure normalized by the formation energy for bulk structure (BCC in this case). N and N_s represent total number of atoms and number of surface atoms in the cluster, respectively. Z_i and Z_b refer to coordination number of 'i'th atom and a bulk atom in the corresponding lattice, respectively. The summation on the right-hand side of the equation was individually computed for FCC and BCC structures by mapping surface atoms on spherical clusters and extracting coordination numbers data using LAMMPS [47] eventually resulting in the solid curve shown in Fig. 5-9. The above criterion is satisfied at a unique N value for each specie implying a critical number, N_c of atoms required for the cluster to undergo structural transformation as indicated in Fig. 5-9. The critical cluster size for select elements relevant or comparable to the current work, Mo, W, Fe, Ta, to highlight the phases seen experimentally.

Though the transformation from pseudomorphic structure to bulk equilibrium structure has been thoroughly established in theory and in experiments, the accuracy of the N_c is debatable and hard to capture in some species. This stems from the fact that the medium in which clusters and precipitates evolve, strongly decides the surface-interface relationship which in turn influences the N_c. Furthermore, N_c will vary under non-equilibrium conditions of formation and growth where complex thermodynamic and kinetic factors are at play. Structural variations

induced by stress, irradiation, electric/magnetic fields, vibrations, etc. in the process of microscopic examinations cannot be completely ruled out.

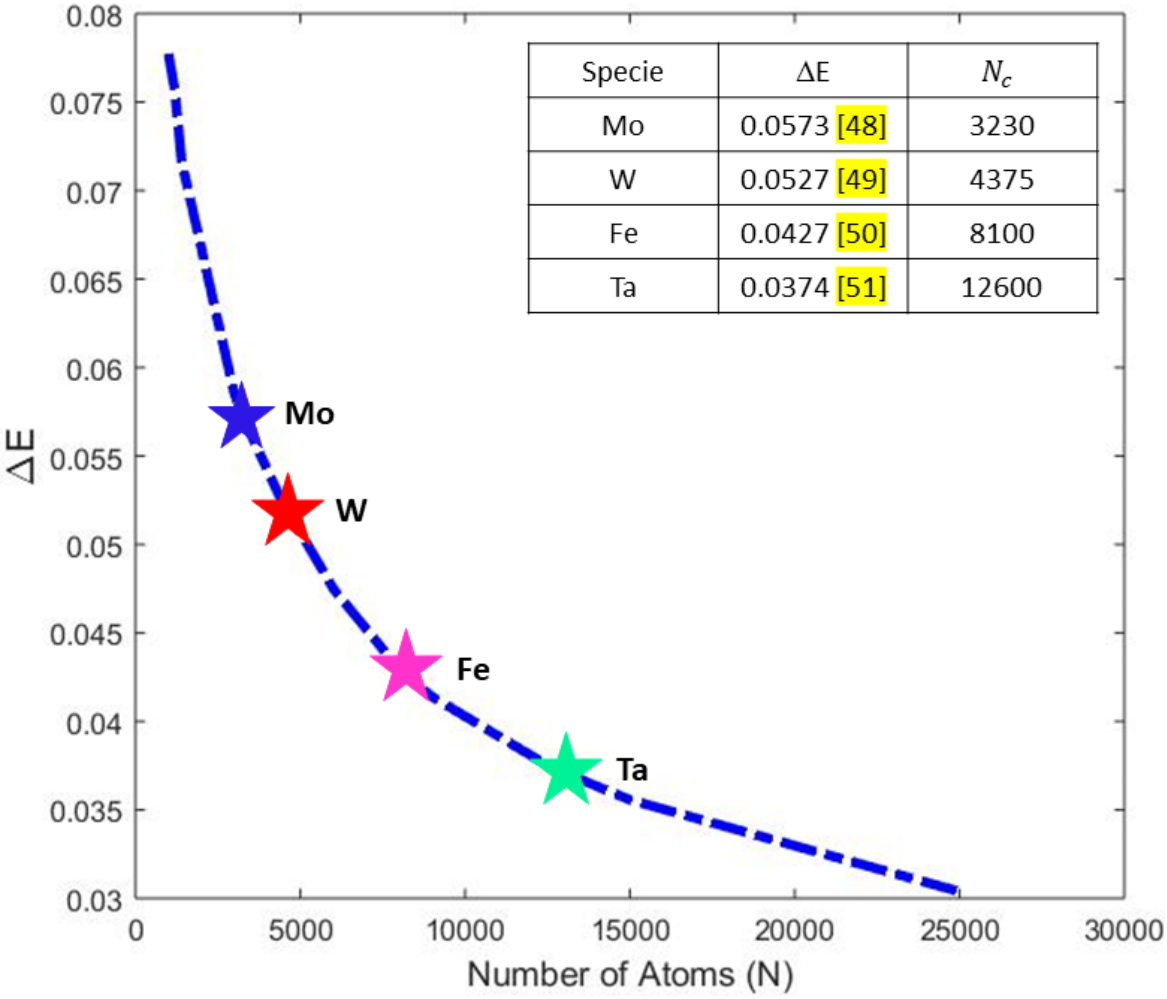

Specie	ΔE	N_c
Mo	0.0573 [48]	3230
W	0.0527 [49]	4375
Fe	0.0427 [50]	8100
Ta	0.0374 [51]	12600

Figure 5-9: Analytically determined structural stability of nanoclusters depicting the critical number of atoms, N_c, at which the lattice structure shifts from close packed FCC to equilibrium BCC for select elements in accordance to Eqn. 5-7. The vertical axis is normalized energy and the inset is a table which provides a general notion of critical cluster sizes for Mo and Ta seen in the hierarchical structures of the present micrographs.

5.3.4 Morphology Map for Hierarchical Structures

The present work can be summarized with two morphology maps of the empirically observed microstructures for the co-deposited immiscible alloy systems. The alloy systems are

noted as forming monomodal or hierarchical morphologies as a function of processing kinetics in the maps of Fig. 5-10a,b. The resultant morphologies of the experimental systems are plotted with respect to the kinetic parameters, the comparative homologous temperature, ΔT_H, and the difference in surface interdiffusion length, $\Delta\rho$, for Fig. 5-10a and for deposition rate, ν, and ΔT_H for Fig. 5-10b. The comparative homologous temperature is evaluated as the difference in T_H for the constituent elements (taken as the average difference in Cu-Mo-Ag). The ΔT_H is selected due to the characterization of Cu-Fe in Fig. 5-3 and Cu-Ag in Fig. 5-7 which indicate the relative difference in constituent homologous temperature is critical to preferential agglomeration of one species and thus multimodal morphologies.

Fig. 5-10a,b show that no single kinetic parameter can be directly correlated to multimodal microstructure. Instead, all three parameters, $\Delta\rho$, ν, and ΔT_H, contribute to hierarchical formation. The ΔT_H is most significant driver since the monomodal microstructures are directly correlated to low ΔT_H values. At the threshold ΔT_H>0.25, noted as dotted lines in Fig 5-10a,b, the co-deposited immiscible alloys yielded hierarchical structures in all cases but one. Fig. 5-7 indicated that the kinetic parameter $\Delta\rho$ can still be affiliated with one element having sufficient kinetic energy to preferentially agglomerate to engulf the immobile complementary element and initiate the multimodal formation. However, Fig. 5-10a reveals that the threshold $\Delta\rho$ value is likely quite low and must be paired with elevated ΔT_H for hierarchical self-assembly. The $\Delta\rho$ value is dependent on a number of inputted factors including deposition temperature, activation energy for diffusion of a species, and deposition rate, the combination of which obfuscate the direct correlation of $\Delta\rho$ with multimodal morphologies.

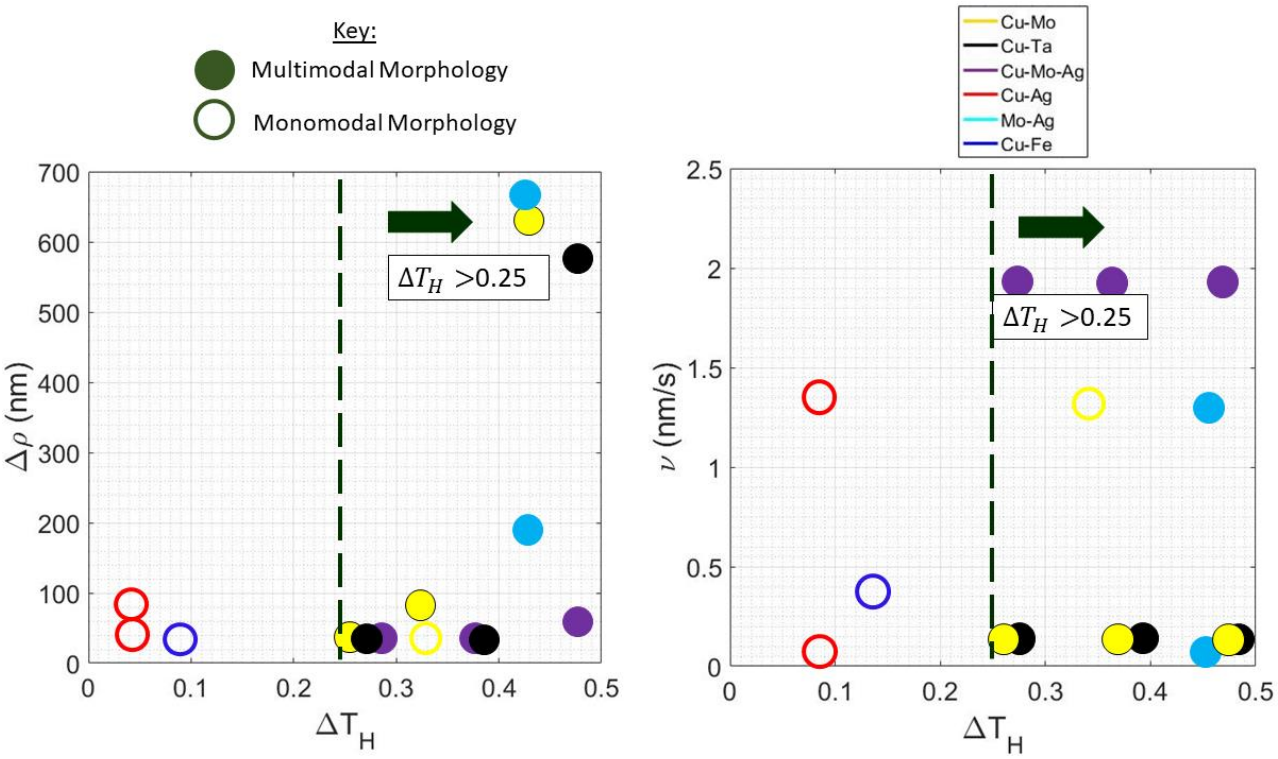

Figure 5-10: (a) Morphology map with the variables $\Delta\rho$ and ΔT_H, the difference in homologous temperature of the constituent species. The empirically observed morphologies of the experimentally deposited systems are plotted as a function of their processing conditions. Two resultant groupings are noted. First, only multimodal morphologies were present at $\Delta\rho$>10 nm. Second, with $\Delta\rho$<10 nm, any systems with ΔT_H<0.25 yielded homogeneous morphologies. (b) Second morphology map with ν and ΔT_H. At the low deposition rates probed in this experiment, the ΔT_H has significantly higher influence on the resultant microstructure morphology. The dashed vertical lines indicate the ΔT_H >0.25 in both maps (a) and (b) which appears to be the threshold for monomodal vs. multimodal architectures except for the single Cu-Mo sample deposited at 600°C.

The deposition rate, ν, has a significant influence on morphology when examined across a large range of rates. This was noticed in Fig. 5-5 with a change in morphology as ν increased by an order of magnitude from Fig. 5-5a to 5-5b. However, the present experiment probed ν across a range of very low to low values, 0.12 to 2 nm/s, which reduced the prominence of the deposition rate and its effect on surface interdiffusion lengths. Increasing ν to medium or high rates would limit the surface interdiffusion length of all deposited species and suppress multimodal

structures. There is likely a transition point in deposition rate unique to each alloy pairing in which the morphologies change from monomodal to multimodal. While the present study examines six co-deposited immiscible systems, the trends apparent in Fig. 5-10a,b may be predictive of the morphologies in a number of deduced immiscible alloy systems adding another dimension to alloy maps as mentioned by Zhang *et al.* [52].

5.4 Conclusions

Experimental micrographs and energetic theory combine to present a comprehensive description of hierarchical structures in co-sputtered immiscible alloys and their formation mechanisms concurrent on the microscopic and nanoscales. The hierarchical structures have a primary and secondary phase separation occurring simultaneously with the pathway:

1.) At the microscopic level, the primary phase separation at the processing conditions of low deposition rates and elevated deposition temperatures induce the landing adatoms of the one species with significant surface diffusivity to agglomerate to reduce the energy of the system. The agglomeration will trap a trace amount of the second species which become nanoprecipitates. The remaining material for both species will form concentration modulations that will surround the agglomerates.

2.) At the nanoscale, the nanoprecipitates will evolve according to the secondary phase separation. Longer deposition times and increased temperature incentivize bulk diffusion which will coarsen the microstructure. The nanoprecipitates likely evolve via a nucleation and growth transformation or complex spinodal decomposition, sometimes occupying a pseudomorphic state then transitioning to their bulk equilibrium state, possibly via martensitic transformation as they become larger in size.

The above steps are relevant for co-deposited immiscible systems which phase separate into distinct regions. Furthermore, the hierarchical structures will only develop under specific kinetics with high T_H values, low ν, and significant $\Delta\rho$ for the alloy.

References

[1] R. Lakes. Materials with structural hierarchy. *Nature*. 361:511-515, 1993.

[2] P. Braun and R. Nuzzo. Knowing when small is better. *Nature Nanotechnology*. 9:962-963, 2014.

[3] A. Chen, Q. Su, H. Han, E. Enriquez, Q. Jia. Metal oxide nanocomposites: a perspective from strain, defect, and interface. *Advanced Materials*. 31:1803241, 2019.

[4] Q. Li, S. Xue, P. Price, X. Sun, J. Ding, Z. Shang, Z. Fan, H. Wang, Y. Zhang, Y. Chen, H. Wang, K. Hattar, X. Zhang. Hierarchical nanotwins in single-crystal nickel with high strength and corrosion resistance produced via a hybrid technique. *Nanoscale.* 12:1356-1365, 2020.

[5] Y. Cui, B. Derby, N. Li, N.A. Mara, A. Misra. Suppression of shear banding in high-strength Cu/Mo nanocomposites with hierarchical bicontinuous intertwined structures. *Materials Research Letters*. 6:184-190, 2017.

[6] Y. Cui, B. Derby, N. Li, A. Misra. Fracture resistance of hierarchical Cu-Mo nanocomposite thin films. *Materials Science Engineering A*. 799:139891, 2021.

[7] B. Derby, J.K. Baldwin, D. Chen, M. Demkowicz, Y. Wang, A. Misra, N. Li. Faceted He-filled “pancakes” confined within nanoscale metal layers. *JOM.* 72:145-149, 2020.

[8] B. Derby, Y. Cui, J.K. Baldwin, R. Arroyave, M. Demkowicz, A. Misra. Processing of novel psuedomorphic Cu-Mo hierarchies in thin films. *Materials Research Letters.* 7(1):1-11, 2019.

[9] T. Xie, L. Fu, W. Qin, J. Zhu, W. Yang, D. Li, L. Zhou. Self-assembled metal nano-multilayered film prepared by co-sputtering method. *Applied Surface Science*. 435:16-22, 2018.

[10] J. Xue, Y. Li, L. Hao, L. Gao, D. Qian, Z. Song, J. Chen. Investigation on the interfacial stability of multilayered Cu-W films at elevated deposition temperatures during co-sputtering. *Vacuum*. 166:162-169, 2019.

[11] A. Bahrami, C.F. Onofre Carrasco, A. Delgado Cardona, T. Huminiuc, T. Polcar, S. E. Rodil. Mechanical properties and microstructural stability of CuTa/Cu composite coatings. *Surface Coatings Technology.* 364:22-31, 2019.

[12] C.M. Muller, A. Sologubenko, S. Gerstl, R. Spolenak. On spinodal decomposition in Cu-34 at.% Ta thin films – an atom probe tomography and transmission electron microscopy study. *Acta Materialia*. 89:181-192, 2015.

[13] B. Derby, Y. Cui, J.K. Baldwin, A. Misra. Effects of substrate temperature and deposition rate on the phase separated morphology of co-sputtered, Cu-Mo thin films. *Thin Solid Films*. 647:50-56, 2018.

[14] M. Atzmon, D.A. Kessler, D. Srolovitz. Phase separation during film growth. *Journal of Applied Physics*. 72:442-446, 1992.

[15] C. Adams, M. Atzmon, Y.T. Cheng, D. Srolovitz. Phase separation during co-deposition of Al-Ge thin films. *Journal of Materials Research*. 7:653-666, 1992.

[16] J. Thornton. Influence of apparatus geometry and deposition conditions on the structure and topography of thick sputtered coatings. *Journal of Vacuum Science and Technology*. 11:666-670, 1974.

[17] A. Kumar, B. Derby, R. Raghavan, A. Misra, M. Demkowicz. 3-D phase-field simulations of self-organized composite morphologies in physical vapor deposited phase-separating binary alloys. *Journal of Applied Physics*. 126:075306, 2019.

[18] J. Stewart, R. Dingreville. Microstructure morphology and concentration modulation of bicontinuous nanocomposite thin-films during simulated physical vapor deposition. *Acta Materialia*. 188:181-191, 2020.

[19] Y. Lu, C. Wang, Y. Gao, R. Shi, X. Liu, Y. Wang. Microstructure map for self-organized phase separation during film deposition. *Physical Review Letters*. 109:086101, 2012.

[20] T. W. Heo, D. Shih, LQ Chen. Kinetic pathways of phase transformations in two-phase Ti alloys. *Metallurgical and Materials Transactions*. 45A:3438-3445, 2014.

[21] M. Powers, B. Derby, A. Shaw, E. Raeker, A. Misra. Microstructural characterization of phase-separated co-deposited Cu-Ta immiscible alloy thin films. *Journal of Materials Research*. 35:1531-1542, 2020.

[22] C. Adams, D. Srolovitz. Monte carlo simulations of phase separation during thin-film codeposition. *Journal of Applied Physics*. 74:1707-1715, 1993.

[23] F.T. Vullers, R. Spolenak. From solid solutions to fully phase separated interpenetrating networks in sputter deposited “immiscible” W-Cu thin films. *Acta Materialia*. 99:213-227, 2015.

[24] C. M. Muller, S. Parviainen, F. Djurabekova, K. Nordlund, R. Spolenak. The as-deposited structure of co-sputtered Cu-Ta alloys, studied by X-ray diffraction and molecular dynamics simulations. *Acta Materialia*. 82:51-63, 2015.

[25] S.L. Lee, M. Doxbeck, J. Mueller, M. Cipollo, P. Cote. Texture, structure, and phase transformation in sputter beta tantalum coating. *Surface Coatings Technology*. 178:44-51, 2004.

[26] K. Fukutani, K. Tanji, T. Saito, T. Den. Fabrication of well-aligned Al nanowire array embedded in Si matrix using limited spinodal decomposition. *Japanese Journal of Applied Physics*. 47(2):1140-1146, 2008.

[27] M. Ohring. *Materials Science of Thin Films*. Elsevier, 2001.

[28] P. Sidles, G. Danielson. Thermal diffusivity of metals at high temperatures. *Journal of Applied Physics*. 25:58-66, 1954.

[29] A. van de Walle, M. Asta, G. Ceder. The alloy theoretic automated toolkit: a user guide. *Calphad*. 26:539-553, 2002.

[30] S. Gohil, R. Banerjee, S. Bose, P. Ayyub. Influence of synthesis conditions on the nanostructure of immiscible copper-silver alloy thin films. *Scripta Materialia*. 58:842-845, 2008.

[31] GD Sim, J. Krogstad, K. Xie, S. Dasgupta, G. Valentino, T. Weihs, K. Hemker. Tailoring the mechanical properties of sputter deposited nanotwinned nickel-molybdenum-tungsten films. *Acta Materialia*. 144:216-225, 2018.

[32] H. Okamoto. Phase Diagrams for Binary Alloys, Desk Handbook, First Edition, 1, Elsevier, 2000.

[33] K. Asami, T. Moriya, K. Hashimoto, T. Masumoto. Roles of temperature and humidity in the oxidation of sputter-deposited Cu-Ta alloys in air. *Corrosion Science*. 44:331-344, 2002.

[34] E. Herman, J. Stewart, R. Dingreville. A data-driven surrogate model to rapidly predict microstructure morphology during physical vapor deposition. *Applied Mathematical Modeling.* 88:589-603, 2020.

[35] L.Q. Chen. Phase-field models for microstructure evolution. *Annual Review of Materials Research*. 32:113-140, 2002.

[36] G. Kairaitis, A. Galdikas. Mechanisms and dynamics of layered structure formation during co-deposition of binary compound thin films. *Coatings*. 10:3-18, 2020.

[37] T. C. Totemeier, W. F. Gale. Smithells Metals Reference Book, Eighth Edition Chapter 13, Elsevier, 2003.

[38] J. Z. Zhao, T. Ahmed, H. X. Jiang, J. He, Q. Sun. Solidification of Immiscible Alloys: A Review. *Acta Metallurgica Sinica (English Letters)*. 30:1–28, 2017.

[39] W. A. Soffa, D. E. Laughlin. Decomposition and ordering processes involving thermodynamically first order order-disorder transformations. *Acta Metallugica*. 37:3019-302, 1998.

[40] J. H. van der Merwe. Equilibrium structure of a thin epitaxial film. *Journal of Applied Physics*. 41:4725, 1970.

[41] W. A. Jesser. A theory of pseudomorphism in thin films. *Materials Science Engineering*. 4:279-286, 1969.

[42] S. A. Dregia, R. Banerjee, H. L. Fraser. Polymorphic phase stability in thin multilayers. *Scripta Materialia*. 39:217–223, 1998.

[43] E. B. Dolgusheva, V. Y. Trubitsyn. Molecular dynamics investigation of the structural stability of body-centered cubic zirconium nanofilms. *Physics of the Solid State*. 54:1652–1662, 2012.

[44] A. Aguayo, G. Murrieta, R. de Coss. Elastic stability and electronic structure of FCC Ti, Zr, and Hf: A first-principles study. *Physical Review B*. 65:092106, 2002.

[45] D. Tomanek, S. Mukherjee, K. H. Bennemann. Simple theory for the electronic and atomic structure of small clusters. *Physical Review B*. 28, 1983.

[46] S. J. Oh, S. H. Huh, H. K. Kim, J. W. Park, G. H. Lee. Structural evolution of W nano clusters with increasing cluster size. *Journal of Chemical Physics*. 111:7402, 1999.

[47] S. Plimpton. Fast Parallel Algorithms for Short-Range Molecular Dynamics. *Journal of Computational Physics*. 117:1-19, 1995.

[48] H. Park, M. R. Fellinger, T. J. Lenosky, W. W. Tipton, D. R. Trinkle, S. P. Rudin, C. Woodward, J. W. Wilkins, R. G. Hennig. Ab initio based empirical potential used to study the mechanical properties of molybdenum. *Physical Review B*. 85:214121, 2012.

[49] M. Marinica, L. Ventelon, M. Gilbert, L. Proville, S. Dudarev, J. Marian, G. Bencteux, F. Willaime. Interatomic potentials for modelling radiation defects and dislocations in tungsten. *Journal of Physics: Condensed Matter*. 25, 2013.

[50] L. Malerba, M. Marinica, N. Anento, C. Björkas, H. Nguyen, C. Domain, F. Djurabekova, P. Olsson, K. Nordlund, A. Serra, D. Terentyev, F. Willaime, C. Becquart. Comparison of empirical interatomic potentials for iron applied to radiation damage studies. *Journal of Nuclear Materials*. 406:19-38, 2010.

[51] G. Pun, K. Darling, L. Kecskes, Y. Mishin. Angular-dependent interatomic potential for the Cu–Ta system and its application to structural stability of nano-crystalline alloys. *Acta Materialia*. 100:377-391, 2015.

[52] R.F. Zhang, X.F. Kong, H.T. Wang, S,H, Zhang, D. Legut, S.H. Sheng, S. Srinivasan, K. Rajan, T.C. Germann. An informatics guided classification of miscible and immiscible binary alloy systems. *Scientific Reports*. 7:9577, 2017.

Chapter 6

Modelling of Compositionally-Driven Formation Mechanism of Hierarchical Morphologies in Co-Deposited Immiscible Alloy Thin Films

The conclusions from the previous chapter show that co-deposited immiscible alloy systems will form hierarchical microstructures under specific processing parameters that accentuate the difference in constituent element mobility. However, the formation mechanism of these unique hierarchical morphologies is difficult to identify since the characterization of these structures is typically done post-deposition. The present chapter employs a combination of phase-field modeling for the microstructure evolution during deposition with microscopy characterization of experimentally-deposited thin films to reveal the origin of the formation mechanism of hierarchical morphologies in co-deposited immiscible alloy thin films. Our results show the significant influence of a local compositional driving force that triggers the simultaneous evolution across multiple length scales, necessary for hierarchical formation. We reveal that there must be a threshold local phase concentration near the surface of the thin film in order to generate distinct hierarchical morphologies in a single domain.

6.1 Introduction

Binary alloy nanocomposite thin-films synthesized via physical vapor deposition (PVD) are used as coatings across a broad range of applications due to their superior performance

including mechanical strength [1,2], elevated fracture toughness [3], and enhanced radiation tolerance[4,5]. It is well understood that co-deposited immiscible alloys will self-organize into phase-separated regions. Under typical PVD processing parameters, the binary films will self-assemble into layers of alternating phases, known as concentration modulations, oriented laterally (LCM), vertically (VCM), or randomly (RCM) [6, 7]. These concentration modulations are classified as monomodal, maintaining a consistent morphology throughout the film. Several mesoscale phase-field models employ classical thin-film growth theory [8, 9, 10, 11, 12, 13] to elucidate the relevant kinetic thermodynamics pathways [14, 15, 16, 17] leading to the formation of these macroscopic monomodal concentration modulation. Recent experimental results present a fourth, novel microstructure morphology with regions self-organizing into a hierarchical architecture [18,19,20]. Hierarchical microstructures are multimodal, having a distinct set of features across multiple length scales. We portray in Fig. 6-1 schematics of sample concentration modulation and hierarchical morphology microstructures. As shown in this figure (Fig. 6-1b), hierarchical structures in binary immiscible alloys typically display significant agglomerates with embedded nanoprecipitates while the remainder of the thin film consists of equimolar concentration modulations. The nanoprecipitate-rich region is termed nanoprecipitate concentration modulations (NPCM). The hierarchical morphologies are a promising functional morphology, worthy of future investigation, as their unique phase organization demonstrates shear band suppression and a homogeneous distribution of stress when deformed [21].

The exact formation mechanism of hierarchical morphologies is presently unknown as *operando* observation of thin film microstructure evolution during PVD interrupts the surface diffusion process and hampers further microstructural evolution [22]. Post-deposition experimental characterization suggests that the hierarchical structures likely form via complex

phase-separation thermodynamics and self-organization processes with multiple simultaneous kinetic activities occurring across several length scales [7,20].

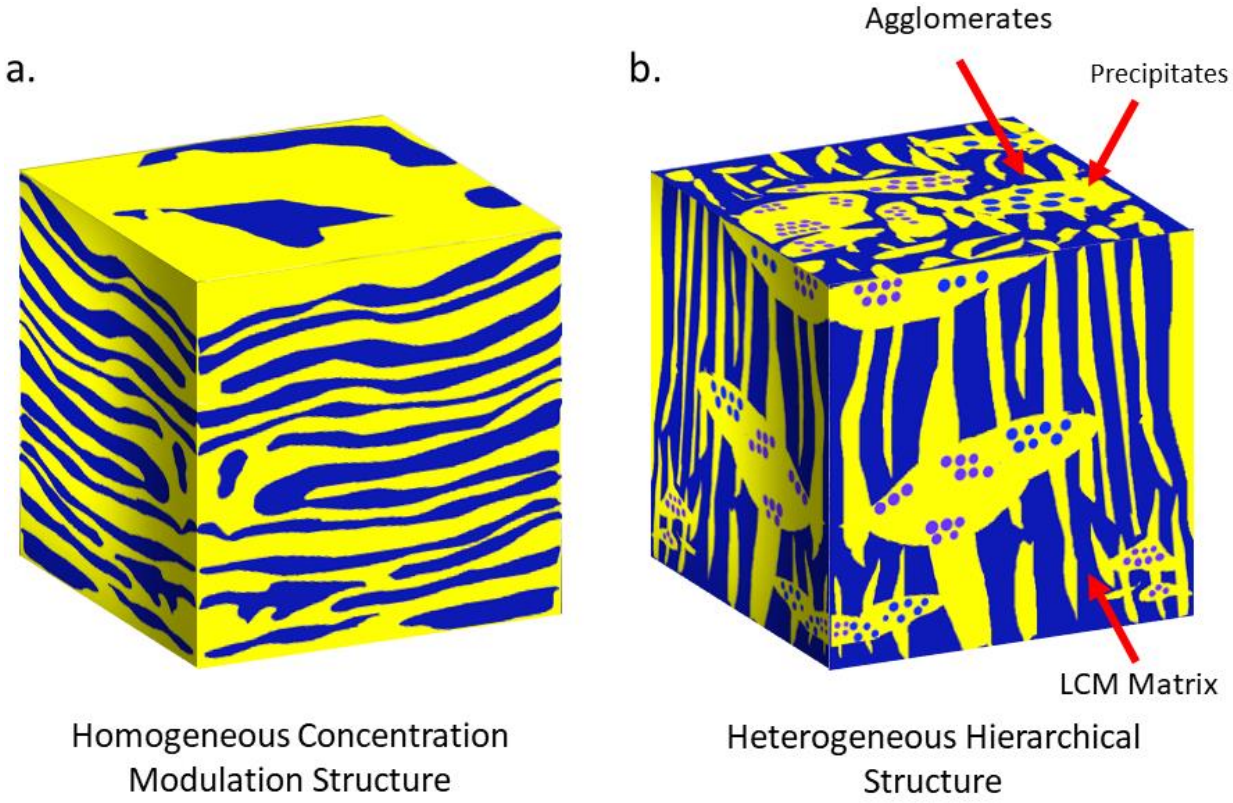

Figure 6-1: Example (a) homogeneous concentration modulations and (b) heterogeneous hierarchical microstructures.

Simple phase-separation and film-growth models lack the ability to capture the complex, concurrent multimodal morphology development and the associated non-equilibrium states that typically develop during hierarchical microstructure evolution. A key characteristic of experimental hierarchical microstructures is the local spatial composition heterogeneity seen near the surface of the deposited thin film. Based on our previous observations [20] and theoretical work [23], we postulate that hierarchical structures form with a multi-step kinetic pathway in binary immiscible alloy systems due to the local compositional inhomogeneity near the surface

of the thin film. We posit that, due to a large discrepancy in the mobility of the immiscible deposited species, the formation mechanism is triggered by the localized, concentrated phase fraction at specific regions near the surface of the film during the deposition process. The result is a compositional driving force that encourages nanoprecipitate formation of a minority phase for the less-mobile elements “trapped” within the agglomerate, while the remainder of the film, which remains at equimolar composition, evolves into the bicontinuous concentration modulation structures. The result is the multimodal microstructure evolution forming hierarchical structures.

To test this hypothesis and fully comprehend the phase-separating, self-assembly hierarchical phenomena, we employed a joint experimental and computational approach. Experimentally, we characterized a series of Cu-Mo thin films co-sputtered at elevated deposition temperatures with the kinetic conditions noted above to facilitate hierarchical organization, e.g., disparate constituent elemental mobilities and processing at high homologous temperature [20]. Computationally, we adapted a previously developed phase-field model to simulate the physical vapor deposition of binary alloys [22, 23] and the formation of various concentration modulations in these thin films. We exercise this phase-field model and validate our predictions with the experimental characterization to identify the necessary conditions that lead to the formation of hierarchical morphologies in co-deposited immiscible alloy thin films.

6.2 Computational Simulation Parameters and Experimental Methods

We simulated the deposition and growth of Cu-Mo thin films as a function of deposition conditions using our previously developed PVD phase-field model [13, 23, 24]. This model has been shown to capture a broad range of experimentally observed concentration modulations dependent on inputted deposition conditions and processing parameters. The model accounts for

major aspects of the PVD process including: (i) the deposition of the incident vapor phase of a binary alloy onto a substrate, (ii) surface interdiffusion, and (iii) the subsequent phase ordering in the resulting inhomogeneous thin film. In this model, the total free-energy functional used to describe the dynamics of the system is a function of two order parameters, one describing the vapor-solid transition and compositional ordering during thin film growth. For the evolution of the compositional field, we solve the Cahn-Hilliard equation in the solid thin film, using structurally and compositionally-dependent mobility function. The mobility function effectively enforces separate diffusivities on the surface and in the bulk of the thin film. We describe the kinetics of thin film growth by solving the Cahn-Hilliard equation for the vapor-solid field variable and include a source term to couple thin film evolution to incident vapor flux. The transport and evolution of the incident vapor flux towards the thin film surface is modeled via the convection-diffusion equation. Elastic effects were neglected in this study. Further details on this model can be found in Ref. [23]. We distinguish our present phase-field model from earlier models simulating phase-separating systems, such as Ref. [13], by the ability of our phase-field model to incorporate the coupled deposition, phase-separation, and surface/bulk kinetic processes between the two depositing species into the Eqn. 2-1. Combining these features with a set of inputs matching experimental deposition parameters is necessary to simulate multimodal morphologies.

We numerically solved the set of coupled partial differential equations using the finite-difference method with second-order central difference stencils for all spatial derivatives. All simulations were performed in two-dimensions on uniform numerical mesh of 512x512 grid points with dimensionless numerical and physical parameters and a time step of $\Delta t = 10^{-2}$. The mobilities for Cu and Mo are based on calculated mobility and observation from experimental

depositions. The bulk mobility values for Cu and Mo are $8.17\times 10^{-4}\,\frac{cm^2}{s/eV}$ and $1.37\times 10^{-10}\,\frac{cm^2}{s/eV}$, respectively. The inputted bulk mobilities for both species were adimensionalized and their corresponding surface mobilities were set an order of magnitude greater. We simulated a dimensionless deposition rate of ν =0.8, which, based on the size of our computational domain and diffusivity parameters selected, corresponds to a 0.8 nm/s for a 1-μm-thick film. We used this model to simulate three different deposition conditions. The first condition corresponds to the deposition of a homogeneous 50-50 at.% alloy composition in the vapor for which we do not expect hierarchical structure formation. The second and third deposition conditions simulate a local imbalance in the phase composition near the surface of the thin film in order to test our hypothesis. For these last two conditions, we considered that the vapor composition was at 90-10 at.% composition in some localized region of the computational domain while the remainder of the vapor domain remained at 50-50 at.% composition. A small and large localized region for the imbalance in the vapor composition were considered in the second and third deposition conditions, respectively. By assuming sub-domains of distinct average composition within the computational domain, we create a variation of free energy landscapes within the film. Within the equimolar region corresponding to the sub-domains, the film microstructure will self-assemble as LCM/VCM, etc., however, in sub-domains where the composition is non-equimolar, the free energy landscape gets locally penalized leading to the formation of globular structures.

To complement and provide credence to our simulated predictions, we compare our simulation results to experimental PVD co-sputtered Cu-Mo thin films. We used Cu (99.999%) and Mo (99.95%) 2'' targets to co-deposit Cu-Mo thin films, with the Cu set at 250 W and the Mo target set at 110 W, onto an oxidized Si substrate rotating at 20 rpm. We applied a 50 W RF bias with a 5" throw distance from the targets to deposit three distinct films at differing

temperatures: 600, 700, and 800°C. The chamber base pressure for deposition was $3.6x10^{-6}$ Pa and the films were deposited at an equimolar Cu-Mo composition to yield a 1 μm thickness at a combined Cu-Mo deposition rate of 0.8 nm/sec. We characterized the cross-sectional and plan-view TEM foils of the films using a scanning transmission electron microscope, JEOL 3100R05 double-Cs corrected S/TEM, operated at 300 keV with point-to-point resolution of 0.055 nm and a convergent angle of 111° for high angle darkfield (HAADF) imaging. True Z-contrast HAADF imagining was accomplished with 8 cm camera length. Energy dispersive X-ray spectroscopy (EDS) compositional maps were collected using a JEOL SDD X-ray detector with a 60 mm^2 active area.

6.3 Results and Discussion

We first examine the sufficient local conditions for film compositional distribution leading to the formation of hierarchical structures. We show in Fig. 6-2a-2c simulated microstructures for three compositional conditions for the binary system with disparate constituent mobilities at a relative deposition rate, ν =0.8. Fig. 6-2a represents a deposition with a homogeneous 50-50 at.% phase fraction. Our results show the co-deposited alloy landing on the substrate and separating into a locally random phase distribution [25]. Newly deposited material will phase separate and diffuse a limited distance via surface diffusion before ultimately being buried by subsequent layers. After minor coarsening via bulk diffusion, the thin film yields concentration modulations in alternating layers in the direction of film growth, termed VCM, aligning with our previous predictions for equimolar deposition [23]. In contrast, as seen in Fig. 6-2b, the presence of a local concentrated region, 90-10 at.%, over a small region near the surface of the thin film affects the subsurface microstructural evolution. The minority phase in the concentrated region becomes spherical and interspersed in a random distribution in the

majority phase. The spherical precipitates coarsen during deposition to form a NPCM structure, while the adjacent 50-50 at.% regions simultaneously form VCM structures. This self-organization is due to energetic minimization in both the concentrated region and the VCM structures. Within the concentrated region, the minority phase with set reduced mobility is unable to diffuse to the adjacent VCM regions, becoming encapsulated and forming spherical precipitates to reduce surface energy within the majority phase agglomerate similar to what has been noted in experimentally co-deposited Cu-Ta systems [19]. The VCM regions follow the

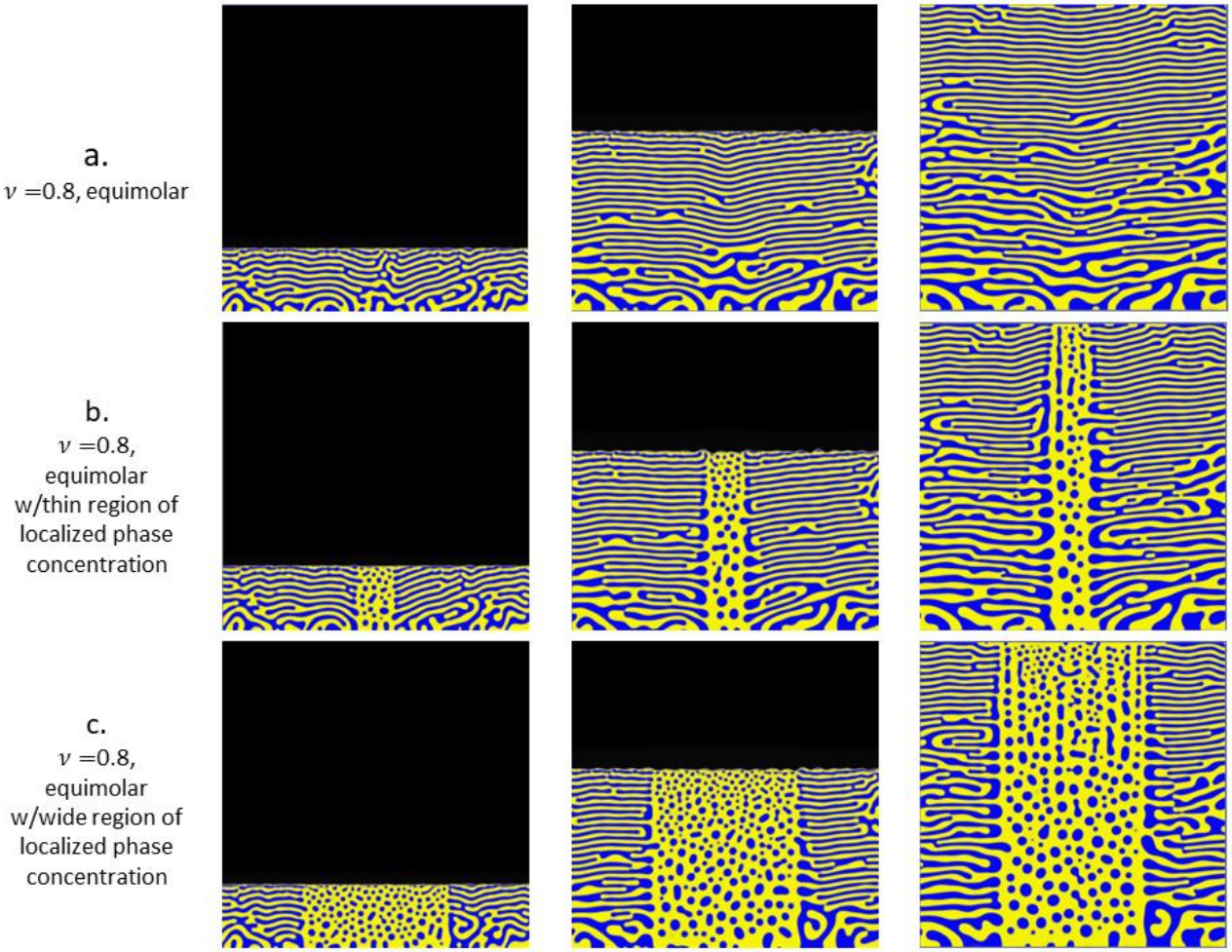

Figure 6-2: Simulated co-deposited of two species under three compositional domains: (a) 50-50 at.% (b) designated region in middle of mesh with 90-10 at.% and remaining area 50-50 at.%, (c) similar to (b) but with wider designated region.

same pathway as described for Fig. 6-2a**.** For a wider local concentration region, a similar observation is noted (see Fig. 6-2c). Again, the "agglomerates-precipitates" and "VCM" morphologies concurrently evolve during deposition. The juxtaposition of the two microstructure morphologies, NPCM and VCM, in Figs. 6-2b, 2c correlates with the experimental observations of the formation of hierarchical structures which show adjacent differing microstructure morphologies at separate length scales [20]. All microstructures in Fig. 6-2 exhibit coarser features towards the bottom of the film due to bulk diffusion during the solid phase deposition.

As previously stated, highly disparate constituent surface interdiffusion lengths in co-deposited immiscible systems will yield hierarchical morphologies in experimental systems [19, 20]. The difference in elemental kinetics leads to preferential agglomeration of one species during deposition, generating a spatially inhomogeneous composition affecting microstructural evolution. A similar compositional influence on film growth has been noted in other systems such as Zr-W thin films [26]. To assess the concentration-morphology dependence, the processing parameters of Cu-Mo films co-sputtered at 600°C with a deposition rate of 0.8 nm/sec were used as inputs into a phase-field model. Localized, highly-concentrated regions were inserted into the computational domain to mimic the effects of preferential agglomeration. Further details on the microscopic characterization of the Cu-Mo films can be found in previous studies [18, 20]. We present in Fig. 6-3a-3d the cross-sectional and plan-view HAADF micrographs with their matching simulated microstructures for four Cu-Mo films. All the micrographs are from the interfacial region between the agglomerate and concentration modulations. The corresponding simulations also contain this interface to probe multimodal morphology growth in our phase-field model. Each simulated microstructure depicts a differing

elemental distribution, but all four simulation predictions replicate the hierarchical features observed experimentally in the related micrographs.

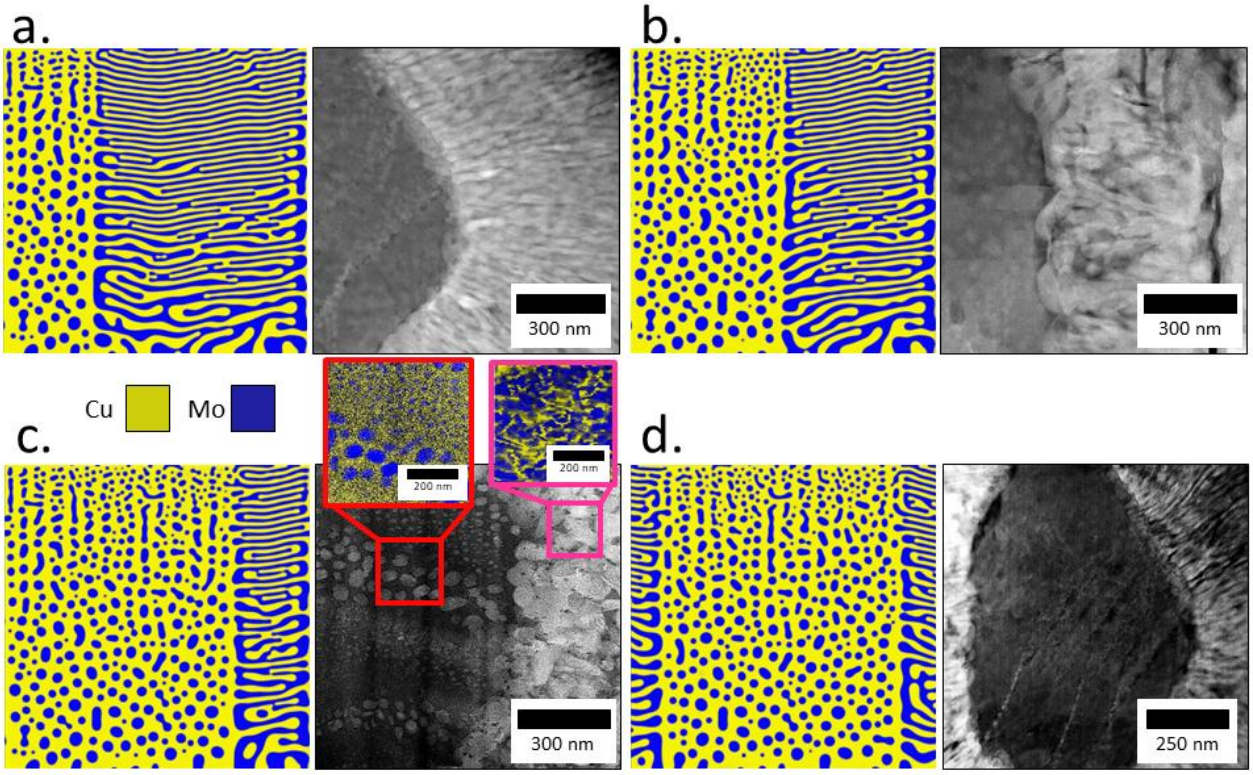

Figure 6-3: (a-d) STEM-HAADF images of four distinct Cu-Mo films co-deposited at 600°C and their respective simulated microstructures with compositional domains from the experimental data. Each micrograph is a magnified image interface of a Cu-rich agglomerate, including Mo nanoprecipitates, and the surrounding Cu-Mo concentration modulations. Darker contrast in HAADF show Cu-rich regions, lighter contrast show Mo-rich regions. The insets in (c) are EDS images of the agglomerate region and the adjoining concentration modulations showing the spatial elemental distribution in each.

In Fig. 6-3a, the cross-sectional HAADF micrograph reveals a darker-contrast Cu-rich region populated by light-contrast Mo-nanoprecipitates surrounded by alternating layers of Cu-Mo VCM. The related simulated microstructure predict a co-deposition with a third of the domain occupied by a Cu-rich domain (90 at. % Cu -10 at. % Mo) and the remainder being equimolar Cu-Mo concentration. The simulated microstructure evolved both regions simultaneously, coarsening the features with limited bulk diffusivity and ultimately forming the familiar hierarchical morphology with juxtaposed NPCM and VCM morphologies. We show in

Fig. 6-3b and Fig. 6-3c similar results for different deposition conditions. The difference being a larger concentrated agglomerate region in the simulated microstructure with highly concentrated localized regions representing 50% and 75% of the domain in Fig. 6-3b and 6-3c, respectively. The first energy-dispersive X-ray spectroscopy image inset in Fig. 6-3c shows a size dichotomy in the experimental Mo nanoprecipitates, with one population approximately 20 nm in diameter and another population approximately 7 nm in diameter. To a degree, the simulated microstructures capture the binary size distribution of the nanoprecipitates as evidenced in Fig. 6-3a-3d. Fig. 6-3d and the corresponding Cu-Mo HAADF image reveal a concentrated region surrounded by two equimolar regions in VCM orientation. Our mesoscale predictions again captured the hierarchical morphology, suggesting the boundary regions have a negligible effect on the evolution of the 90-10 at. % region.

A final quantitative study of the localized concentrated phase fraction is necessary to complement the qualitative reasoning. We conduct a parameterization sweep of the concentration of localized phase fraction regions to determine the threshold agglomeration necessary for the hierarchical formation. We present in Fig. 6-4 six simulated domains with differing phase fraction in the first half of the computational domain, incrementing by 5% at. for subsequent simulations, while the second half remains at equimolar concentration. The simulated phase fractions illustrated in Fig. 6-4 show that the transition from monomodal VCM to multimodal VCM+NPCM occurs for a local phase fraction between 70-30 at.% and 75-25 at.%. Thus, the bimodal morphology evolution necessary for hierarchical formation will only occur when the kinetics of the constituent elements generate agglomeration regions of at least 70-30 at.% phase fraction. Computationally, accurate simulations of hierarchical architectures and multimodal growth must incorporate a concentrated region of at least 70-30 at.% phase fraction.

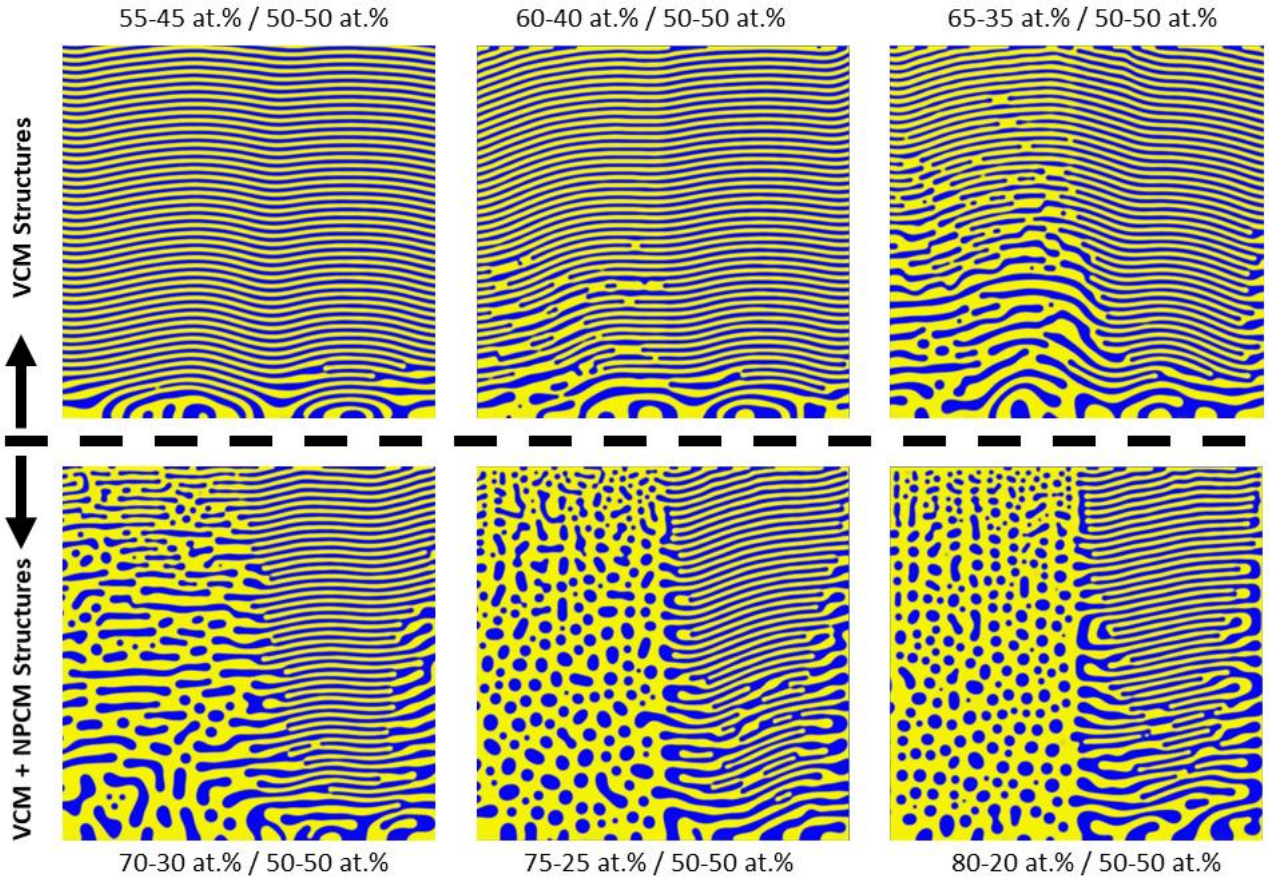

Figure 6-4: Simulated microstructures with split compositional domain with respect to x-axis. The first half had varied phase fraction incrementing by 5 at. %, the second half had equimolar phase fraction. Dashed line delineates the transition from VCM to VCM + NPCM morphologies.

Experimentally, the processing parameters during deposition must favor the accumulation of one species during film growth to create the 70-30 at.% regions. Such preferential agglomeration may be influenced by spatial inhomogeneities of the deposited atoms in the deposition chamber as they land from the vapor phase. Kinetically, the diffusivity of the co-deposited elements can be tuned with deposition temperature and elemental selection [27]. The conditions of low deposition rate and reduced noble gas partial pressure must be present for one species to have an advantageous surface interdiffusion length, leading to its clustering on the film surface during phase separation.

Using the simulation results of Chapter 6 and the experimental results of Chapter 5, we can establish a probable multi-step kinetic pathway yielding the hierarchical structures. The detailed kinetics are predicated on the adatoms of only one species having sufficient kinetic energy for large-scale surface diffusion lengths in the conditions of low deposition rate and elevated deposition temperature. The film evolution is in four stages in Fig. 6-5. In stage one, during an equimolar co-deposition the adatoms of two species land on the substrate surface and diffuse short distances. In stage two, more adatoms land on the substrate surface and the similar species will diffuse and group together, driven by phase-separation energetics. A more mobile species, A, will diffuse a larger distance while less mobile species will diffuse short distances. For stage 3, the subsequent adatoms layer arrives which inhibits the diffusion in the preceding layer. The phase separation continues with the mobile species A preferentially forming agglomerates to minimize the interfacial energy. Trace amounts of species B land in the A agglomerate and get encapsulated inside. By stage 4, the species A agglomerate has grown considerably with multiple isolated clusters of species B. The region outside of the agglomerate are templated by the preceding layers and grow into concentration modulations. The macroscopic film composition is equimolar A-B; however, the composition is closer to 90-10 at.% A-B in the agglomerate region thereby driving the nanoprecipitate formation ultimately seen in experimental micrographs. The surrounding region maintains an approximately 50-50 at.% composition to form the concentration modulation structures.

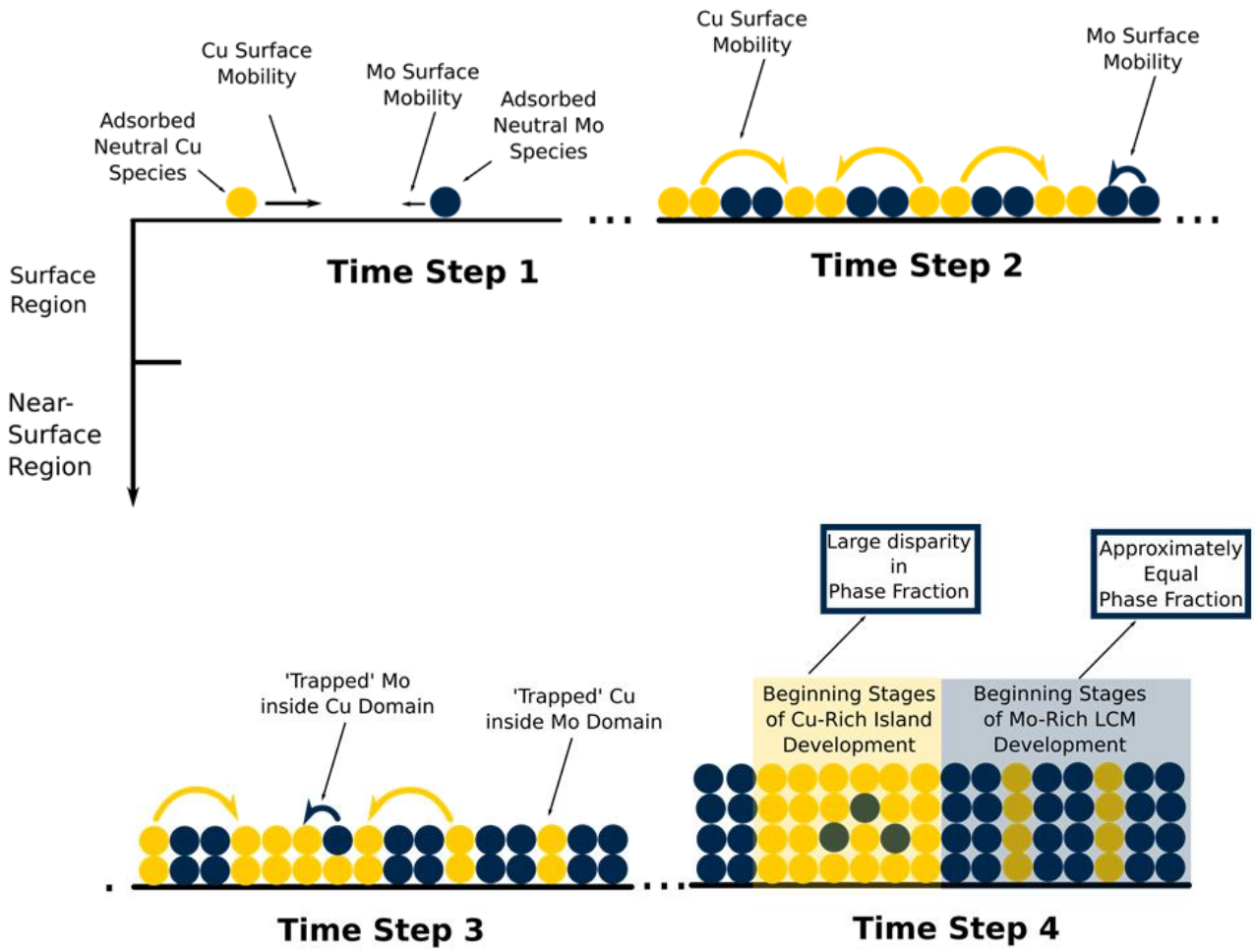

Figure 6-5: Four-step illustration of the multiple kinetic pathways likely responsible for multimodal hierarchical morphologies. Adapted from Ref. [29].

6.4 Conclusions

The results of the present work can be summarized into two essential findings. First, immiscible alloys are likely to form hierarchical morphologies if localized regions of at least 70-30 at.% (approximately) A-B develop, the composition driving the microstructure bimodality during co-deposition. Second, our phase-field model can effectively predict vapor-solid film deposition of a phase-separating system with controlled compositional domains. A logical expansion of this work would be the incorporation of complex thermodynamic free-energy

potentials into our phase-field model to study the deposition of more complex alloys. Our experimental characterization revealed non-equilibrium phases present in hierarchical structures, indicating multiple localized minima in the free energy functional that describes the solid phase equilibria of the system. A metastable state in the NPCM could be stabilized with a third energetic well, akin to prior simulations of three-phase C:Ni thin films [28]; however, targeted compositional regions would still be necessary to induce hierarchical development.

References

[1] D. Yadav, D. Zhao, J.K. Baldwin, A. Devaraj, M. Demkowicz, K. Y. Xie. Persistance of crystal orientations across sub-micron-scale "super-grains" in self-organized Cu-W nanocomposites. *Scripta Materialia*. 194:113667, 2021.

[2] Q. Li, S. Xue, P. Price, X. Sun, J. Ding, Z. Shang, Z. Fan, H. Wang, Y. Zhang, Y. Chen, H. Wang, K. Hattar, X. Zhang. Hierarchical nanotwins in single-crystal nickel with high strength and corrosion resistance produced via a hybrid technique *Nanoscale*. 12:1356-1365, 2020.

[3] Y. Cui, B. Derby, N. Li, A. Misra. Fracture resistance of hierarchical Cu-Mo nanocomposite thin films. *Materials Science Engineering A.* 799:139891, 2021.

[4] B. Derby, J.K. Baldwin, D. Chen, M. Demkowicz, Y. Wang, A. Misra, N. Li. Faceted He-filled "pancakes" confined within nanoscale metal layers. *JOM*. 72:145-149, 2020.

[5] M. Demkowicz, I. Beyerlein. The effects of nanoscale confinement on the behavior of metal laminates. *Scripta Materialia*. 187:130-136, 2020.

[6] B. Derby, Y. Cui, J.K. Baldwin, A. Misra. Effects of substrate temperature and deposition rate on the phase separated morphology of co-sputtered, Cu-Mo thin films. *Thin Solid Film*s. 647:50-56, 2018.

[7] T. W. Heo, D. Shih, LQ Chen. Kinetic pathways of phase transformations in two-phase Ti alloys. *Metallurgical and Materials Transactions*. 45A:3438-3445, 2014.

[8] C.D. Adams, M. Atzmon, Y.T. Cheng, D.J. Srolovitz. Phase separation during co-deposition of Al-Ge thin films. *Journal of Materials Research*. 7(3):653-666, 1992.

[9] M. Atzmon, D.A. Kessler, D. Srolovitz. Phase separation during film growth. *Journal of Applied Physics*. 72:442-446, 1992.

[10] C. Adams, D. Srolovitz. Monte carlo simulations of phase separation during thin-film co deposition. *Journal of Applied Physics*. 74:1707-1715, 1993.

[11] C.V. Thompson. Grain growth in thin films. *Annual Review of Materials Science*. 20:245-268, 1990.

[12] J. A. Thornton. Influence of substrate temperature and deposition rate on structure of thick sputtered Cu coatings. *Journal of Vacuum Science & Technology*. 12(4): 830-835, 1975.

[13] A. Kumar, B. Derby, R. Raghavan, A. Misra, M. Demkowicz. 3-D phase-field simulations of self-organized composite morphologies in physical vapor deposited phase-separating binary alloys. *Journal of Applied Physics*. 126:075306, 2019.

[14] G. Kairaitis, A. Galdikas. Mechanisms and dynamics of layered structure formation during co-deposition of binary compound thin films. *Coatings*. 10:3-18, 2020.

[15] A. Galdikas. Study of nanoclusters growth at initial stages of ultrathin film deposition by kinetic modeling. *Applied Surface Science*. 254:3964-3970, 2008.

[16] Y. Lu, C. Wang, Y. Gao, R. Shi, X. Liu, Y. Wang. Microstructure map for self-organized phase separation during film deposition. *Physical Review Letters*. 109:086101, 2012.

[17] B. Derby, Y. Cui, J. Baldwin, R. Arróyave, J. Demkowicz, and A. Misra. Processing of novel pseudomorphic Cu – Mo hierarchies in thin films. *Materials Research Letters*. 7(1): 1-11, 2019.

[18] M. Powers, B. Derby, A. Shaw, E. Raeker, A. Misra. Microstructural characterization of phase-separated co-deposited Cu-Ta immiscible alloy thin films. *Journal of Materials Research*, 35:1531-1542 (2020).

[19] M. Powers, B. Derby, S.N. Manjunath, A. Misra. Hierarchical morphologies in co-sputter deposited thin films. *Physical Review Materials*, 4(12):123801 (2020).

[20] Y. Cui, B. Derby, N. Li, N. A. Mara, and A. Misra. Suppression of shear banding in high-strength Cu/Mo nanocomposites with hierarchical bicontinuous intertwined structures. *Materials Research Letters*. 6(3):184-190, 2018.

[21] T. Xie, L. Fu, W. Qin, J. Zhu, W. Yang, D. Li, L. Zhou. Self-assembled metal nano-multilayered film prepared by co-sputtering method. *Applied Surface Science*. 435:16-22, 2018.

[22] J. A. Stewart and R. Dingreville. Microstructure morphology and concentration modulation of nanocomposite thin-films during simulated physical vapor deposition. *Acta Materialia*. 188:181-191, 2020.

[23] J.A. Stewart and D.E. Spearot. Phase-field models for simulating physical vapor deposition and grain evolution of isotropic single-phase polycrystalline thin films. *Computational Materials Science*. 123:111-120, 2016.

[24] E. Herman, J.A. Stewart, R. Dingreville. A Data-driven surrogate model to rapidly predict microstructure morphology during physical vapor deposition. *Applied Mathematical Modeling*. 88:589-603, 2020.

[25] J. E. Krzanowski. Phase formation and phase separation in multiphase thin film hard coatings. *Surface Coatings Technology*. 189:376-383, 2004.

[26] A. Borroto, A.C. Garcia-Wong, S. Bruyere, S. Migot, D. Pilloud, J.F. Pierson, F. Mucklich, D. Horwat. Composition-driven transition from amorphous to crystalline films enables bottom-up design of functional surface. *Applied Surface Science*. 538:148133, 2021.

[27] G.A. Langer, G. Erdelyi, Z. Erdelyi, G. Csiszar. Determination of diffusion coefficients in immiscible systems: Cu-W as an example. *Acta Materialia*. 6:100342, 2019.

[28] G. Kairaitis, A. Galdikas. Modelling of phase structure and surface morphology evolution during compound thin film deposition. *Coatings*. 10:1077, 2019.

[29] B. Derby. “Engineering bicontinuous interfaces for enhanced mechanical performance.” Ph.D dissertation, Rackham College of Engineering, University of Michigan, Michigan, 2020. Accessed on: September 10, 2020. [Online].

Chapter 7

Mechanical Performance of Co-Deposited Immiscible Cu-Ta Thin Films

The previous thesis chapters have emphasized how the hierarchical structures form and the necessary processing parameters that enable concurrent evolution across multiple length scales. The present chapter and future work focus on the final third of the processing-microstructure-performance relationship. From the introduction, we note that immiscible alloy thin films in multilayer geometries have prominent mechanical performance in functional applications. However, there are issues of localized shearing at the phase-separated interface, layer rotation and slipping [1], which induce brittle-like failure mechanisms in the plastic regime. In contrast, hierarchical morphologies have exhibited shear band suppression, a more homogenous stress distribution, and increased deformation plasticity prior to fracture [2,3]. Given the novelty of hierarchical morphologies in metallic thin films, preliminary mechanical testing must establish a baseline for elastic and plastic deformation behavior. Thus, we select Cu-Ta as a sample hierarchical thin film and probe indentation behavior under quasi-static loading conditions. The intent is to establish the chief deformation mechanisms of the unique architecture to note any variation from bulk Cu, bulk Ta, or multilayer Cu-Ta thin films of equivalent feature size. As nanoindentation allows for some variation in loading strain-rate, we explore any strain rate sensitivity in mechanical response.

7.1 Introduction

Immiscible alloy films may have interesting mechanical properties due to the distribution of atomically sharp interfaces between the phase separated regions. The length scales of the phase separated regions and the character of the interfaces will influence key deformation mechanisms such as dislocation trapping and suppression of shear localization [1] and may give immiscible alloys, sometimes in the form of metallic nanocomposites, a variety of properties including high yield strength, ductility, and elevated fatigue and wear performance. Copper-based immiscible alloys are capable of enhanced hardness and toughness even at elevated temperatures [2,3]. The thermally stable microstructure paired with heightened mechanical properties as a thin film [4] make Cu-Ta a promising material for protective coating applications. The immiscibility of Cu and Ta enables a wide compositional range for the constituent elements while avoiding the formation of intermetallics which may severely embrittle the alloy.

Prior research on Cu and Ta monolithic films reveal that Cu's mechanical performance is strain-rate sensitive [5] and is generally ductile [6] depending on the grain size. Nanocrystalline Ta films have hardness far exceeding bulk hardness [7] and reduced or even negative strain-rate sensitivity depending on the Ta phase [8]. Combining Cu and Ta as an immiscible alloy increases its mechanical performance beyond what is possible with either solitary element. Multilayer Cu-Ta films have shown enhanced mechanical properties contingent on layer thickness but suffer from shear banding at nanometer-scale layer thicknesses [9]. The penchant for shear banding is attributed to flow localization at the interface which is a function of interfacial nature. Simulations on the similar Cu-Nb system show that dislocation motion, pile-up, flow localization, and strain hardening of multilayers highly depends on interface coherency and orientation [10,11].

Moving beyond the multilayer design, co-sputtering of Cu and Ta film enables the access of three-dimensional nanoscale morphologies that can have high hardness while suppressing shear bands. Variable deposition rates and temperatures can produce a spectrum of morphologies as the Cu-Ta self-segregate into phase separated regions. The scale and orientation of the phase separated regions is important to limit shear banding, inhibit plastic flow localization, and induce interface-dominated deformation mechanisms to yield enhanced mechanical performance of these thin films. This is particularly true if there is nanoscale spacing between microstructural heterogeneities which may behave as barriers to dislocation glide. On such scale, Hall-Petch strengthening [12,13] and confined layer slip will have significant influence on material strength.

As reported in earlier chapters of this dissertation and related publications [14,15] there is a direct relationship between co-deposited Cu-Ta film morphologies as a function of deposition temperature. The following morphologies were produced with the corresponding temperatures: 23°C, nanocrystalline Cu and Ta; 400 °C, wavy-layered bicontinuous Cu-Ta oriented perpendicular to the film growth axis; 600 °C, agglomerated Cu surrounded by thin bands of Ta; and 800 °C, larger agglomerations of Cu with trace amounts of Ta trapped inside and Ta bands with trace amounts of Cu trapped inside. The 800 °C morphology is characterized as a hierarchical structure with features on multiple separate length scales as also observed in co-deposited Cu-Mo [16]. Fig. 7-1 presents high-angle annular darkfield (HAADF) scanning transmission electron microscopy (STEM) micrographs of cross-sectional samples to illustrate the four disparate film morphologies. Macroscopic deformation of these Cu-Ta films is required to gauge their efficacy in protective coating applications. The current work will characterize these four unique morphologies at low strain rates with high throughput testing via nanoindentation to build a base line for future experimentation at dynamic loading conditions. Of

note is the effect of hierarchical morphologies on overall film mechanics. A metallic multilayered Cr/Cu-Cr displayed improved nanoindentation hardness due to the Cu precipitates in the Cr layer [17]. The hierarchical morphologies of Cu-Ta may replicate that behavior with precipitate hardening caused by the minority Cu and Ta phases.

An important consideration for PVD metallic films is the residual stress inherent to the non-equilibrium film deposition process. The heating and cooling during deposition will induce internal stresses caused by the coefficient of thermal expansion mismatch of the substrate and the metallic film. A calculation using the formula for biaxial strain and the coefficient of thermal expansion for Cu of 16×10^{-6}, Ta of 6.5×10^{-6}, and Si of 2.6×10^{-6}, all in units of $m\ (m\ K)^{-1}$, and known elastic constants, yields a calculated stress of 60 MPa in a 50-50 at. % Cu-Ta film deposited at 800 °C [18]. The calculated stress will be compressive upon heating during deposition and tensile upon cooling to room temperature. Compared to the measured hardness (and flow strengths inferred from the hardness) of the Cu-Ta films reported in this article, these residual stresses are very low.

In this investigation, the indentation response of Cu-Ta co-sputtered films at quasi-static strain rates is correlated with film heterogeneities and microstructure morphology. However, surface features such as faceted regions or protruding grains will alter the contact area of the arriving tip and can significantly influence nanoindentation measurements [19]. Thus, both the microstructure and surface topology will be considered when analyzing variations in measured indentation behavior.

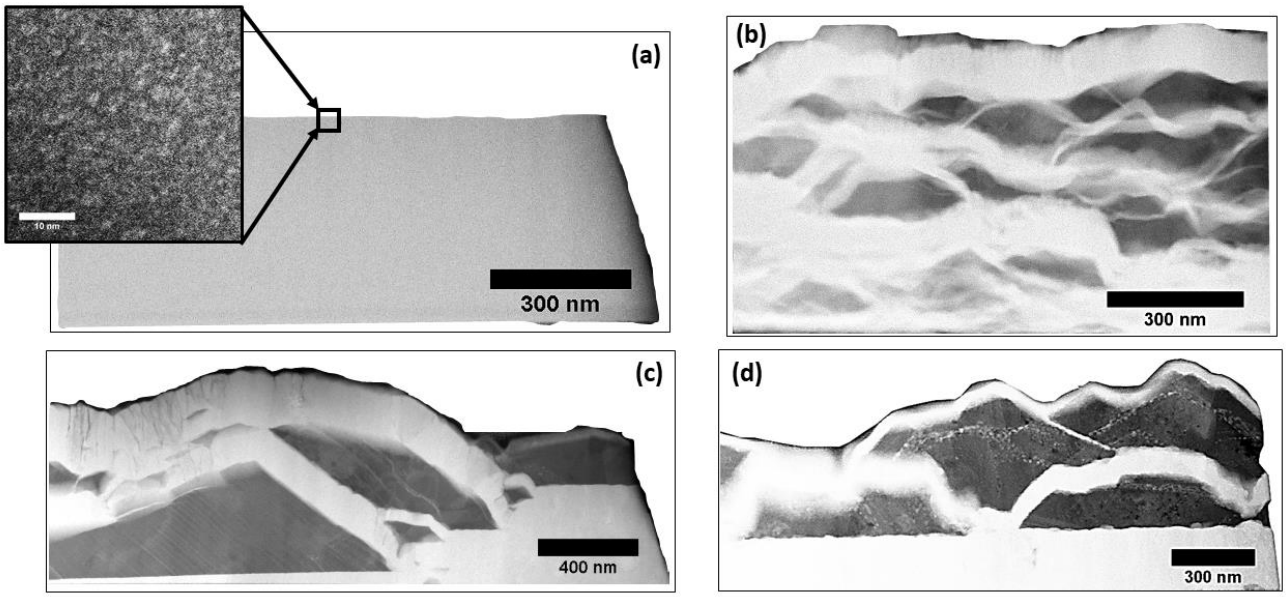

Figure 7-1: HAADF-STEM cross-sectional micrographs of the films of the four deposition temperatures. Ta-rich regions are lighter contrast, Cu-rich regions are darker contrast. (top left, a) 23 °C, with nanocrystalline Cu-Ta phase separated regions as indicated by high resolution TEM inset. (top right, b) 400 °C, alternating concentration modulations oriented perpendicular to the growth direction. (bottom left, c) 600 °C, Cu-rich agglomerates surrounded by Ta-rich veins, note the fine Ta-rich groups in the Cu-rich agglomerates. (bottom right, d) 800 °C, similar agglomerate-vein microstructure but with noticeably larger hierarchical features, particularly the Ta-rich clusters in the Cu agglomerates.

7.2 Fabrication and Characterization

7.2.1 Thin Film Deposition

The co-deposition used 3-inch diameter Si substrates with a 1000 nm thick SiO_2 surface layer. The substrates were ultrasonically cleaned in acetone, rinsed with isopropanol alcohol, then dried with compressed air. The PVD chamber was a Kurt Lesker PVD 75. The chamber maintained a base pressure below 6×10^{-7} Pa and the substrates were cleaned with an RF bias of 50 W for 120 seconds before deposition. The Cu-Ta films were co-deposited via the PVD process of DC magnetron sputtering using 2-inch disk Cu and Ta targets with nominal purities of

99.999% for Cu and 99.95% for Ta. The Cu-Ta targets were simultaneously activated to co-deposit films with 50 at.% Cu-Ta composition with a target throw distance of 5 inches. Four separate depositions were performed at four distinct deposition temperatures: 23 (room temperature), 400, 600, and 800 °C. The deposition temperature refers to the temperature of the substrate that is heated via a heating coil to a consistent temperature during the respective deposition. All films were deposited to a nominal 700 nm thickness. After deposition, the samples were cooled to room temperature over a few hours in the high vacuum of the deposition chamber to prevent oxide formation on the film surface.

7.2.2 Nanoindentation and Imaging

Nanomechanical properties including strain rate sensitivity and surface feature effects were tested using a standard Berkovich probe on a Hysitron 950 Triboindenter. Strain rate sensitivity was assessed over a strain rate range of $5 \times 10^{-3}\ s^{-1}$ to $10\ s^{-1}$. The indentation depth for the strain rate testing was 100 nm except when probing the flat, Ta-rich regions in the 600 °C and 800 °C films at an indentation depth of 80 nm. Indentations for strain rate sensitivity testing were spaced >10 microns from each other and were organized in grids.

The piezo scanning functionality on the Triboindenter was used to generate topographical maps and target particular surface features for indentation. Higher resolution scans performed with a tip velocity of $1 \times 10^{-1}\ s^{-1}$ were used to image the residual indent and confirm its location. Further imaging of the residual indents was performed with a Tescan Mira3 FEG scanning electron microscope. Images were taken in both secondary electron (SE) and backscatter electron (BSE) imaging modes.

7.3 Results

7.3.1 Strain-Rate Sensitivity

The four deposition temperatures of 23, 400, 600, and 800 °C yielded four distinct microstructure morphologies as shown in Fig. 7-1. Expanding further on the feature length scale, the Cu and Ta nanocrystals in the 23 °C film are ~5 nm in diameter. At 400 °C, the Ta-rich and Cu-rich bands are 124±5 nm and 83±4 nm in width, respectively. For 600 and 800 °C, the Cu-rich agglomerates 30 to 500 nm in diameter with Ta rich veins 60 to 200 nm in width.

The film morphologies are a result of the complex relationship of the thermodynamic driving force for phase-separation, the kinetic energy of the landing adatoms, their corresponding surface interdiffusion length during deposition, and the residual stresses generated during elevated temperature co-sputtering. The initial understanding of immiscible alloy thin film growth is based on work by Atzmon [20] and Adams [21] which describe the behavior of the landing adatoms. The deposited two species land on the substrate surface and will preferentially phase separate, diffusing a specific interdiffusion length along the surface before being buried by the oncoming layer of deposition flux. The Atzmon model describes the surface interdiffusion length as:

$$\rho = \sqrt{\frac{D_s \delta}{\nu}} \tag{7-1}$$

where D_s is the surface diffusivity of the species, δ is the thickness of the most recently deposited layer (on the order of interatomic spacing), and ν is the deposition flux. Typically, the adatoms will form locally de-mix to minimize system energy which influences the subsequent layers and as they grow into the homogeneous phase-separated regions. As the surface diffusivity is orders of magnitude higher than the bulk diffusivity and the films are deposited for a limited

period, the bulk diffusion is considered negligible and surface diffusion is the primary facilitator of material flux during film growth. Atzmon and Adams determined that the microstructure morphology is contingent on the surface interdiffusion length of the landing species which is in turn controlled by the deposition rate, the deposition temperature, and the elemental selection.

The evolution of the Cu-Ta microstructures can be placed in the context of surface interdiffusion length during co-deposition. The films were deposited at four distinct temperatures (23, 400, 600, and 800°C) with all other processing parameters held constant. At 23°C, the landing Cu-Ta had limited kinetic energy and diffused a short distance before being buried by the oncoming flux, yielding the nanocrystalline Cu, Ta seen in Fig. 7-1a. Increasing the deposition temperature to 400°C provides moderate kinetic energy to the species which enables phase separation into the wavy, lateral concentration modulation morphology of Fig. 7-1b. For 600 and 800°C an interesting phenomenon is noted, the elevated temperatures resulted in preferential agglomeration of Cu surrounded by vein-like Ta. The rationale is the high surface interdiffusion length for Cu relative to Ta at such temperatures. The agglomeration occurs to lessen the interfacial energy by reducing the contacting area between Cu and Ta phase separated regions. The rapidity of the Cu agglomeration encapsulated trace amounts of the immobile Ta seen in Fig. 7-1c and 7-1d. A description of the surface morphology and phase distribution for each of the experimental Cu-Ta films can be found in a previous work by the author [14]. Further microstructural characterization, including a discussion of the formation mechanisms are elaborated by the authors in an adjacent work [15].

Nanoindentation performed at strain rates $5 \times 10^{-3}\ s^{-1}$ to $10\ s^{-1}$indicated low strain rate sensitivity for all four Cu-Ta films as it pertains to microstructure. The strain rate sensitivity of the 23 °C film ($m_{Cu\text{-}Ta}$) was estimated to be 0.005 by calculating the slope of the best fit line for

the double log plot of flow stress and strain rate, where flow stress is approximated as $Hardness/3$. In comparison to its constituent elements, $m_{Cu\text{-}Ta}$ is lower than that of pure Cu or Ta, with $m_{Cu} \sim 0.1$ and $m_{Ta} \sim 0.05$ for grain sizes around 10 nm [22,23]. We also find that $m_{Cu\text{-}Ta}$ is lower than the strain rate sensitivity for multilayered Cu-Ta of similar composition. Multilayered Cu-Ta with equal layer heights was shown to have $m \sim 0.05$ [24]. From Fig. 7-2, the average elastic modulus for each film has limited variance with respect to strain rate. This correlates with Fig. 7-3 as the films maintain relatively consistent hardness across the strain rates. Any differences across the Fig. 7-2 and Fig. 7-3 values are not a function of the bulk microstructure or strain rate, but rather the surface morphology. As will be elaborated later in this chapter, the specific indentation location greatly alters the measured elastic properties.

In Fig. 7-2, all four films depicted average elastic moduli within the range of 105 GPa +/- 15 GPa which is slightly below the elastic modulus of 121 GPa for monolithic nanocrystalline Cu films [6]. The experimental elastic modulus is also lower than the anticipated calculated rule-of-mixtures 50-50 at. % Cu-Ta elastic modulus of 149 GPa [6,7,25]. The average hardness values in Fig. 7-3 ranged broadly at 4.5 +/- 2.0 GPa. With a nanocrystalline Cu hardness of 1.89 GPa and a nanocrystalline Ta hardness of 11.6 GPa [6,7], the experimental co-deposited Cu-Ta trended slightly under the calculated rule-of-mixtures 50-50 at.% Cu-Ta of 6.75 GPa. A key observation from Fig. 7-3 is that the 23 °C film consistently performed on the higher end of the experimental hardness values. Averaging across all strain rates, the 23°C film with nanometer-scale phase separated Cu-Ta displayed over 50% greater hardness than the other films.

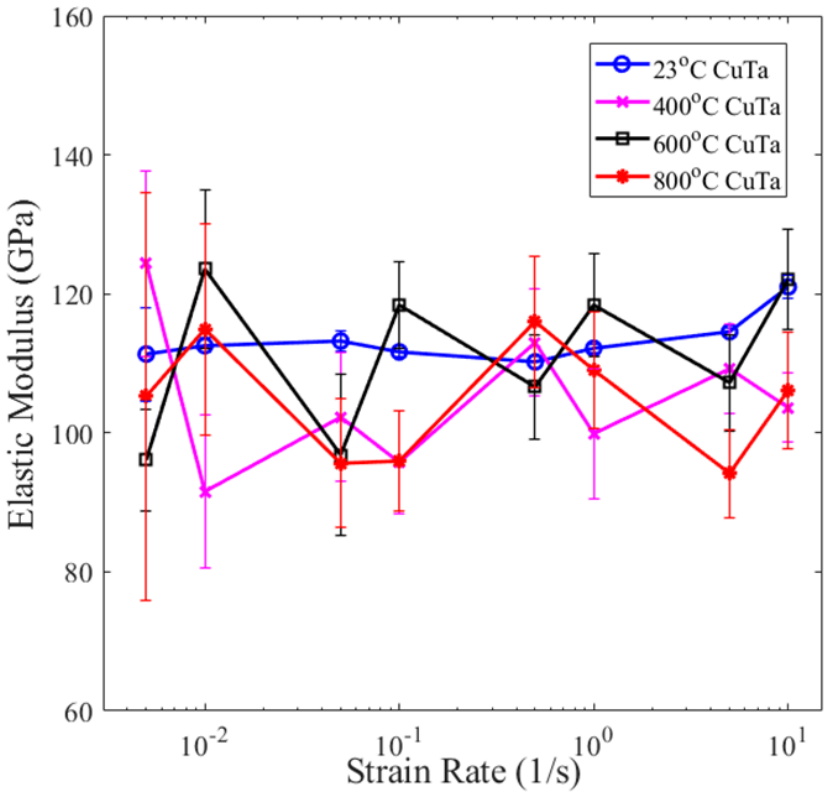

Figure 7-2: Average elastic moduli of Cu-Ta films deposited at varying temperatures tested across multiple strain rates. The error bars correspond to +/- one standard error.

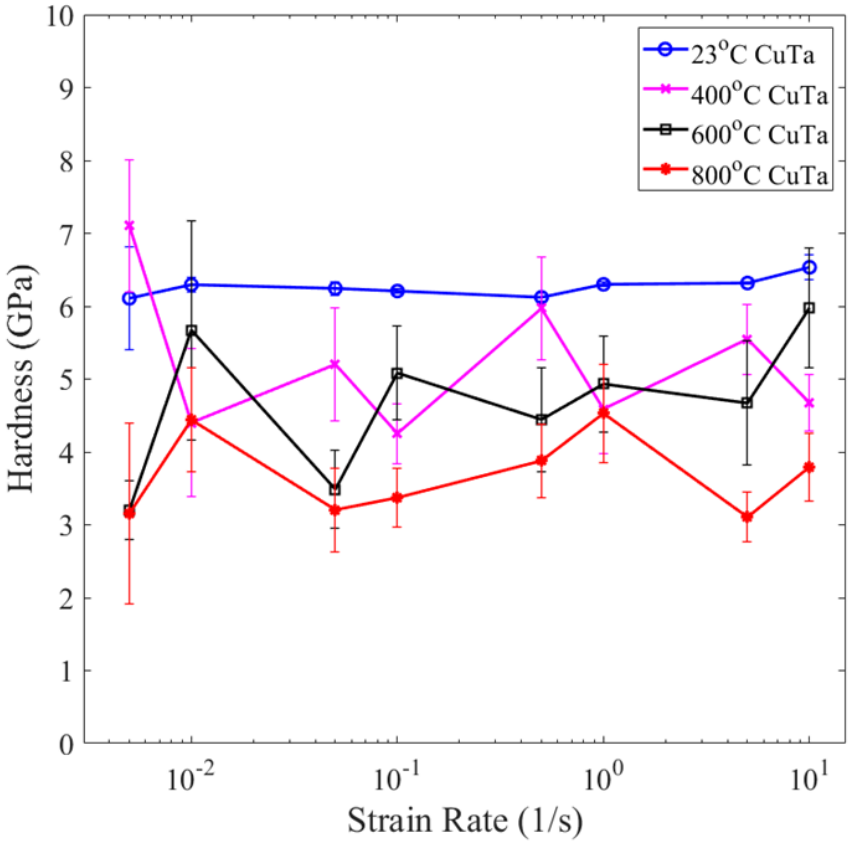

Figure 7-3: Average hardness of Cu-Ta films deposited at varying temperatures tested across multiple strain rates. The error bars correspond to +/- one standard error.

7.3.2 Spatially Dependent Mechanical Performance

The substantial range in mechanical performance across indentations on a single film prompted investigation into factors other than microstructure that are influencing measured properties. The result is a high spatial dependence that is correlated to variant surface morphologies in the 400, 600, and 800 °C films. The histograms in Fig.7- 4 quantify the spatial dependence with respect to measured elastic modulus and hardness. The relative strain insensitivity in the high throughput testing suggests the indents from all tested strain rates can be used equivalently to compare the distribution of mechanical performance across the film surfaces. The histograms reveal a narrow normal distribution for both measured properties in the 23 °C film due to its planar, uniform surface of nanocrystalline Cu-Ta. The 600, and 800 °C films depict widened normal distributions for measured elastic modulus. The hardness histograms indicate bimodality with a majority cluster of low hardness indents followed by a minority cluster of elevated hardness values equivalent or exceeding the hardness of nanocrystalline Ta [25]. The 400 °C film has a wide distribution of elastic moduli but does not exhibit the hardness bimodality. An important metric of skewed distributions is the median value which is plotted against deposition temperature at the bottom of Fig. 7-4. In terms of general trends, elastic moduli and hardness both decline with respect to increasing deposition temperature.

Distinct surface morphology is the source of the spatially variant elastic moduli and bimodality of hardness in the 400, 600, and 800 °C films. The 400 °C film has coarse features with jutting grains (tens of nanometers-scale) that encompasses the whole surface. The 600 and 800 °C films both contain rough surfaces that can be classified into two cases. The first case is the coarsened, but uniform-in-height Ta-rich regions that also contain a minority phase of

nanocrystalline Cu. The second case is a large protruding grain (hundreds of nanometers-scale) or "hillock" induced by stress relaxation and agglomeration of the more mobile species, Cu. The 600 and 800 °C films each have equal spatial fraction of the flat Ta-rich regions and protruding Cu-rich hillocks.

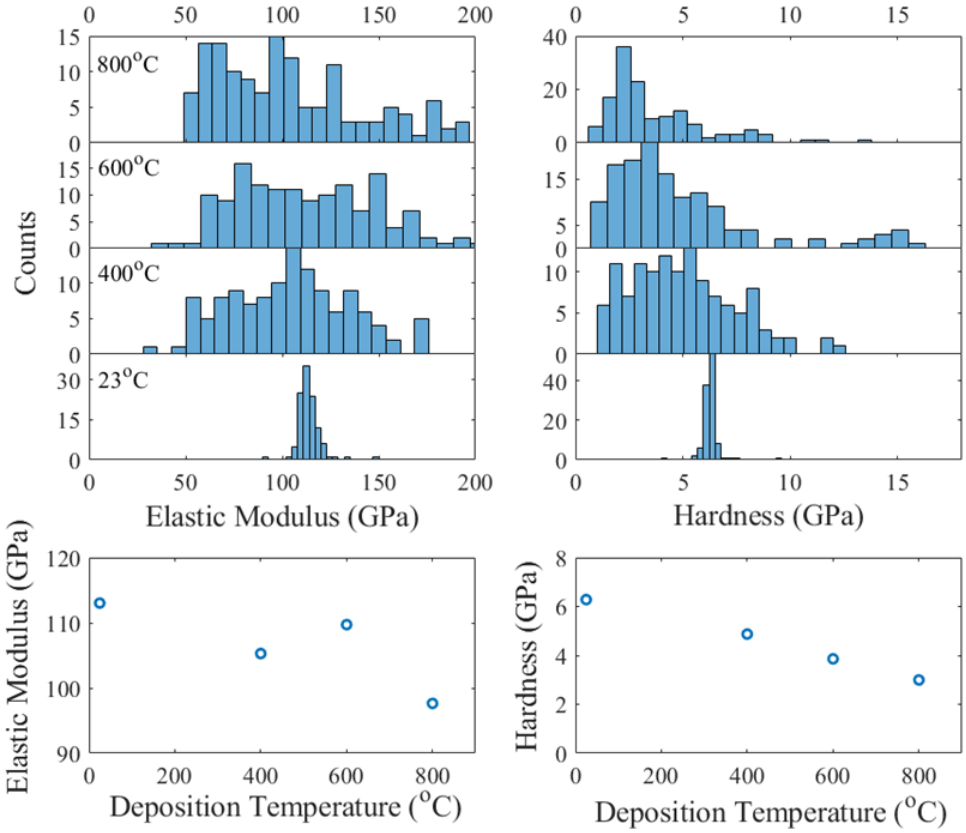

Figure 7-4: (top) Histograms representing the spatial distribution of mechanical properties across the film surface. The histograms are the combined data from the strain rate testing for each Cu-Ta film. (bottom) Median hardness and elastic modulus as a function of deposition temperature.

The wide normal distributions and bimodality encouraged examination of specific points on the film surface. In the 400 °C film, variations in mechanical properties can be attributed to the angle of contact between the Berkovich tip and the surface. Small grains jutting out of the surface and material displacement altered the contact area of the tip during the relatively shallow

nanoindentation. The 600 and 800 °C films present a different case. A series of nanoindentations were performed that targeted specific flat regions between hillocks and sizable facets on the top of hillocks. A wide disparity in measured mechanical properties arose between the flat, Ta-rich regions and hillocks containing Cu-rich agglomerates.

The quantifiable data is represented in Fig. 7-5. As anticipated, the flat regions had mechanical properties akin to nanocrystalline Ta. The hillocks exhibited lower hardness and limited elastic deformation aligning with behavior observed for monolithic nanocrystalline Cu films. This was particularly interesting given that the hillocks tend to have thin layers of Ta-rich regions (~100 to 200 nm in width) that surround the Cu-rich agglomerates. The Ta-rich veins had limited effect as the agglomerated Cu underneath the protrusions readily displaced even under loads $\leq$ 1000 μN. The bimodality in mechanical response was accentuated at 600 °C and less prominent at 800 °C which is directly correlated to the comparatively reduced spacing between Cu-rich agglomerates in the 800 °C microstructure. Spatial influence on properties will be an important consideration for any future testing at low or high strain rates on Cu-Ta films co-deposited at 600 or 800 °C.

A series of load-controlled indents 200-300 nm in depth were performed to establish a qualitative understanding of the plastic deformation mechanisms in the surface features of the Cu-Ta films. These specific indents were not included in the data from the previously mentioned figures due to the potential Si substrate effects. The SEM images of the indentation geometries is displayed in Fig. 7-6. In Fig. 7-6a, indentations on the 23 °C film maintain a uniform indentation geometry even at increased strain. This is a departure from previous nanoindentation research performed on Cu-Ta multilayers [9]. In the multilayer geometries, shear banding deformation was prevalent in samples with phase-separated Cu and Ta layers $\leq$9 nm in width. In the current

experiment, the phase separated Cu and Ta nanocrystals are ~5 nm in diameter but shear banding is absent from post-indentation SEM images. The lack of shear bands can be attributed to a homogenous stress distribution and limited regions for flow localization among the texture-less nanocrystals.

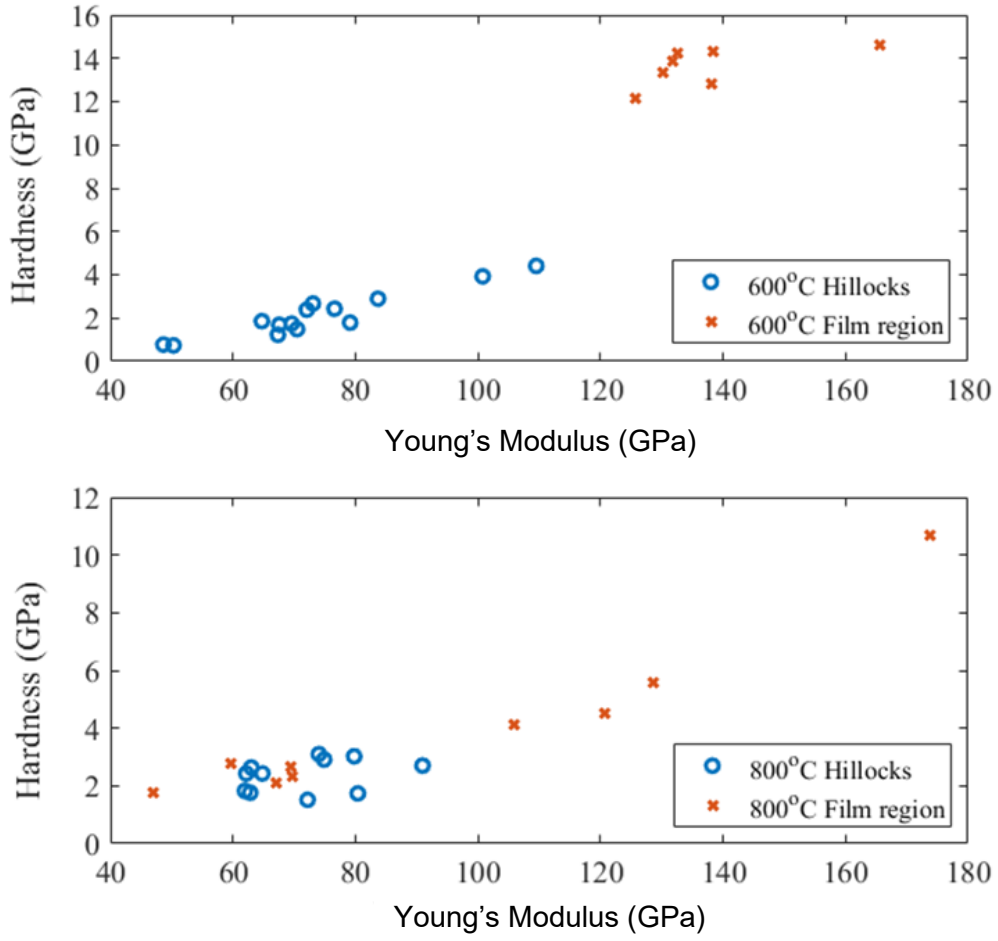

Figure 7-5: Elastic modulus and hardness of the two targeted surface morphology features. A hillock is a grain protruding from the film surface, in this case having a Cu-agglomerate core, and the film region denotes a planar Ta-rich surface. The error bars correspond to +/- one standard deviation.

The SEM images in Fig. 7-6b, 7-6c exemplify the bimodality in the mechanical response of the 600 and 800 °C films. Both indents had the same applied force, but indentations on the film's flat section in Fig. 7-6b showed marginal material displacement while Fig. 7-6c shows

significant material displacement and a deeper indent into the hillock feature. Fig. 7-6b also depicts the difficultly in isolating the measured properties from the Ta-rich regions as the indentation tip may contact small protruding grains on the film surface. Therefore, key source for error in this high throughput testing technique is varied tip contact area due to displaced material or non-uniform surfaces. The error is less applicable in the current experiment given the shallowness of the indents (80 to 100 nm) but can be sizeable in future research.

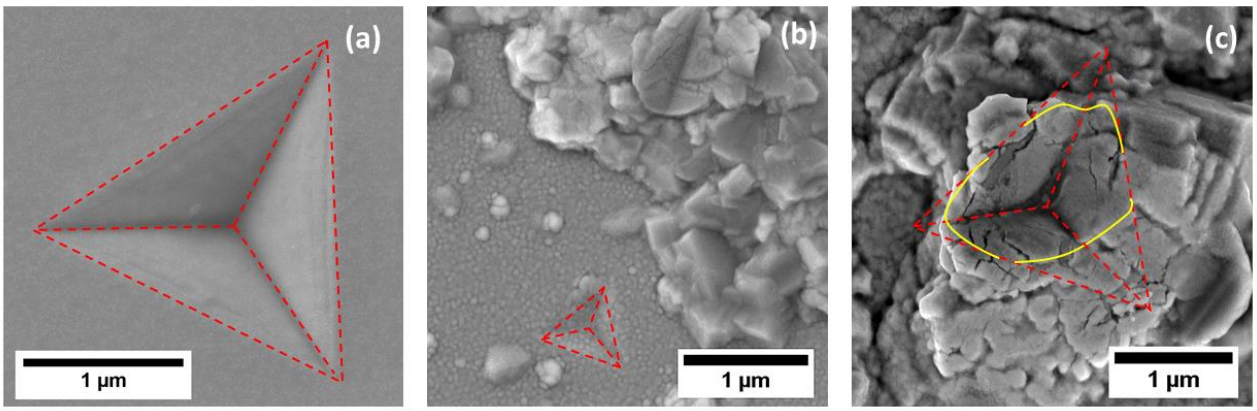

Figure 7-6: SE SEM images of residual high-load indentations on the surface of Cu-Ta deposited at 23 °C (a) and targeted surface morphologies for 600 °C (b) and 800 °C (c).

7.3.3 Comparative Results

To establish a comprehensive scope, the median values of hardness and elastic moduli in Fig. 3 of the 600 °C film are compared to nanoindentation data from Cu-Ta co-deposited at room temperature and annealed for a period of two hours at 650 °C performed by Bahrami *et al*. [4]. Comparing films of nearly the same 50-50 at. % Cu-Ta composition, the 600 °C film (current experiment) and as-deposited film have approximately equal hardness. While the annealed film is harder by ~2 GPa, the elastic moduli of the as-deposited and annealed films aligned with the

calculated rule-of-mixtures 50-50 at. % Cu-Ta elastic modulus of 149 GPa, showing higher stiffness than the 600 °C film.

One step further is to examine if the median hardness values in the current experiment continue to follow the rule-of-mixtures as a function of processing temperature. Fig. 7-7 [6,26-31] compares the co-deposited Cu-Ta to literature monolithic Cu and Ta that have been annealed at various temperatures. The trend reveals the median hardness nearly follows the extrapolated average between the monolithic Cu and Ta at the same processing temperature. A lack of hardness data for the monolithic films processed at 600 and 800 °C leave ambiguity to the validity of the trend for the hierarchical structures in the 600 and 800 °C films.

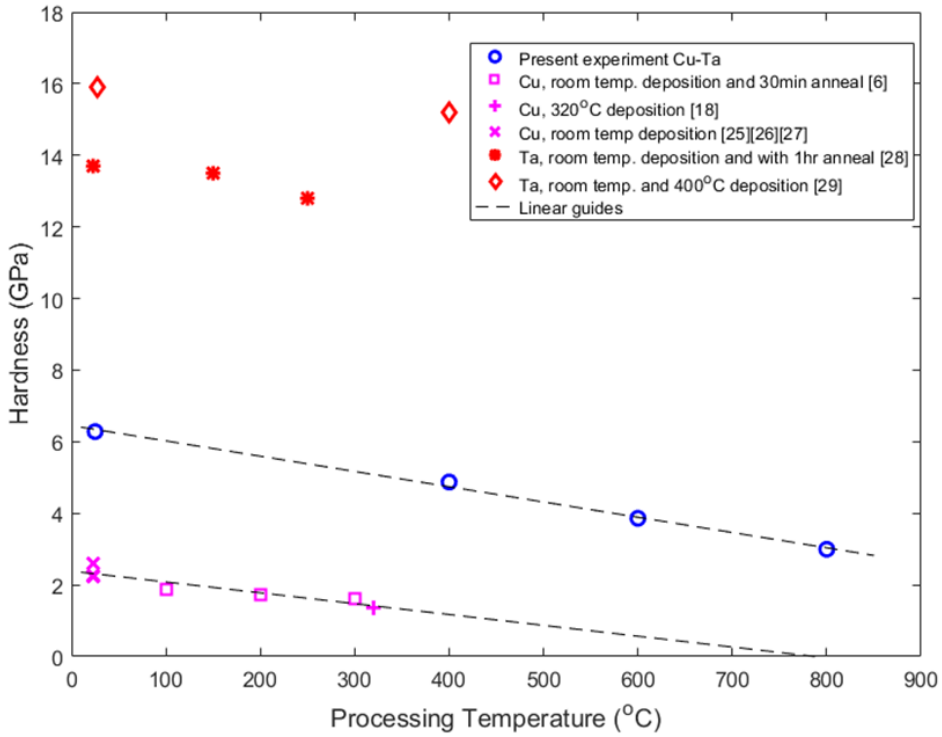

Figure 7-7: Hardness values as a function of temperature. Literature hardness values for monolithic Cu and Ta films annealed at various temperatures are compared to hardness values of Cu-Ta in the present experiment. The trend lines indicate general behavior and are not empirically based.

7.4 Discussion

All four heterogeneous Cu-Ta microstructures maintained minimal strain rate sensitivity for the range probed in this experiment, 5×10^{-3} s^{-1} to 10 s^{-1}. Although the strain rate is varied across four orders of magnitude, the strain rates are still relatively low and would not activate high or very-high strain rate deformation mechanisms, e.g., twinning. Other reasons for the reduced strain rate sensitivity are the semi-coherent Cu-Ta interfaces with their discontinuous slip systems for dislocation transmission and precipitate hardening caused by Ta nanoprecipitates in the hierarchical morphologies. As both semi-coherent interfaces and precipitates impede the dislocation motion, any reduction of the activation barrier for dislocation motion caused by an increase in strain rate may be minimal which may be the source of the low observed strain rate sensitivity in Cu-Ta. Any conclusive statements on the exact influence of interfaces as impediments on dislocation motion in the material would have to be verified with *in situ* microscopy experiments in future studies. The same is true to validate any dislocation pile-up, bowing, or confined layer slip which may all be occurring at instances of sufficient strains in the material.

Nanoindentation is a high throughput method to determine the elastic properties of film surfaces. The key metrics of hardness and elastic modulus are extracted from the data on tip displacement as a function of applied load. Original nanoindentation studies conducted by Oliver and Pharr [32] describe the elastic modulus as:

$$\frac{1}{E_r} = \frac{(1-\nu^2)}{E} + \frac{(1-\nu_i^2)}{E_i} \qquad (7\text{-}2)$$

where E_r is the reduced modulus which is calculated based on the slope of the unloading region of the indentation curve, E and ν are the elastic modulus and Poisson's ratio for the specimen and E_i and ν_i are the same parameters for the indenter. The hardness is expressed as:

$$H = \frac{P_{max}}{A} \tag{7-3}$$

where P_{max} is the peak indentation load, A is the contact area of the Berkovich tip, and H is the specimen hardness. Nanoindentation of the Cu-Ta provided two key sources of error that influenced the accuracy of Eqns. 7-2 and 7-3. Material displacement and jutting grains on the film's surface affected both the contact area and the calculated reduced modulus. As a result, the measured hardness and elastic modulus could vary even when measuring film regions with nearly identical underlying morphologies. The error was less influential in the Cu-Ta deposited at 23 °C, moderate in the 400 °C sample, and especially prominent in the 600 and 800 °C films. The increased error was due to the ductile Cu-agglomerations under the hillocks which created large areas of uneven surfaces and experienced high material displacement even under reduced loads.

The authors sought theoretical and experimental methods to minimize the inaccuracy caused by material displacement and imprecise contact area. Formalism by Saha and Nix [33] presented stiffness as a measurable property for mechanical performance. Normalizing the applied load by the square of the stiffness provides a metric that is insensitive to indentation depth and therefore projected contact area. However, the majority of literature on nanoindentation of Cu-Ta thin films provide results in the form of hardness and elastic modulus. To enable direct comparison to literature values, the authors chose not to adopt the metric proposed by Saha and Nix. Instead, the authors turned to experimental methods to reduce the error. With reduced applied load, shallow indentation depths, and precise location selection, it was possible to achieve consistent mechanical performance and avoid outliers in the data.

Given the shallowness of the indents and the emphasis on macroscopic properties, quantifiable properties were limited to the elastic regime. Mechanical performance as function of

temperature for monolithic Cu or Ta films in Fig. 7-7 suggest that the Hall Petch relationship pertaining to grain size plays a key role in material performance. The specific Hall-Petch strengthening coefficient of $k_h = 5.2 \times 10^{-3}$ MPa $nm^{1/2}$ may explain the reduction in hardness with the coarser microstructures seen for Cu-Ta deposited at increased deposition temperatures [34]. However, further experimentation is necessary to draw conclusions on any Hall-Petch relationship or deviation thereof in these complex Cu-Ta films. The unique nature of co-deposited Cu-Ta microstructure would make grain size studies difficult, particularly in the hierarchical structures with the phase separated regions on multiple length scales. Additionally, the trapped Ta or Cu phases in the 600 and 800 °C films may be critical in preventing grain boundary rotation or grain boundary sliding but *in situ* measurements at higher strains would be needed to confirm this.

The absence of shear bands in the extended depth indentations of Fig. 7-6 suggest an equitable distribution of flow stress in all four films. This behavior contrasts with shear banding noted for Cu-Ta multilayers [9] but aligns with homogenous stress distributions observed in Cu-Mo hierarchical structures [35]. The Cu-Mo hierarchical structures are akin to those seen in the 600 and 800 °C Cu-Ta with large agglomerations of Cu surrounded by a secondary structure. The hierarchical Cu-Mo reached compressive strengths upwards of 2.6 GPa at engineering strains exceeding 0.1 without shear band formation. The hierarchical structure suppressed shear banding due to uniform stress distributions throughout the Cu-Mo sample from dislocation pile-up and strain hardening effects paired with the variant spatial distribution of Cu-Mo interfaces which are weak in shear and susceptible to plastic flow localization. The same underlying factors can rationalize the suppression of shear banding of the current co-deposited Cu-Ta films.

The heterogeneity of the surface topology in the 600 and 800 °C Cu-Ta reflects some variation in the mechanical performance. As noted in section 7.3.2, the faceted, protruding hillocks are composed primarily of underlying Cu-rich agglomerates while the flat regions of the film are principally Ta-rich. The hardness of the hillock region was consistent with results for monolithic Cu films [25,26]. The hardness of the Ta-rich flat region had ample variability, in some instances reaching the hardness of pure Ta films, around 12 to 15 GPa dependent on processing [28,29], and in some instances it was a reduced 2 to 3 GPa, particularly in the 800 °C film. While the topology is a contributing factor, the compositional distribution is likely the chief parameter dictating mechanical performance. Any future nanoindentation at high strain rates must account for the heterogenous distribution of elements and likely variable mechanical performance contingent on the location of the indentation.

The present work is distinguished from similar nanoindentation performed on co-deposited Cu-Ta because of the unique microstructures that arise from elevated deposition temperatures of nominally equi-atomic Cu-Ta films. With increased deposition temperatures, surface diffusion becomes the chief vehicle for material flux as landing adatoms will travel up to a specific interdiffusion length as determined by the kinetics of the adatoms, the driving forces for phase separation and chemical potential gradients induced by stress within the film, and the deposition rate of the oncoming layers. The dominance of surface diffusion coupled with high deposition temperatures yields the hierarchical structures with large agglomerates of Cu and the entrapment of the less mobile Ta and low mobility Ta impeding Cu movement. The frozen bulk approximation [20] means little change in the film bulk during the deposition process. Co-sputtered Cu-Ta from literature [4,36,37] deposited the films at room temperature and annealed the films for a period of time at elevated temperature. The annealing facilitates bulk diffusion

and grain boundary movement. The resulting microstructures may be bicontinuous or concentration modulated but have not yet indicated any hierarchical formatting.

7.5 Conclusions

The elastic macroscopic mechanical performance of co-deposited Cu-Ta films was tested using high-throughput nanoindentation to establish low strain rate baseline for eventual high-strain testing. The four Cu-Ta films deposited at 23, 400, 600, and 800 °C appeared to have little correlation between elastic modulus and strain rate as well as hardness and strain rate, and large variances were present in the measurements for the 400, 600, and 800 °C samples. The strain rate sensitivity of the 23 °C sample was calculated to be 0.005 for the probed strain rate range of 5×10^{-3} s^{-1} to 10 s^{-1}. The large variances of mechanical performance at a given strain rate for the 400, 600, and 800 °C samples prompted further exploration into film surface morphologies. Indentations across the surfaces revealed a spatial dependence in the 600 and 800 °C films. The two films at elevated temperatures contained surface features identified as Ta-rich planar regions and protruding grains, hillocks, caused by Cu-agglomeration. Precise indentation into these two features showed a dichotomy of performance and revealed a source of error as indentation may potentially displace material and have incorrect contact area. Furthermore, the co-deposited Cu-Ta suppressed the formation of shear bands even as the indentation depth exceeded 10% of the film thickness. When comparing the median Cu-Ta film hardness to literature monolithic Cu and monolithic Ta as a function of processing temperatures, the hardness appears to follow a rule-of-mixtures for 50-50 at. % Cu-Ta.

References

[1] N. A. Mara and I. J. Beyerlein. Review : effect of bimetal interface structure on the mechanical behavior of Cu – Nb fcc – bcc nanolayered composites. *Journal of Materials Science*. 49:6497–6516, 2014.

[2] Y. Cui, B. Derby, N. Li, and A. Misra. Fracture resistance of hierarchical Cu–Mo nanocomposite thin films. *Materials Science & Engineering A*. 799:139891, 2021.

[3] A. Chatterjee, E. Sprague, J. Mazumder, A. Misra. Hierarchical microstructures and deformation behavior of laser direct-metal-deposited Cu-Fe alloys. *Materials Science and Engineering A*. 802:140659 (2021).

[4] A. Bahrami, C.F. Onofre Carrasco, A. Delgado Cardona, T. Huminiuc, T. Polcar, S. E. Rodil. Mechanical properties and microstructural stability of CuTa/Cu composite coatings. *Surface Coatings Technology*. 364:22-31, 2019.

[5] S. Suresh, T.G. Nieh, B.W. Choi. Nano-indentation of copper thin films on silicon substrates. *Scripta Materialia*. 41:951-957, 1999.

[6] S.Y. Chang, T.K. Chang. Grain size effect on nanomechanical properties and deformation behavior of copper under nanoindentation test. *Journal of Applied Physics*. 101:033507, 2007.

[7] M. Zhang, B. Yang, J. Chu, T.G. Nieh. Hardness enhancement in nanocrystalline tantalum thin films. *Scripta Materialia*. 54:1227-1230, 2006.

[8] Y.M. Wang, A.M. Hodge, P.M. Bythrow, T.W. Barbee, A.V. Hamza. Negative strain rate sensitivity in ultrahigh-strength nanocrystalline tantalum. *Applied Physics Letters*. 89:081903, 2006.

[9] F. Wang, P. Huang, M. Xu, T.J. Lu, K.W. Xu, Shear banding deformation in Cu/Ta nano-multilayers. *Materials Science and Engineering A*. 528:7290-7294, 2011.

[10] S. Shao, H.M. Zbib, I.N. Mastorakos, D.F. Bahr. Deformation mechanisms, size effects, and strain hardening in nanoscale metallic multilayers under nanoindentation. *Journal of Applied Physics*. 112:044307, 2012.

[11] I.N. Mastorakos, A. Bellou, D.F. Bahr, H.M. Zbib, Size-dependent strength in nanolaminate metallic systems. *Journal of Materials Research*. 26:1179-1187, 2011.

[12] E.O. Hall. The deformation and ageing of mild steel: III discussion of results.

Proceedings of the Physical Society - Section B, 64:747, 1951.

[13] N.J. Petch. The cleavage strength of polycrystals. *The Journal of the Iron and Steel Institute*. 174:25-28, 1953.

[14] M. Powers, B. Derby, E. Raeker, N. Champion, A. Misra. Hillock formation in co-deposited thin films of immiscible metal alloy sytems. *Thin Solid Films*. 693:137692, 2020.

[15] M. Powers, B. Derby, A. Shaw, E. Raeker, A. Misra. Microstructural characterization of phase-separated co-deposited Cu-Ta immiscible alloy thin films. *Journal of Materials Research*, 35:1531-1542, 2020.

[16] B. Derby, Y. Cui, J. Baldwin, R. Arróyave, J. Demkowicz, and A. Misra. Processing of novel pseudomorphic Cu – Mo hierarchies in thin films. *Materials Research Letters*. 7(1): 1-11, 2019.

[17] P.C. Wo, N. Abdolrahim, Y.F. Zhu, I.N. Mastorakos, D.F. Bahr, H.M. Zbib. Precipitation strengthening in nanocomposite Cr/Cu–Cr multilayer films. *Philosophical Magazine.* 95:1780-1794, 2015.

[18] A. Segmuller, M. Murakami. X-ray diffraction analysis of strains and stresses in thin films. *Treatise on Materials Science & Technology*. 27:143-200, 1988.

[19] W.G. Jiang, J.J. Su,, X.Q. Feng. Effect of surface roughness on nanoindentation test of thin films. *Engineering Fracture Mechanics.* 75:4965-4972, 2008.

[20] C.D. Adams, M. Atzmon, Y.T. Cheng, D.J. Srolovitz. Phase separation during co-deposition of Al-Ge thin films. *Journal of Materials Research*. 7(3):653-666, 1991.

[21] M. Atzmon, D.A. Kessler, and D.J. Srolovitz. Phase separation during film growth. *Journal of Applied Physics*. 72:442, 1992.

[22] P. Huang, F. Wang, M. Xu, K.W. Xu, T.J. Lu. Dependence of strain rate sensitivity upon deformed microstructures in nanocrystalline Cu. *Acta Materialia*. 58:5196-5205, 2010.

[23] Z. Cao, Q. She, Y. Huang, X. Meng. The rate sensitivity and plastic deformation of nanocrystalline tantalum films at nanoscale. *Nanoscale Research Letters.* 6:186, 2011.

[24] Q. Zhou, J.J. Li, F. Wang, P. Huang, K.W. Xu, T.J. Lu. Strain rate sensitivity of Cu/Ta multilayered films: Comparison between grain boundary and heterophase interface. *Scripta Materialia*. 111:123-126, 2016.

[25] G. Guisbiers, E. Herth, L. Buchaillot, T. Pardoen. Fracture toughness, hardness, and Young's modulus of tantalum nanocrystalline films. *Applied Physics Letters*. 97:143115, 2010.

[26] U. Kanders, K. Kanders, J. Maniks, V. Mitin, V. Kovalenko, P. Nazarovs, D. Erts. Nanoindentation response analysis of Cu-rich carbon-copper composite films deposited by PVD technique. *Surface Coatings Technology*. 280:308-316, 2015.

[27] D. Beegan, S. Chowdhury, M.T. Laugier. Comparison between nanoindentation and scratch test hardness (scratch hardness) values of copper thin films on oxidised silicon substrates. *Surface Coatings Technology*. 201:5804-5808, 2007.

[28] I. Velicu, V. Tiron, B. Rusu, G. Popa. Copper thin films deposited under different power delivery modes and magnetron configurations: A comparative study. *Surface Coatings Technology*. 327:192-199, 2017.

[29] H.C. Barshilia, K.S. Rajam. Characterization of Cu/Ni multilayer coatings by nanoindentation and atomic force microscopy. *Surface Coatings Technology*. 155:195-202, 2002.

[30] Y.T. Chen. Nanoindentation and Adhesion Properties of Ta Thin Films. *Journal of Nanomaterials*. 154179: 2013.

[31] Z. Cao, X. Meng. Inverse Hall-Petch effect of hardness in nanocrystalline Ta films. *Advances in Materials Research*. 378:575-579, 2011.

[32] W. C. Oliver and G. M. Pharr. An improved technique for determining hardness and elastic modulus using load and displacement sensing indentation experiments. *Journal of Materials Research*. 7(6):1564-1583, 1992.

[33] R. Saha and W. D. Nix. Effects of the substrate on the determination of thin film mechanical properties by nanoindentation. *Acta Materialia*. 50:23-38, 2002.

[34] T. Venugopal, K. Prasad Rao, B. Murty. Mechanical and electrical properties of Cu-Ta nanocomposites prepared by high-energy ball milling. *Acta Materialia*. 55:4439-4445, 2007.

[35] Y. Cui, B. Derby, N. Li, N. A. Mara, and A. Misra. Suppression of shear banding in high-strength Cu/Mo nanocomposites with hierarchical bicontinuous intertwined structures. *Materials Research Letters*. 6(3):184-190, 2018.

[36] C. M. Muller, S. Parviainen, F. Djurabekova, K. Nordlund, and R. Spolenak. The as-deposited structure of co-sputtered Cu–Ta alloys, studied by X-ray diffraction and

molecular dynamics simulations. *Acta Materialia*. 82:51-63, 2015.

[37] C. M. Muller, S. Parviainen, F. Djurabekova, K. Nordlund, R. Spolenak. The as-deposited structure of co-sputtered Cu-Ta alloys, studied by X-ray diffraction and molecular dynamics simulations. *Acta Materialia.* 82:51-63, 2015.

Chapter 8

Conclusions, Summaries, and Suggestions for Future Work

8.1 Conclusions

The fundamental accomplishment of this dissertation has been the thorough investigation of multimodal hierarchical microstructure morphologies in FCC/BCC immiscible alloy thin films. The intention was to establish a processing-microstructure-relationship for hierarchical microstructures which are a novel morphology in co-deposited metallic thin films. Chapters 3 and 4 focus on the characterization of co-deposited Cu-Ta to study the microstructural features including the interfaces between the phase-separated regions, the orientation and geometries of the grains, the surface topology, and the phase states. Chapter 5 investigate a number of co-deposited immiscible alloy systems to generalize the kinetic and thermodynamic conditions necessary to form hierarchical morphologies. The work expanded on previous research accomplished by Derby *et al*. to establish a set of conditions favorable for the complex multimodal organization. In Chapter 6, the research incorporated a coding framework developed by collaborators at Sandia National Laboratories to study the effect of localized compositional regions on the solid evolution during thin film growth. Ultimately, the experimental and simulation results helped frame a multi-scale development pathway for the hierarchical architectures. Finally, Chapter 7 probed the mechanical properties of Cu-Ta hierarchical morphologies. Preliminary nanoindentation noted mild strain-rate sensitivity of Cu-Ta with

hardness and elastic modulus instead more contingent on the spatially heterogeneous compositional distribution. The mechanical characterization represents the most promising field for future research. Further work can probe the mechanical performance of hierarchical structures across different immiscible alloy systems and at a variety of strain rates to activate differing deformation mechanism and test any extended plasticity properties.

The main points of the dissertation results are enumerated below:

1.) Chapter 3, Cu-Ta co-deposited at 25, 400, 600, and 800 °C yielded distinct morphologies at each temperature. STEM images of the film cross sections showed the microstructure morphology varied from nanocrystalline Cu-Ta at 25 °C to a wavy ribbon-like structure at 400 °C, to Cu-rich agglomerates or clusters surrounded by Ta-rich veins at 600 and 800 °C. In the agglomerate-vein morphology, microstructural features were present on two length scales: a few nm to tens of nm, thus making the structures hierarchical. On the nanoscale, the Cu-rich agglomerates contained Ta precipitates while the Ta-rich veins had embedded Cu nanocrystals. The various microstructures can be attributed to the highly disparate constituent element mobility at the deposition temperatures with the Cu having orders of magnitude higher mobility than Ta at the deposition temperatures.

2.) In Chapter 4, for Cu-Ta and Cu-Mo-Ag films co-deposited at 25, 400, 600, and 800 °C. A significant number of homogeneously distributed surface hillocks were observed only in the 600 and 800°C films. HAADF cross-sectional imaging revealed significant Cu agglomerations underneath the protruding features. For the Cu-Ta films, the Cu was enveloped in a Cu-Ta nanocrystalline matrix. For Cu-Mo-Ag, the Cu was surrounded by Mo-Ag concentration modulations. While thermal stress

gradients arise during deposition of immiscible metal films, biaxial stress calculations and literature cases reveal that they are not solely responsible for hillock formation. The observed morphologies align with a surface diffusion kinetic model that evaluates diffusion length of adatoms during deposition as a function of deposition temperature. This indicates a phase separation driving force paired with the constituent elements' dissimilar mobilities at elevated deposition temperatures contribute to the presence of hillocks.

3.) For Chapter 5, hierarchical structures form with sufficient disparity in kinetic energy between the constituent atoms in a co-deposited immiscible alloy system, one species being highly mobile (A) and the other relatively immobile (B). This condition arises typically at elevated deposition temperatures and reduced deposition rates but is also alloy dependent. The hierarchical structures form during deposition via phase separation and self-organization processes across the multiple length scales. The adatoms diffuse on the film surface with the highly mobile species swiftly agglomerating into A-rich domains within which B-rich nanoprecipitates form, often self-organizing into periodic arrays. The smallest B-rich nanoprecipitates in the A-rich domains are found to be coherent and in a metastable crystal structure (B taking the structure of A), but coarser precipitates that exhibit the equilibrium structure of B element. The A-rich domains are surrounded by a B-rich matrix that phase-separates into a concentration modulated structure.

4.) In Chapter 6, simulation results show the significant influence of a local compositional driving force that triggers the simultaneous evolution across multiple length scales, necessary for hierarchical formation. We reveal that there must be a

threshold local phase concentration of at least 70-30 at. % in a localized region near the surface of the thin film in order to generate distinct hierarchical morphologies in a single domain.

8.2 Future Work

As this dissertation concludes, there are three areas related to hierarchical structures in immiscible alloy metallic thin films that warrant future exploration. The first is an analysis of fabricating high entropy alloys with physical vapor deposition. High entropy alloys are a newly discovered system of metals which form a variety of solid solutions composed of equimolar compositions of four or more alloys. Typically, these high entropy samples are fabricated with arc melting to account for the disparate melting temperatures of the components which can range upwards of 3000 ºC for refractory metals. Physical vapor deposition presents itself as an ideal fabrication technique since sputtering is agnostic to melting temperatures. Furthermore, high entropy alloys present an interesting application case of the kinetics described in this dissertation. Can the same kinetic arguments of surface interdiffusion length and the potential creation of a hierarchical microstructure morphology be applied if we co-deposit five or more alloys with limited miscibility? Furthermore, the exact hierarchical nature could vary depending on the alloy selection. Instead of two characteristic lengths describing the system, as is the case in Cu-Ta and Cu-Mo, perhaps three or more may be necessary if fabricating the Cantor alloy with co-deposition.

The metastable and equilibrium phases present in the hierarchical morphologies generate ambiguity as to describing the system with an appropriate Gibbs' free energy function. As mentioned in Chapter 6, the phase diagrams are based off equilibrium states present in immiscible pairings. The hierarchical structures present a number of non-equilibrium phases

which complicate the Gibbs expression significantly. Mapping the energetic favorability of the various states in the hierarchical morphologies would improve the accuracy of phase-field models and their ability to simulate the concurrent phase separation occurring on multiple length scales which has yet to be truly depicted up to this point.

Nanoindentation and flyer plate tests must be used to further characterize the mechanical response of the hierarchical morphologies. The results presented in this research can be further expanded to incorporate high and very high strain rate loading conditions which will activate a number of shock-response deformation mechanisms in the constituent elements of the hierarchical microstructures. A key point of interest is how the Cu-rich agglomerates will perform and whether they will experience significant stress localization and ultimately be the incipient point for material failure. Another note is the plastic behavior and whether the microstructures will retain any ductility with their hierarchical organization.